

Electronic Theses and Dissertations, 2004-2019

2016

Fundamental Understanding of Interactions Among Flow, Turbulence, and Heat Transfer in Jet Impingement Cooling

Md. Jahed Hossain
University of Central Florida

 Part of the [Mechanical Engineering Commons](#)
Find similar works at: <https://stars.library.ucf.edu/etd>
University of Central Florida Libraries <http://library.ucf.edu>

This Doctoral Dissertation (Open Access) is brought to you for free and open access by STARS. It has been accepted for inclusion in Electronic Theses and Dissertations, 2004-2019 by an authorized administrator of STARS. For more information, please contact STARS@ucf.edu.

STARS Citation

Hossain, Md. Jahed, "Fundamental Understanding of Interactions Among Flow, Turbulence, and Heat Transfer in Jet Impingement Cooling" (2016). *Electronic Theses and Dissertations, 2004-2019*. 5308. <https://stars.library.ucf.edu/etd/5308>

FUNDAMENTAL UNDERSTANDING OF INTERACTIONS AMONG FLOW,
TURBULENCE, AND HEAT TRANSFER IN JET IMPINGEMENT COOLING

by

JAHED HOSSAIN

B.S. Mechanical Engineering, Bangladesh University of Engineering & Technology, 2008
M.S. Mechanical Engineering, University of North Carolina at Charlotte, 2011

A dissertation submitted in partial fulfillment of the requirements
for the degree of Doctor of Philosophy
in the Department of Mechanical and Aerospace Engineering
in the College of Engineering and Computer Science
at the University of Central Florida
Orlando, Florida

Fall Term
2016

Major Professor: Jayanta S. Kapat

© 2016 Jahed Hossain

ABSTRACT

The flow physics of impinging jet is very complex and is not fully understood yet. The flow field in an impingement problem comprised of three different distinct regions: a free jet with a potential core, a stagnation region where the velocity goes to zero as the jet impinges onto the wall and a creation of wall jet region where the boundary layer grows radially outward after impinging. Since impingement itself is a broad topic, effort is being made in the current study to narrow down on three particular geometric configurations (a narrow wall, an array impingement configuration and a curved surface impingement configuration) that shows up in a typical gas turbine impingement problem in relation to heat transfer. Impingement problems are difficult to simulate numerically using conventional RANS models. It is worth noting that the typical RANS model contains a number of calibrated constants and these have been formulated with respect to relatively simple shear flows. As a result typically these isotropic eddy viscosity models fail in predicting the correct heat transfer value and trend in impingement problem where the flow is highly anisotropic. The common RANS-based models over predict stagnation heat transfer coefficients by as much as 300% when compared to measured values. Even the best of the models, the $v^2 - f$ model, can be inaccurate by up to 30%. Even though there is myriad number of experimental and numerical work published on single jet impingement; the knowledge gathered from these works cannot be applied to real engineering impingement cooling application as the dynamics of flow changes completely. This study underlines the lack of experimental flow physics data in published literature on multiple jet impingement and the author emphasized how important it is to have experimental data to validate CFD tools and to determine the suitability of Large Eddy Simulation (LES) in industrial application.

In the open literature there is not enough study where experimental heat transfer and flow physics data are combined to explain the behavior for gas turbine impingement cooling application. Often it is hard to understand the heat transfer behavior due to lack of time accurate flow physics data hence a lot of conjecture has been made to explain the phenomena. The problem is further exacerbated for array of impingement jets where the flow is much more complex than a single round jet. The experimental flow field obtained from Particle Image Velocimetry (PIV) and heat transfer data obtained from Temperature Sensitive Paint (TSP) from this work will be analyzed to understand the relationship between flow characteristics and heat transfer for the three types of novel geometry mentioned above.

There has not been any effort made on implementing LES technique on array impingement problem in the published literature. Nowadays with growing computational power and resources CFD are widely used as a design tool. To support the data gathered from the experiment, LES is carried out in narrow wall impingement cooling configuration. The results will provide more accurate information on impingement flow physics phenomena where experimental techniques are limited and the typical RANS models yield erroneous result

The objective of the current study is to provide a better understanding of impingement heat transfer in relation to flow physics associated with it. As heat transfer is basically a manifestation of the flow and most of the flow in real engineering applications is turbulent, it is very important to understand the dynamics of flow physics in an impingement problem. The work emphasis the importance of understanding mean velocities, turbulence, jet shear layer instability and its importance in heat transfer application. The present work shows detailed information of flow phenomena using Particle Image Velocimetry (PIV) in a single row narrow impingement channel.

Results from the RANS and LES simulations are compared with Particle Image Velocimetry (PIV) data. The accuracy of LES in predicting the flow field and heat transfer of an impingement problem is also presented in the current work as it is validated against experimental flow field measured through PIV.

Results obtained from the PIV and LES shows excellent agreement for predicting both heat transfer and flow physics data. Some of the key findings from the study highlight the shortcomings of the typical RANS models used for the impingement heat transfer problem. It was found that the stagnation point heat transfer was over predicted by as much as 48% from RANS simulations when compared to the experimental data. A lot of conjecture has been made in the past for RANS' ability to predict the stagnation point heat transfer correctly. The length of the potential core for the first jet was found to be $\sim 2D$ in RANS simulations as oppose to $1D$ in PIV and LES, confirm the possible underlying reason for this discrepancy. The jet shear layer thickness was underpredicted by $\sim 40\%$ in RANS simulations proving the model is not diffusive enough for a flow like jet impingement. Turbulence production due to shear stress was over predicted by $\sim 130\%$ and turbulence production due to normal stresses were underpredicted by $\sim 40\%$ in RANS simulation very close to the target wall showing RANS models fail where both strain rate and shear stress plays a pivotal role in the dynamics of the flow.

In the closing, turbulence is still one of the most difficult problems to solve accurately, as has been the case for about a century. A quote below from the famous mathematician, Horace Lamb (1849-1934) express the level of difficulty and frustration associated with understanding turbulence in fluid mechanics.

“I am an old man now, and when I die and go to heaven there are two matters on which I hope for enlightenment. One is *quantum electrodynamics*, and the other is the *turbulent motion of fluids*. And about the former I am rather optimistic.”

Source: <http://scienceworld.wolfram.com/biography/Lamb.html>

This dissertation is expected to shed some light onto one specific example of turbulent flows.

DEDICATED TO MY ELDER BROTHER, **TANVIR HOSSAIN**. THANK YOU FOR EVERYTHING.

ACKNOWLEDGMENT

I would like to express my special appreciation and gratitude to my Ph.D. advisor Dr. Jay Kapat, for his continuous support and mentorship throughout the last four years. I am thankful for his guidance and patience. His guidance and advices have been priceless, as they have helped my research as well as given the privilege to work on various funded projects. Every time I had a discussion with him I learned something new. I could not have imagined having a better PhD advisor because it was always a best fit curve for me.

I would also like to thank my committee members: Dr. Ali Gordon, Dr. Kareem Ahmed, and Dr. Paul Weigand for serving on my committee. I appreciate their time, and insightful suggestions and comments on my dissertation work. Thank you for all the encouragement.

A special thanks to Dr. Paul Weigand, for providing support to run my simulations on STOKES during summer 2016.

I am also grateful to Erik Fernandez for his input with the PIV experiment. I have learned a lot from you. I want to also thank all my fellow lab mates at CATER. I have always felt that you are all my family.

I want to thank Mark Ricklick, Wenping Wang, Matt Golsen, and Greg Natsui for being an awesome mentor for me when I started my PhD study. You guys are awesome.

A special thanks to Malay Shah and Brandon Ealy for their help whenever I needed. We started to work on projects and over the years we became friends. I am thankful to both of you for your invaluable support, encouragement, and friendship.

Last, but certainly not least, I must acknowledge Liana Chowdhury. I want to thank you for your love, support and un-wavering belief in me. There are no words than can express my gratitude and appreciation for all the motivation.

Above all, thank you God for allowing me to come thus far. ~

TABLE OF CONTENTS

LIST OF FIGURES	xv
LIST OF TABLES	xxii
LIST OF NOMENCLATURE	xxiii
CHAPTER 1: INTRODUCTION	1
Background	1
Structure of an Impinging Jet	7
Literature Review	9
Narrow Wall Impingement Cooling	10
Array Impingement	17
Curved Surface Impingement	20
Summary	27
CHAPTER 2: OBJECTIVE & MOTIVATION	29
Objective of the Present Study	29
Novelty	30
Intellectual Contribution	31
Dissertation Research Impact	32
CHAPTER 3: INVESTIGATION TECHNIQUES	34
Temperature Sensitive Paint	34

Particle Image Velocimetry	35
Reynolds Averaged Navier-Stokes Equation (RANS)	36
k- ϵ Turbulence Model	39
κ - ω Turbulence Model	42
Reynolds Stress Turbulence Model (RSM)	43
v^2 - f Turbulence Model	43
Large Eddy Simulation (LES)	44
CHAPTER 4: EXPERIMENTAL SETUP	47
Curved surface Impingement	47
Array Impingement	52
Narrow Wall Impingement	55
CHAPTER 5: NUMERICAL SETUP	60
Curve Surface Impingement	60
Boundary Condition	60
Mesh	61
Grid Convergence	63
Array Impingement	64
Boundary Condition	64
Mesh	65

Grid Convergence	68
Narrow Wall Impingement	70
Mesh.....	70
Boundary Condition.....	72
Grid Convergence	73
CHAPTER 6: RESULTS.....	74
Curve Surface Impingement	74
Flow Distribution	74
Experimental Heat Transfer Result.....	78
Turbulator Design.....	79
Post-Impingement Heat Transfer.....	81
CFD Comparison	87
Array Impingement.....	94
Experimental Heat Transfer Results	95
CFD Comparison	99
Narrow Wall Impingement	104
Heat Transfer: RANS vs Experiment	104
Flow Visualizations: RANS vs Experiment	106
CHAPTER 7: DETAILED FLOW FIELD ANALYSIS	111

Mean Axial Velocity Contour.....	111
Shear Layer Thickness	113
Centerline Axial Velocity	114
Streamwise Velocity Profiles.....	119
Mean Axial Velocity Profile at Different Wall Normal Distance	122
Jet Dynamics.....	126
Turbulent Statistics	137
Flow Anisotropy	137
Turbulent Kinetic Energy profile.....	139
Turbulent Shear Stress Profile	141
Turbulent Kinetic Energy Budget.....	147
CHAPTER 8: DETAILED HEAT TRANSFER ANALYSIS.....	154
Heat Transfer Comparison.....	154
Target Wall Nusselt Number	156
Sidewall Wall Nusselt Number.....	160
CHAPTER 9: CONCLUSION AND FUTURE WORK.....	162
Curved Surface Impingement	162
Array Impingement.....	163
Narrow Wall Impingement	163

Future Work	164
Topic1: Revisiting Single Round Jet Impingement	164
Topic 2: Narrow Wall Impingement.....	169
Topic 3: Effect of Crossflow in a Narrow Wall Impingement Cooling	171
APPENDIX.....	173
Statistical Convergence.....	173
Uncertainty Tree for Heat Transfer.....	178
PIV Uncertainty	178
LIST OF REFERENCES	179

LIST OF FIGURES

Figure 1 Components of a basic gas turbine	3
Figure 2 Temperature-entropy diagram of an Ideal Brayton Cycle	3
Figure 3 Non-dimensional work out and pressure ratio dependency	5
Figure 4 Structure of a single round impinging jet	8
Figure 5 Structure of an array of impinging jet	8
Figure 6 Narrow wall impingement cooling concept [6]	11
Figure 7 Turbine airfoils with narrow wall cooling configurations	12
Figure 8 Turbine airfoils with narrow wall cooling configurations	12
Figure 9 Jablonski energy level diagram adopted from [67]	34
Figure 10 Test section for the curved surface impingement	47
Figure 11 Detailed side view of the curved configuration	50
Figure 12 Pressure tap location	51
Figure 13 Flow loop setup [85]	54
Figure 14 Heated area for the impingement channel	54
Figure 15 Test section schematic of the narrow wall impingement channel [25]	56
Figure 16 Flow loop test setup for impingement heat transfer [25]	57
Figure 17 PIV setup	58
Figure 18 Experimental set up	59
Figure 19 Computational domain	61
Figure 20 Mesh of the 90° turbulators	62
Figure 21 Mesh of the W-Shaped turbulators	62

Figure 22 Mesh of the 90° turbulators	62
Figure 23 Grid convergence study	63
Figure 24 Wide array impingement configuration	64
Figure 25 Computational Setup and boundary conditions	65
Figure 26 Detailed Mesh	66
Figure 27 Shear layer refinement	66
Figure 28 Mesh near the jet	67
Figure 29 Near wall refinement	67
Figure 30 Mesh with O-grid block structure	68
Figure 31 Grid independence study	69
Figure 32 Target wall y plus distribution for the finest mesh	69
Figure 33 Mesh at the centerline plane of the channel	71
Figure 34 Mesh from the top	71
Figure 35 Computational setup for the five jet impingement study	72
Figure 36 Grid Convergence	73
Figure 37 Array-averaged discharge coefficients	75
Figure 38 Experimental local G_c/G_J distribution for $Re_j = 55,000$	76
Figure 39 Pressure ratio distribution	77
Figure 40 Turbulator - (90° rib)	79
Figure 41 Turbulator- (W-1 shaped rib)	80
Figure 42 Turbulator- (W-2 shaped rib)	80

Figure 43 Nusselt number profile for the baseline configuration; Upstream curved section (left) & downstream flat section (right)	81
Figure 44 Heat transfer distribution in the post-impingement region for $Re_j = 125K$	83
Figure 45 Laterally averaged Nusselt numbers for baseline curved surface (upstream and downstream)	84
Figure 46 Laterally averaged Nusselt numbers at the downstream section (Baseline, 90° turbulators, and W-shaped turbulators)	85
Figure 47 Heat transfer enhancement for the channel	86
Figure 48 CFD comparison of Nusselt number for $Re_j = 125K$	88
Figure 49 CFD vs Experiment: impingement heat transfer (Upstream)	90
Figure 50 Laterally averaged Nusselt number comparison for 90° Turbulators ($Re_j = 125K$)	90
Figure 51 Laterally averaged Nusselt number comparison for W-1 shaped Turbulators ($Re_j = 125K$)	91
Figure 52 Laterally averaged Nusselt number comparison for W-2 shaped Turbulators ($Re_j = 125K$)	91
Figure 53 Flow streamlines: a) 90° turbulator b) W-1 shaped turbulator c) Primary recirculation zone for the 90° turbulator d) Primary recirculation zone for the W-1 shaped turbulator	93
Figure 54 Nusselt number profile for $Re_j = 10,000$	95
Figure 55 Nusselt number profile for $Re_j = 20,000$	95
Figure 56 Nusselt number profile for $Re_j = 30,000$	96
Figure 57 Iso-surface of velocity magnitude (25 m/s)	97
Figure 58 Laterally averaged Nusselt number profile	99

Figure 59 Nusselt number profile for $Re_j=20,000$ (Experiment)	100
Figure 60 Nusselt number profile for $Re_j=20,000$ (CFD)	100
Figure 61 Laterally averaged Nusselt number comparison	101
Figure 62 Velocity contour comparison between CFD (top) and Experiment (Bottom).	102
Figure 63 PIV layout for the first 10 jets	103
Figure 64 Nusselt number contour (experiment)	105
Figure 65 Nusselt number contour (CFD)	105
Figure 66 Laterally averaged target wall Nusselt number distribution at the target wall	105
Figure 67 Measurement Planes for PIV experiment	106
Figure 68 Jet axial velocity contour for the 2 nd Jet; Experiment (Top) and CFD (Bottom)	107
Figure 69 Jet axial velocity contour for the 6 th Jet; Experiment (Top) and CFD (Bottom)	109
Figure 70 jet axial velocity contour for the 14 th Jet; Experiment (Top) and CFD (Bottom)	109
Figure 71 Axial velocity magnitude contour profile at the centerline plane ($x/D, z/D=0, 0$) of the channel	112
Figure 72 Jet shear layer thickness from PIV, LES, and RANS for the first jet	114
Figure 73 Centerline jet profile for the first three jets in the impingement channel	115
Figure 74 Axial mean velocity profile for the first jet	116
Figure 75 Axial mean velocity profile for the second jet	117
Figure 76 Axial mean velocity profile for the third jet	119
Figure 77 Streamwise velocity profile location (crossflow velocity)	120
Figure 78 Streamwise velocity profile at $x/D=10$	120
Figure 79 Streamwise velocity profile at $x/D=15$	121

Figure 80 Streamwise velocity profile at $x/D=20$	122
Figure 81 Axial velocity profile of v_z at $z/d=2.5$	123
Figure 82 Axial velocity profile in the streamwise direction for $z/D=2.5$	124
Figure 83 Mean axial velocity profile in the streamwise direction for $z/D=0.5$	125
Figure 84 Axial velocity profile in the streamwise direction for $z/D=0.5$	125
Figure 85 Heat transfer distribution for different jet to target wall distance [92]	127
Figure 86 Vortex formation in jet impingement and effect on heat transfer [100], [95]	129
Figure 87 Locations for power spectral density in the jet shear layer	131
Figure 88 Power Spectral Density in the jet shear layer	132
Figure 89 Point probe location in the potential core	132
Figure 90 PSD inside the jet potential core	133
Figure 91 Point probe location in the 5 th jet	134
Figure 92 Power Spectral Density for the fifth jet	134
Figure 93 Point probe location near wall jet	135
Figure 94 PSD near wall region	135
Figure 95 Location of the Reynolds normal stresses	137
Figure 96 Flow field anisotropy at two different axial location for the first jet ($z/D=2.50$)	138
Figure 97 Flow field anisotropy at two different axial location for the first jet ($z/D=0.25$)	138
Figure 98 Locations for turbulent kinetic energy profile comparison	140
Figure 99 Turbulent kinetic profile at different channel height for individual jets	140
Figure 100 Turbulent shear stress profile along the jet centerline	142
Figure 101 Turbulent shear stress profile along the centerline (First jet)	143

Figure 102 Turbulent shear stress profile along the centerline (Second jet)	143
Figure 103 Turbulent shear stress profile along the centerline (Third jet)	143
Figure 104 Shear stress profile location close to the target wall	144
Figure 105 Turbulent shear stress profile close to the target wall, $z/D=0.25$ (first jet)	145
Figure 106 Turbulent shear stress profile close to the target wall, $z/D=0.25$ (second jet)	145
Figure 107 Turbulent shear stress profile close to the target wall, $z/D=0.25$ (third jet)	146
Figure 108 Turbulent shear stress profile close to the target wall, $z/D=0.25$ (fourth jet)	147
Figure 109 Location for turbulent kinetic energy budget calculation	148
Figure 110 Contribution of the normal stresses to the production rate of turbulent kinetic energy	149
Figure 111 Velocity vector from PIV	150
Figure 112 Turbulence production due to normal stresses	150
Figure 113 Comparison of turbulence production rate due to normal stress (PIV, LES, and RSM)	151
Figure 114 Velocity streamline and negative contour of Pw'^2	152
Figure 115 Production of turbulent kinetic energy due to shear	153
Figure 116 Isometric view of the target wall and sidewall heat transfer comparison for $Re_j = 15,000$ (top-LES; bottom-Experiment (TSP))	154
Figure 117 Detailed flow visualization and heat transfer calculated from LES ($Re_j = 15,000$)	155
Figure 118 Target wall Nusselt number contour ($Re_j = 15,000$)	156
Figure 119 Velocity and heat transfer for the first and second jet (Obtained from LES)	157

Figure 120 Laterally averaged Nusselt number comparison for $Re_j = 15,000$ (Experiment and LES)	158
Figure 121 Laterally averaged Nusselt number comparison $Re_j = 15,000$ (Experiment, LES and RANS)	159
Figure 122 Sidewall Nusselt number contour ($Re_j = 15,000$)	160
Figure 123 Laterally averaged Nusselt number for the sidewall heat transfer for $Re_j = 15,000$ (Comparison between experiment and LES)	160
Figure 124 Scalar contour shows the effect of three different inlet velocity profiles [68]	166
Figure 125 Wall resolved mesh for single jet impingement LES case	168
Figure 126 Ratio of the resolved turbulent kinetic energy to the total kinetic energy (M) is at the center plane of the channel	169
Figure 127 Wall resolved LES mesh for narrow wall impingement	171

LIST OF TABLES

Table 1 Summary of narrow work impingement work	15
Table 2 Summary of literary review for array impingement work	19
Table 3 Summary of impingement work with turbulators	23
Table 4 Summary of turbulator work with one wall ribbed configuration	26
Table 5 Test matrix	49
Table 6 Test matrix	55
Table 7 Mesh criteria by [71]	70
Table 8 Mesh criteria for the present study	71
Table 9 Rib parameters	80
Table 10 Variation of the geometry	94
Table 11 Jet Impingement Natural Frequency	136
Table 12 Mesh criteria for wall resolved LES	168

LIST OF NOMENCLATURE

A_c	=	Cross-sectional area (m ²)
A_s	=	Heated area (m ²)
a	=	Speed of sound (m/s)
C_p	=	Specific heat (KJ/KgK)
C	=	Velocity (m/s)
C_s	=	Smagorinsky model constant
C_w	=	WALE model constant
C_d	=	Discharge coefficient
D	=	Jet hole diameter (m)
D_h	=	Hydraulic diameter of the channel (m)
e	=	Rib Height (m)
F_i	=	Body force
h	=	Enthalpy (J)
h	=	Heat Transfer Coefficient (W/m ² -K)
i	=	Current (A)
G_c	=	Channel mass flux
G_j	=	Jet mass flux, $G_j = \rho U_j$
k	=	Thermal conductivity (W/m-K)
k_f	=	Thermal conductivity of air (W/m-K)
k	=	Thermal conductivity (W/m-K)

k	=	$\frac{1}{2} \overline{u'_i u'_i}$, Turbulent kinetic energy
L	=	Height of the jet hole (m)
Nu	=	Nusselt number
P	=	Rib Pitch (m)
Pr	=	Prandtl Number
R	=	Resistance (Ω)
R_{air}	=	Gas constant of air
Re_j	=	Averaged jet Reynolds number
S	=	Streamwise jet spacing for curved surface target plate (m)
S_{ij}	=	Strain rate
S_{ij}	=	Mean strain rate
S_φ	=	Source term for variable φ
T	=	Temperature ($^{\circ}\text{C}$)
T_o	=	Plenum temperature (Pa)
T_{ref}	=	Temperature of reference picture ($^{\circ}\text{C}$)
T_w	=	Wall temperature ($^{\circ}\text{C}$)
T_∞	=	Plenum temperature ($^{\circ}\text{C}$)
U	=	Velocity (m/s)
U_{javg}	=	Average jet velocity (m/s)
U_n	=	n^{th} row jet velocity (m/s)
U_{javg}	=	Average jet velocity (m/s)
U_n	=	n^{th} row jet velocity (m/s)

\bar{U}_i	=	Resolved velocity vector
u_i	=	Instantaneous velocity vector
$\overline{u'^2}$	=	Wall parallel turbulent stress
$\overline{w'^2}$	=	Wall normal turbulent stress
$\overline{u'w'}$	=	Turbulent shear stress
u'_i	=	Unresolved velocity vector
u	=	Instantaneous fluid velocity
V_z	=	Mean axial velocity magnitude (m/s) / wall normal velocity component
V_z	=	Mean streamwise velocity magnitude (m/s)
V_{zmax}	=	Maximum axial velocity magnitude (m/s)
W	=	Work (J)
W	=	Mean axial velocity magnitude (m/s) / wall normal velocity component
X	=	Streamwise jet spacing for flat surface target plate (m)
x_i	=	Co-ordinates in tensor notation
Y	=	Spanwise jet spacing (m)
Z	=	Jet-to-target plate spacing (m)
\dot{m}	=	mass flow rate (kg/s)
p_o	=	Total plenum pressure (Pa)
p	=	Pressure (Pa)
q''_{cond}	=	Heat loss by conduction (W/m ²)
q''_{rad}	=	Heat loss by radiation (W/m ²)
q''_{gen}	=	Heat flux generated by joule heating (W/m ²)

q''_{eff}	=	Effective heat flux (W/m ²)
r	=	Radius of curved surface target plate (m)
s	=	Tangential direction along curved target plate (m)
t	=	Heater thickness (m), time (s)
w	=	Heater width (m)
x, y, z	=	Streamwise, spanwise and wall normal directions
z_1^+	=	Dimensionless wall distance
Re	=	Reynolds number
St	=	Strouhal number
t	=	time(s)

Greek Symbols

Γ	=	Turbulent diffusion coefficient
η	=	Thermal efficiency
δ	=	Shear layer thickness
δ_{ij}	=	kronecker delta
μ, μ_t	=	Molecular and turbulent eddy viscosity
μ^b	=	Bulk-viscosity coefficient
ν, ν_t	=	Kinematic molecular and turbulence viscosities
ε	=	turbulent dissipation rate
σ_{ij}	=	Stress-tensor components due to deformation and bulk dilation
φ	=	Scalar quantity
Δ	=	Filter width

ρ_{el} = Electrical Resistivity ($\Omega\cdot m$)

ρ = Density (kg/m^3)

Δ = Grid Size

μ = Dynamic Viscosity

ν = Kinematic Viscosity

τ_{ij} = Subgrid Stress

μ_{SGS} = SGS Eddy Viscosity

$\Delta x+, \Delta y+, \Delta z+=$ nondimensional size of the grid in three coordinate directions

ρ = Density (kg/m^3)

γ = Heat capacity ratio

δ = Jet shear layer thickness

Acronyms

CCD = Charged Coupled Device

CFD = Computational Fluid Dynamics

LES = Large Eddy Simulation

PIV = Particle Image Velocimetry

PSD = Power Spectral Density

RANS = Reynolds-Averaged Navier-Stokes

SGS = Subgrid Scale

CMOS = Complementary Metal-Oxide-Semiconductor

RSM = Reynolds Stress Model

CVP = Counter-Rotating Vortex Pair

WALE= Wall-Adapting Local Eddy-viscosity SGS Model

Abbreviations

($'$) = prime indicates fluctuating component of a turbulent quantity

($\bar{}$) = Overbar means temporal averaging of a turbulent quantity

CHAPTER 1: INTRODUCTION

Background

Gas turbine can be viewed as an internal combustion engine that is capable of producing a large amount of power for the use of aircraft, propulsion and other industrial applications. The size and weight of these engines vary depending on the application and requirements. The land-based stationary gas turbines are used to generate electric power.

The development of gas turbine began after the Second World War, at which time its use was mostly limited to the turbojet engines for aircraft propulsion. The use of gas turbine for other applications took place in the mid 1950's. Previously, steam turbines had been widely used for electric power generation, but one of the major drawbacks was that the high-pressure, high-temperature steam required installation of large, heavy, and bulky equipment. This major drawback of steam turbines prompted the invention of the gas turbine [1]

The three main components of a typical gas turbine are: compressor, combustion chamber and the turbine. Power is generated by expanding working fluid through the turbine, and in order for this expansion to happen the working fluid must be pressurized before it enters the turbine. The compressor then compresses to achieve the desired compression ratio. These three components are coupled together in a typical gas turbine arrangement. If there are no losses between compression and expansion, the combination between compressor and turbine would turn the turbine. No further output work would be possible to achieve [1]. But the output power developed by the turbine can be increased with the concept of adding a combustor into the system, augmenting the energy of the working fluid. If air is used as a working fluid, the addition of fuel into it can ignite the

compressed fluid. The expansion of hot working fluid in this way would provide a greater power output in addition to driving the compressor. This is an ideal scenario.

But in reality, there is always a pressure drop across the compressor and across the turbine. This results in a loss that increases the power absorbed by the compressor and decreases the power output of the turbine. To overcome this, a certain amount of energy is added to the working fluid to get a desired power output. There is a restriction of adding unlimited amount of fuel to increase the net power output. For a given amount of working fluid of air there is a limit to which fuel can be supplied. The fuel/air ratio has a limitation on the critical material temperature of the turbine blades. This problem introduces the two main design factors that govern the performance of gas turbine: stage efficiencies and “turbine inlet temperature” or the “firing temperature”.

Gas turbines are operated on Brayton thermodynamic cycle. These processes are characterized by four processes:

- 1-2: Isentropic Compression
- 2-3: Constant Pressure Heat Addition
- 3-4: Isentropic Expansion
- 4-1: Constant Pressure Heat Rejection

A sketch of typical gas turbine components is shown in Figure 1 and the corresponding temperature-entropy diagram associated with each thermodynamic state is shown in Figure 2

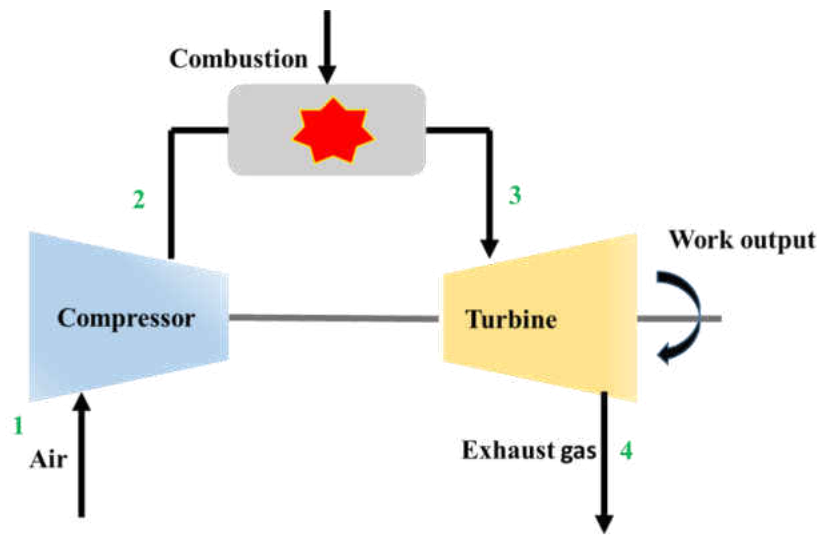


Figure 1 Components of a basic gas turbine

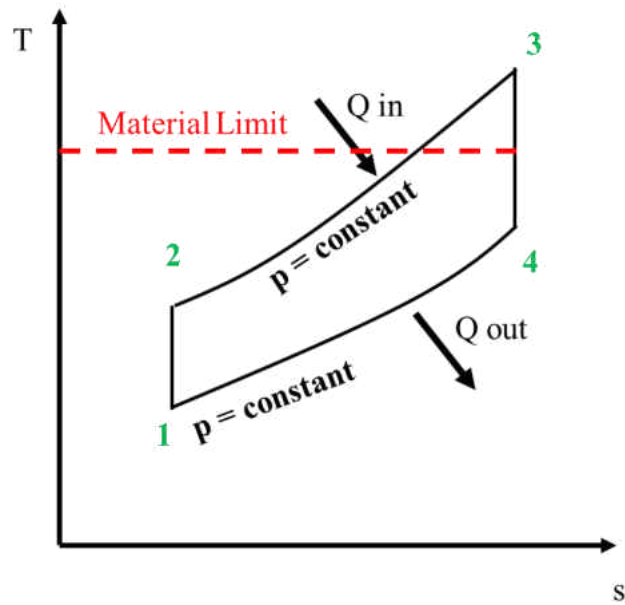


Figure 2 Temperature-entropy diagram of an Ideal Brayton Cycle

The steady flow energy equation from the Brayton cycle 1-2-3-4 (shown in equation 1) can be written as:

$$Q = (h_2 - h_1) + \frac{1}{2} (C_2^2 - C_1^2) + W \quad (1)$$

Where Q and W are the heat and work transfer rate. Assuming there is no difference in the change of kinetic energy between the inlet and the outlet of each component in the Brayton cycle we can write,

$$W_{12} = -(h_2 - h_1) = -c_p (T_2 - T_1) \quad (2)$$

$$Q_{23} = -(h_3 - h_2) = -c_p (T_3 - T_2) \quad (3)$$

$$W_{34} = -(h_3 - h_4) = -c_p (T_3 - T_4) \quad (4)$$

The cycle efficiency can be defined as:

$$\eta = \frac{W_{net}}{Q_{in}} = \frac{\text{net work output}}{\text{heat supplied}} = \frac{c_p (T_3 - T_4) - c_p (T_2 - T_1)}{c_p (T_3 - T_2)} \quad (5)$$

From the isentropic relation,

$$\frac{T_2}{T_1} = r^{\frac{(\gamma-1)}{\gamma}} = \frac{T_3}{T_4} \quad (6)$$

$$\text{Where } r = \frac{p_2}{p_1} = \frac{p_3}{p_4} \quad (7)$$

The expression for cycle efficiency expressed as:

$$\eta = 1 - \left(\frac{1}{r}\right)^{\frac{(\gamma-1)}{\gamma}}$$

Thus the efficiency depends on the pressure ratio and working fluid. It can be shown that the specific work output, w is a function of not only pressure ratio but also the maximum cycle temperature, T_3 .

$$W = c_p (T_3 - T_4) - c_p (T_2 - T_1) \quad (8)$$

The above expression can be reduced to,

$$\frac{W}{c_p T_1} = t \left(1 - \frac{1}{r^{\frac{\gamma-1}{\gamma}}} \right) - \left(r^{\frac{\gamma-1}{\gamma}} - 1 \right) \quad (9)$$

$$\text{Where } t = \frac{T_3}{T_1} \quad (10)$$

T_1 is ambient temperature and it cannot be increased. The value of T_3 can be increased to gain more power output. This temperature is often called the “firing temperature”. Early gas turbines usually have the value of t between 3.5 and 4, but with the advent of cooling mechanisms in air-cooled turbine blades the value of t can be raised to between 5-6 [1]

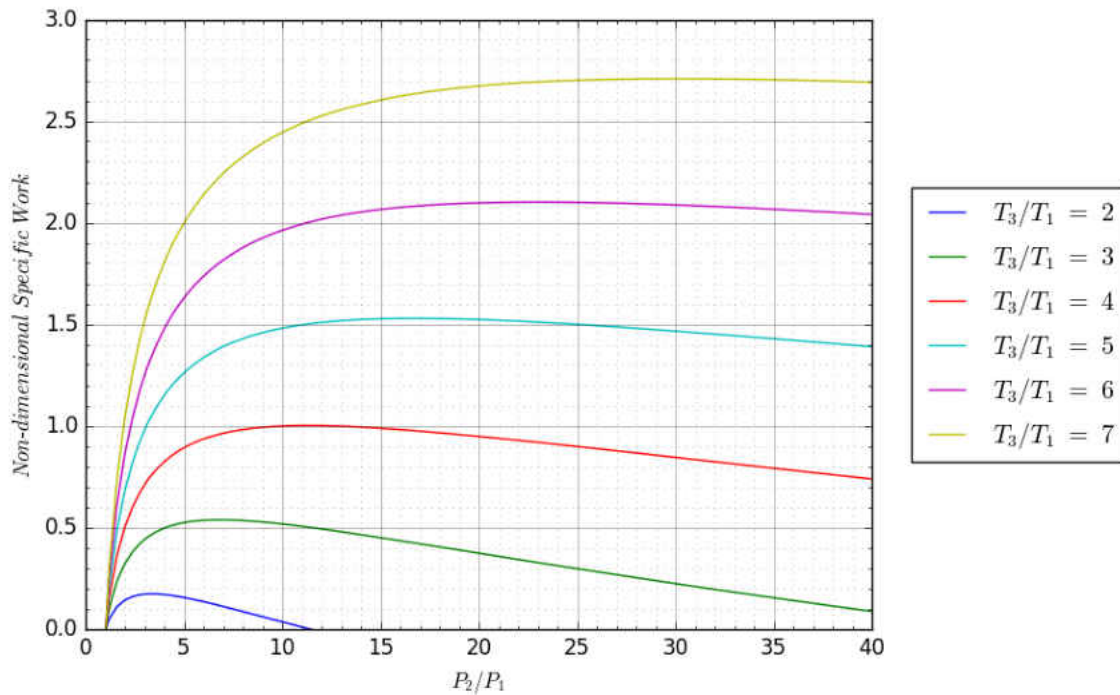


Figure 3 Non-dimensional work out and pressure ratio dependency

Thus, the motivation for raising the firing temperature can be seen, as this parameter drives the thermal efficiency. The current firing temperature has already exceeded the material allowable limit, 1900K, or even higher, in the first state of a gas turbine [2]. The high firing temperature could cause a failure in the turbine blades or vanes. With an aim to increase the engine life and preventing the blade material from being failing due to higher temperature, the concept of several cooling techniques in the turbine blade section has been introduced. As a result, the need for heat transfer into the turbine components also increases. To protect the critical components in the engine from being damaged under elevated temperature, cooling plays a pivotal role. A small increment of 50K in firing temperature can result in an 8-9% increase in power output and 2-4% improvement in the cycle efficiency [3]. Therefore, it is necessary to introduce a cooling mechanism to these blades in order to protect the material as the engine is run at high temperatures. A detailed overview of several cooling methods can be found in open literature for external as well as internal turbine blade cooling. These cooling techniques are accomplished by passing the compressor air through the blades which operate at a much elevated temperature. Both external cooling technique (film cooling) and internal cooling (convection and impingement cooling) are usually used to cool the various heated parts in the turbine and combustor section.

But cooling comes at a price. The compressor air is used as coolant to cool hot parts in the turbine otherwise this coolant would be used to generate power. The addition of coolant reduces the work output from the turbines. Bunker stated, “The use of 20 to 30% of this compressed air to cool the high pressure turbine presents a severe penalty on the thermodynamic efficiency unless the firing temperature is sufficiently high for the gains to outweigh the losses” [4]

Structure of an Impinging Jet

Because the turbine blades have a complex geometry, several cooling schemes have been introduced to cool the various parts of each blade. Among the different cooling techniques, impingement cooling produces some of the highest heat transfer coefficients. This is because the cooling is highly localized near the stagnation region of the impinging jets. Some examples of this include: turbine guide vanes, rotor blades, rotor disks, and combustor liners.

Two types of impinging jets are typically studied in the open literature: a) single round jet nozzle and b) array of impinging jets. The applications of impingement jets are not only limited to the gas turbine, but they are also, it is widely used in the electronic cooling, food packaging, etc. The structure of the single round impinging jet is different than an array of impinging jets. Because jet-to-jet interaction in an array of impinging jets causes completely different behavior, the knowledge from single jet impingement cannot be applied to an array of impinging jet system. That is why it is important to understand the fundamental structure of jets for both configurations.

A classic example of a wall-bounded flow is a single round impinging jet. Figure 4 shows a typical example of a single round impinging jet. Figure 5 shows the structure of an array of impinging jets.

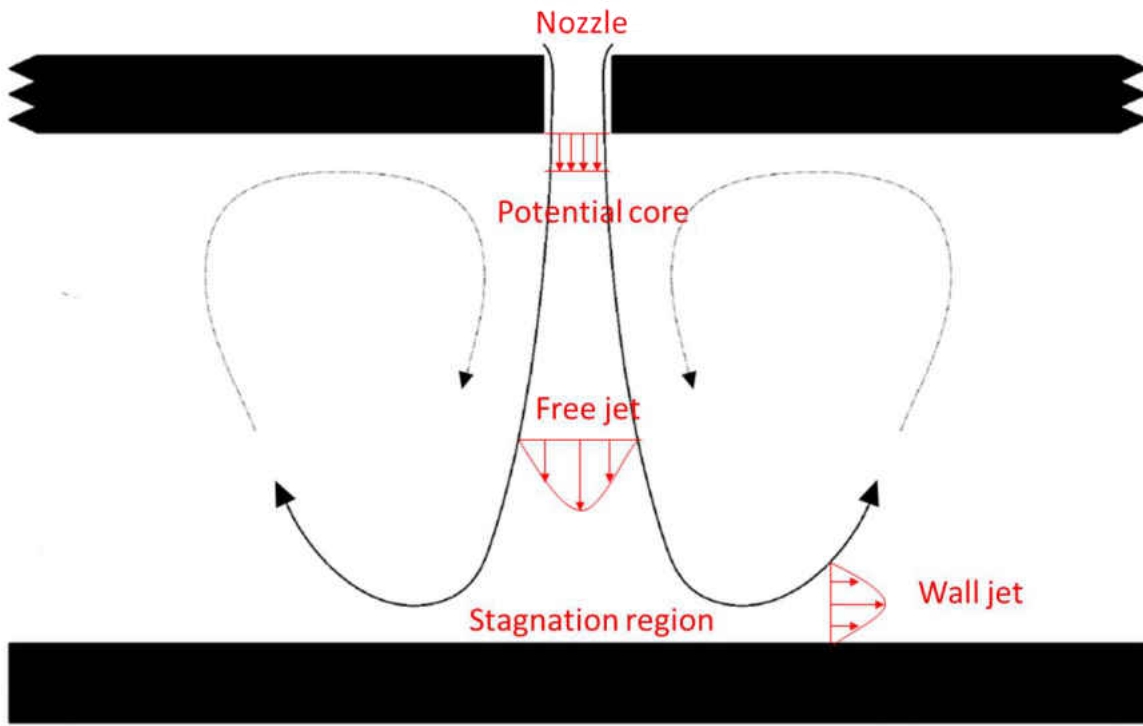


Figure 4 Structure of a single round impinging jet

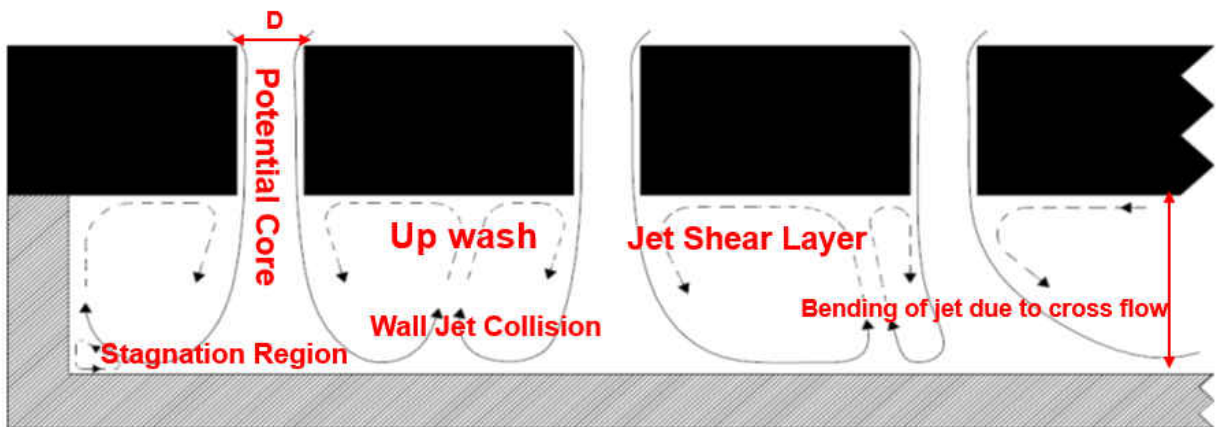


Figure 5 Structure of an array of impinging jet

In both the configurations several flow structures develop. Some of the common flow features for single jet and array of impinging jets are very similar. In impingement configuration jets are formed by fluid issuing from a pipe or nozzle into an unconfined or confined space and organized into:

I) Potential Core/Free Jet Region: In this region centerline velocity equals the jet exit velocity. The length of the potential core is defined up to where the velocity remains constant. The formation of jet shear layer, instability, and entrainment occurs in this region.

II) Stagnation Region: As the jet approaches the target wall, fluid velocity goes to zero near the target surface, and this area is called the stagnation region.

III) Wall Jet Region: This is the area where the flow starts to develop radially after impinging onto the wall and the boundary layer starts to grow.

The flow structure in an array of impinging jets is somewhat more complex than for single jet impingement due to the presence of neighboring jets. In addition to the potential core, stagnation region, and wall jet region like single jet fountain flow, upwash flow and wall jet vortices are observed as shown in Figure 5.

Literature Review

In the open literature a wide variety of impingement study has been done. The Array of impinging jets are widely used in industrial applications than single jet impingement. In this dissertation three types of impingement configurations are studied. These are:

1. Narrow wall impingement
2. Inline jet array impingement configuration
3. Curved surface impingement configuration

In general, the final goal of these geometric configurations is to gain a better heat transfer performance. In the literature review survey a summary of numerical work and flow visualization study related to jet impingement study is also included in a tabular fashion in the current study.

Narrow Wall Impingement Cooling

In the review study by Bunker [5], the current cooling technologies (shaped film cooling holes and thermal barrier coatings) have approached their limit and it is hindering the further increase of turbine inlet temperature. The limitation of these cooling techniques drives the introduction of new concepts of cooling in gas turbine blades. Impingement inside a narrow channel can be a potential way to implement near wall cooling of turbine blades and vanes as the narrow wall channel allows the coolant to flow closely to the heated surface. Figure 6 shows an example of an application of narrow wall cooling.

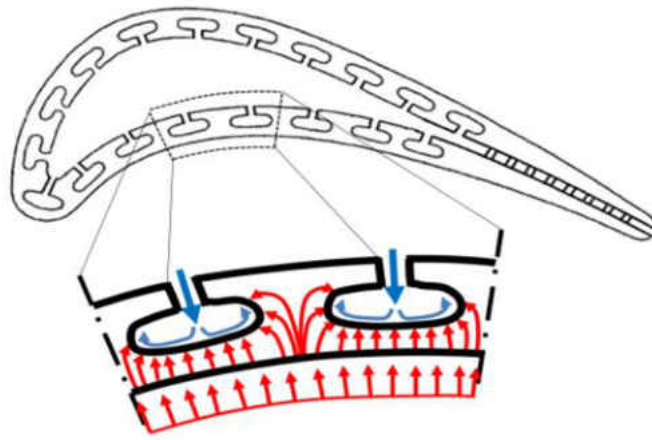
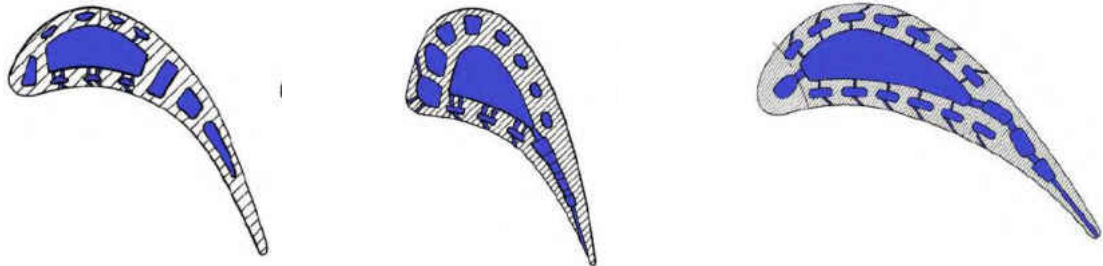


Figure 6 Narrow wall impingement cooling concept [6]

This cooling scheme becomes more practical from the advent of several advanced manufacturing techniques, including additive manufacturing. This technique is considered one of the most novel and innovative impingement cooling techniques. One of the benefits of this cooling technique is that with the same amount of mass flow four sides of the heated wall can be cooled simultaneously; hence this cooling is also sometimes called double wall cooling. Several industries have adopted this narrow wall cooling concept in their design, as shown in. Figure 7 and Figure 8.

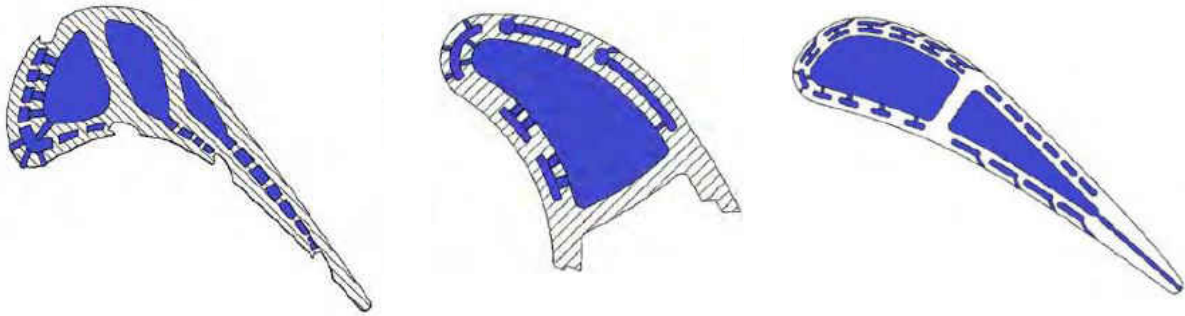


(a) Rolls-Royce [7]

(b) Rolls-Royce [8]

(c) United Technologies Corporation [9]

Figure 7 Turbine airfoils with narrow wall cooling configurations



(a) General Electric [10]

(b) Alstom Technologies Ltd
[11]

(c) Florida Turbine Technologies
[12]

Figure 8 Turbine airfoils with narrow wall cooling configurations

The above pictures have been adopted from [3]. Early works by Florschuetz et al. [13] [14] [15] presented different array of jet configurations and provided the correlations for area averaged Nusselt number with different stream wise X/D , spanwise Y/D , and different jet-to-target wall Z/D

spacing. A limited amount of work has been found focusing on a narrow wall impingement channel rather than a conventional wide jet array impingement configuration. The primary way this study is different from the class of impingement problems covered by the Florschuetz et al. correlation is that side walls alter the flow physics and contribute to overall heat transfer; the myriad of papers on large impingement arrays do not cover this topic. Gillespie et al. [16] studied the local heat transfer distribution of an integrally cast impingement cooling configuration. The Reynolds number tested based on jet diameter was in the range of 21,000-40,000. The jet hole arrangement was in a staggered manner and the spent air of the jets were drawn out through inline film cooling holes. Seven staggered jet holes and five inline film cooling holes were used for the study. Chambers et al. [17] investigated the heat transfer performance of nineteen staggered jets in a high aspect ratio cooling channel. The jet Reynolds number used in the experiment was 10,000-35,000. Both the jet plate and target plate heat transfer was studied. It was found that, as the crossflow builds up no augmentation of heat transfer was achieved at the downstream. The same geometry was tested by Chambers et al. [18] using elliptical shaped impingement hole rather than circular shape jet hole. It was reported that the elliptical shape enhanced the heat transfer. Chyu and Alvin [19] numerical study found that blade metal temperatures are greatly reduced when using a double wall cooling technique. Ricklick and Kapat [20] studied the effect of side walls in a narrow impingement channel. The study points out the side walls' significant contribution to the overall heat transfer capability of the impingement channel; Ricklick and Kapat [20] shows the side walls benefit from the buildup of crossflow as opposed to the target wall. More recently, Terzis et al. [3] studied a narrow impingement channel with jet staggering in the spanwise direction. It was determined that an inline pattern provided the highest area averaged Nusselt number values as the

crossflow has a larger impact on the staggered array. Side wall data was also provided; the side wall area averaged Nusselt number increased as the staggering distance increased due to the larger jet interaction with the neighboring wall. Claretti et al. [21] studied the relationship between target and sidewall surfaces of a single row impingement channel. His results suggest that when both the target and sidewall channels were taken into account the $Z/D=3$ channel provides the largest overall heat transfer rate through the target wall and sidewalls out of all the channel heights tested. Miller et al [22] investigated the effect of varying jet diameter on a rib-roughened target surface in a single row narrow impingent channel with five inline jets. Uysal et al [23] studied the effect of varying jet diameter in a narrow impingement channel with six inline holes. The jet Reynolds number in the study was 14,000-40,000. They found that the with constant jet diameter the heat transfer is more uniform than non-uniform jet diameters. No sidewall heat transfer data was reported. Fechter et al. [24] numerically studied the heat transfer characteristics of narrow impingement channels with five jets and compared them with the experimental heat transfer data. The study was done with jet Reynolds number ranging from 10,000-40,000. It was reported that the average heat transfer rates on the sidewalls as well as the impingement plate are about 25% and 40% lower than the target plate value respectively. Hossain et al. [25] studied the aerothermal investigation of a single row narrow wall impingement channel using PIV, TSP and CFD. Terzis et al. [26] performed an aerothermal investigation of a single row narrow wall impingement channel using PIV and LCT. A divergent impingement channel was investigated and compared to a uniform channel of the same open area ratio. Table 1 shows a summary

Table 1 Summary of narrow work impingement work

Authors	Number of Jets	Rows	L/D	X/D	Y/D	Z/D	Re_D (x10⁴)	Sidewall HT	Target Wall HT	Jet Plate HT	CFD	PIV
Gillespie et al. (1998)	7	1	1.25	4	7.5	1.25	21.-4.2	No	Yes	Yes	No	No
Chambers et al. (2005)	19	1	1.25	4.36	3.03	1.54	1-3.5	No	Yes	Yes	No	No
Uysal et al. (2006)	1	1	8.5	7.5	6.8	0.8,1.6,2.4	1.4-4	No	Yes	Yes	No	No
Ricklick et al. (2010)	15	1	1	5	4	1,3,5	1.7-4.5	Yes	Yes	No	No	No
Miller et al.(2013)	5	1	2	5	4	2,4	5-8	No	Yes	No	No	No

Authors	Number of Jets	Rows	L/D	X/D	Y/D	Z/D	ReD (x104)	Sidewall HT	Target Wall HT	LES	RANS	PIV
Trezis et al.(2013)	5	1	1	5,8	3,4,5,6	1,1.5,2,3	1-8.6	Yes	Yes	No	No	No
Claretti et al (2013)	15	1	1	5	4	3	1.5-4.5	Yes	Yes	No	No	No
Fechter et al.(2013)	5	1	1	5	5	1,3	1-4.5	Yes	Yes	No	Yes	No
Hossain et al. (2014)	15	1	1	5	4	3	3.0	No	Yes	No	Yes	Yes
Trezis et al. (2015)	5	1	1	6.66	5.5	2	1.4-4.5	No	Yes	No	No	Yes
Present Study	5	1	1	5	4	3	1.5	Yes	Yes	Yes	Yes	Yes

Array Impingement

Florschuetz et al. [13], [14].and [15] developed a correlation for array impingement heat transfer. The range of streamwise spacings (X/D) was 5-15, the range of spanwise spacings (Y/D) was 4, -8 and the range for jet-to-target wall spacings (Z/D) 1-3. Jet average Reynolds numbers ranged from 5,000 to 75,000. The Nusselt number was given in the form of:

$$Nu = A(Re_j)^m \left\{ 1 - B \left[\left(\frac{Z}{d} \right) \left(\frac{G_c}{G_j} \right) \right]^n \right\} * Pr^{\frac{1}{3}} \quad (11)$$

The value of these parameter (A, m, B) are given in [15].

The expressions to calculate flow distribution is given below from [15].

$$\frac{G_j}{G_j} = \frac{\beta N_c \cosh\left(\beta \left(\frac{x}{x_n}\right)\right)}{\sinh(\beta N_c)} \quad (12)$$

$$\frac{G_c}{G_j} = \frac{1}{\sqrt{2} C_D} \frac{\sinh\left(\beta \left(\frac{x}{x_n} - \frac{1}{2}\right)\right)}{\sinh\left(\beta \frac{x}{x_n}\right)} \quad (13)$$

$$\beta = \frac{C_D * \sqrt{2} * \frac{\pi}{4}}{\left(\frac{y_n}{d}\right) \left(\frac{z_n}{d}\right)} \quad (14)$$

$$x = x_n \left(i - \frac{1}{2} \right) \quad (15)$$

Weigand and Spring [27] summarized a detailed review on impingement cooling work focusing on the array impingement configuration. The review covers an in-depth discussion on factors influencing impingement heat transfer such as the effect of crossflow, jet-to-jet interaction, and separation distance between a jet and target plate in a multiple jet array.

Numerous papers have been published on array impingement jet configuration that cover a wide variety of testing parameters. The parameters that are included in the table are jet Reynolds number, streamwise spacing x/D , spanwise spacing y/D , and jet-to-target plate distance z/D . Also the the crossflow configurations are included in the table 2. Table 2 shows the trend in array impingement study in the published literature. Instead of summarizing each publication, the author has put together a summary table for these array impingement work to highlight the scope of current study. The parameters that are included in the table are Jet Reynolds number, streamwise spacing x/D , spanwise spacing y/D and jet to target plate distance z/D . Also the crossflow configurations are included in the table 2.

Table 2 Summary of literary review for array impingement work

Authors	Year	Crossflow Direction	Reynolds Number	x/D	y/D	z/D	Flow Physics Study	CFD Comparison
Kercher & Tabakoff [28]	1970	min-max	300-30,000	3.1-12.5	3.1-12.5	1-4.8	No	No
Hollworth and Berry [29]	1978	max	3,000-35,000	10-25	10-25	1-25	No	No
Metzger D.E et al. [30]	1979	max	5,000-25,000	10	8-10	1-3	No	No
Florschuetz et al. [14]	1981	max	5,000-70,000	5-15	4-8	1-3	No	No
Andrews, G.E. [31]	1987	Unknown	1,000-65,000	5-10	4-8	1-3	No	No
Obot and Trabold, [32]	1987	mid-min-max	1,000-21,000	10	10	4.5	No	No
Van Treuren et al. [33]	1994	max	10,000-40,000	8	8	1	No	No
Huang et al. [34]	1998	mid-max	4,800-18,300	4	4	3	No	No
Son et al. [35]	2001	max	19,500-29,500	3-4.8	3.75-6	1.875-3	No	No
Azad et al. [36]	2002	mid-max	4,850-18,300	2.54	2.54	3	No	No
Dano et al. [37]	2004	max	8,500-15,900	unknown	unknown	2-4	Yes	No
Yan W.M. et al. [38]	2005	mid-max	1,500-4,500	6	3	3-9	No	No
Geers et al. [39]	2005	max	5,000-20,000	unknown	2-6	3-10	yes	yes
Park J. et al. [40]	2007	max	5,000-20,000	2,4,6,10	2,4,6,10	1,2,5	No	No
Goodro M. et al. [41]	2008	max	8,200-30,500	8,12	8,12	3	No	No
Esposito et al. [42]	2009	max	20,000-60,000	5	5	3-6	No	No
Katti & Prabhu [43]	2009	max	3,000-7,000	3-5	5	1-3	No	No
Ricklick & Kapat [20]	2011	max	17,000-45,000	5	4	1,3	No	No
Spring S. et al. [44]	2010	min-mid-max	17,000-34,000	5	5	3-5	No	No
Xing Y. et al. [45]	2010	mid-min-max	17,000-34,000	5	5	3-5	No	No
Chi et al. [46]	2013	max	10,000-30,000	4	8	3	No	yes
Fetcher et al. [24]	2013	max	10,000-40,000	5	5	1-3	No	Yes

Curved Surface Impingement

As stated in [47], a lot of published literature has been focused on jet impingement on a flat plate configuration. In real turbine applications, heat transfer by impingement must also occur on a curved surface. Several studies have been done on curved surface impingement with small radius of concave surfaces, representative of a typical turbine airfoil leading edge [48], [49] and [50]. The study on jet impingement with a large radius of curvature is scarce. Due to complex geometries in actual gas turbine application where jet impinges on a large curvature geometries. Some examples are combustion liner or turbine blade midchord.

Weigand and Spring [27] mentioned that impingement cooling coupled with turbulators has the potential to enhance heat transfer. Even though the concept is novel, the author recommends further research on this topic. Gau and Lee [51]. studied impingement flow structure and heat transfer along rib-roughened walls with Reynolds number varying from 2,500 to 11,000 and jet to target plate spacing varying from 2 to 16. With these modifications, the flow structures and heat transfer results were found to be different than that of a smooth plate. Hansen and Webb [52] experimentally examined the impingement heat transfer where the target surface was modified with arrays of fin-type extensions with jet Reynolds number ranging from 4,700 to 24,000.

The results showed that the enhancement factor ranging from 1.4 to 4.5 can be obtained using different fin geometries. Chang et al. performed a series of experiments [53, 54] on impingement heat transfer from a rib-roughened surface within an array of circular jets. It was found that the relative position of the jet hole to the ribs has a great effect on impingement heat transfer, and the most effective location of a jet hole can be achieved by placing a jet in-between two ribs.

Annerfeldt et al. [55] performed a detailed experimental investigation of impingement cooling with turbulators. The jet Reynolds number varied from 20,000 to 65,000. The study used four different surface enlarging elements; triangle, wing, cylinder and dashed rib. The ribs were placed such that the jets were protected from crossflow. It was found that for all geometries the Nusselt number enhancement is modest and increased by a factor of 1-1.13 when compared to flat plate results. Andrews et al. [31] investigated the influence of heat transfer in the presence of ribs. Rectangular slotted ribs were used with a 50% blockage to the crossflow. It was found that 50% blockage resulted in higher enhancement of impingement heat transfer. Son et al. [56] investigated heat transfer distribution and cooling performance by installing roughness elements in an impingement cooling system. A hexagonal rim was placed in the low heat transfer region (midway between two impinging jets). El-Gabry and Kaminski [57] experimentally investigated the local heat transfer distribution at jet Reynolds number ranging from 15,000 to 35,000 on smooth and roughened surfaces under an array of impinging jets. The results showed that utilizing roughed surface heat transfer can enhance significantly. Xing et al. [45] carried out an experimental and numerical investigation of an inline jet impingement heat transfer with micro-rib roughened surface for different crossflow schemes. The experiments were conducted at jet Reynolds number varying from 15,000-35,000 .It was found that the presence of micro ribs can enhance up to 9.6% for maximum crossflow configuration. Spring et al. [44] performed an experimental and numerical investigation of heat transfer characteristics from arrays of impinging jets with surface ribs for the jet Reynolds number of 35,000 and for jet to target plate distance of 3D. The study reported that high accuracy of averaged quantities can be obtained from CFD. For averaged values, an accuracy of around 10% is achievable from CFD, emphasizing CFD can be useful for the prediction of jet

impingement heat transfer. Miller et al. [22] investigated the effect of surface roughness in a single row narrow impingement channel. The results showed that among the different types of turbulators tested the X-shaped rib yields the best heat transfer performance. Brakmann et al. [58] extended the work done by Xing et al. [45] and Spring et al. [44] and studied the effect of cubic micro-features on the target surface within an array of the impinging jet system.

Table 3 shows a brief summary of work done on the impingement heat transfer with turbulators and the scope of the present work.

Table 3 Summary of impingement work with turbulators

Authors	Year	X/D	Y/D	Z/D	Re_j	Rib Location
Trabold and Obot [32]	1987	6	4	2-16	1300-21,000	Within Impingement Array
Gau and Lee [59]	1992	N/A	N/A	2-16	2500-11,000	Within Impingement Array
Hansen and Webb [52]	1993	N/A	N/A	5- 14	4700-24,000	Within Impingement Array
Chang et al. [53]	1998	5,7.5,10	5,7.5,10	1.5,2,3,4,5	7000-15,000	Within Impingement Array
Annerfeldt et al. [55]	2001	5	5.77	0.82,1.73,2.45	20,000-65,000	Within Impingement Array
Son et al. [56]	2005	3-3.7	3.75-4.6	1.88-3	17,000-41,000	Within Impingement Array

Authors	Year	X/D	Y/D	Z/D	Re_j	Rib Location
El Gabry and Kaminski [57]	2005	5	5	1,2	10,000-35,000	Within Impingement Array
Andrews et al. [31]	2006	1.86- 4.66	1.9	1.1-2.75	10,000	Within Impingement Array
Xing et al. [45]	2010	5	5	3-5	15,000-35,000	Within Impingement Array
Spring et al. [44]	2012	5	5	3	35,000	Within Impingement Array
Miller et al. [22]	2013	4	4	2	50,000-80,000	Within Impingement Array
Brakmann et al. [58]	2015	5	5	3-5	15,000-35,000	Within Impingement Array
Present Study	2016	5.79	4.49	3	55,000- 125,000	Post Impingement Area

Harrington et al. [60] investigated the effect of wall curvature on impingement heat transfer distribution. The results obtained from the curved surface was compared with the flat surface. It was reported that target wall curvature caused higher heat transfer distribution. The objective of the current study is to investigate the effect of rib turbulators on heat transfer distribution in the post-impingement area for a curved surface. Annerfeldt et al. [55] stated that in order to match engine representative condition for modern gas turbine application, the Reynolds number should be at least 60,000. In the open literature, data reported for impingement cooling with turbulators at large jet Reynolds number is very scarce. It was found in the open literature that ribs are located within the array of impingement jet arrays. The current study differs from the past impingement cooling work because the ribs are located in the post-impingement area where the heat transfer degrades significantly. The rib height is such that it corresponds to channel blockage ratio of 4.76%. For all the configurations, maximum crossflow scheme was used as this condition has the highest potential for heat transfer benefits [32]. CFD calculations were performed and compared with experimental results for the highest jet average Reynolds number case ($Re_j=125,000$).

Table 4 Summary of turbulator work with one wall ribbed configuration

Authors	Year	Re_{D_h}	P/e	e/ D_h	Rib type	Flow condition: Fully Developed	No. of Ribbed Walls
Chandra et al. [61]	1995	10,000-80,000	8	.0625	90 ⁰	Yes	1
Momin et al. [62]	2002	2,500-18,000	10	.022	45 ⁰	Yes	1
Maurer [63]	2008	90,000-500,000	10	.022	45 ⁰	Yes	1
Maurer [63]	2008	90,000-500,000	5	.02	45 ⁰	Yes	1
Present Study	2016	100,000-200,000	15	.0264	90 ⁰	No	1
Present Study	2016	100,000-200,000	15	.0264	45 ⁰	No	1

In the downstream region of the current study, the flow in the post-impingement area is similar to internal duct cooling but is not a fully developed flow. As a reference, Table 4 is a summary of literature review on internal duct cooling with turbulator work, which is similar to the post-impingement area of the current study. However, the rib configurations studied in the current study do not fall into a proper validation case that fits the current testing parameters listed in Table 2 ($Re_{Dh}, P/e$ and e/D_h , flow condition). Hence, all the data was compared to the Dittus-Boelter correlation to understand the enhancement caused by the turbulators.

Summary

The currently published results in narrow impingement channels have focused on surface measurements and presentation of Nu-distribution. None of these published papers present any measured flow fields. Hence a lot of conjecture has been made regarding the behavior of the flow field in order to explain the observed variations of heat transfer coefficients on the surfaces. The primary contribution of this study is to connect a measured flow field to the measured surface heat transfer.

For general multiple row impingement configurations (i.e. not considering narrow channels), there are a limited number of publications which consider both the flow field and surface heat transfer data. One of the recent and most expansive ones is presented by Geers et al. [39]. Currently, it is the only available in-depth flow visualization work on array impingement. Even then the focus was on flow structure and thermal imprint, and not on comparison against standard correlations. In fact, Nu-results were not presented in a way that one can readily compare the results with the Florschuetz correlation. Again, it should be noted that the paper [39] considered a 3x3 array of

impinging jets, and not a narrow impingement channel. Even for their multi-hole array impingement, the paper stated that typical RANS turbulence models failed to predict heat transfer and flow field data. Even though there are few studies on single jet impingement using LES, according to author's knowledge no LES work in array impingement configuration was done prior to this work.

CHAPTER 2: OBJECTIVE & MOTIVATION

Objective of the Present Study

The objective of the current study is to provide a better understanding of impingement heat transfer in relation to flow physics associated with it. As heat transfer is basically a manifestation of the flow, and most of the flow in real engineering applications is turbulent, it is very important to understand the dynamics of flow physics in an impingement problem. Since impingement itself is a broad topic, effort is being made to narrow it down to three particular geometric configuration (a narrow wall impingement configuration, an array impingement configuration and a curved surface impingement configuration) that show up in a typical gas turbine impingement problem in relation to heat transfer. These three different types of impingement configurations are widely used in a typical gas turbine cooling application. In order to understand these problems, a three-pronged approach has been implemented in each of these cooling configurations.

- Spatial heat transfer distribution to understand the thermal imprint on the target surface using Temperature Sensitive Paint (TSP)
- Time accurate flow physics data using Particle Image Velocimetry (PIV)
- RANS CFD comparison with the experimental data and Large Eddy Simulation (LES) analysis in a single row narrow impingement channel

This three-pronged approach was adopted in order to connect the flow physics and heat transfer behavior, data obtained from the experiment would result in understanding the flow mechanism

that goes in an impingement channel. Most of the studies in the impingement are focused on heat transfer performance of the cooling channels hence the true structure of flow mechanism and fidelity of the CFD models are not completely understood. This dissertation makes an effort to bridge this gap. Another objective of the current study is to emphasize the importance of accurate flow physics data that is lacking in the impingement study, which can give a lot of information about flow physics. Finally, the accuracy of LES and RANS is compared with experimental data to understand the shortcoming of the typical RANS models.

Novelty

Following are aspects of the various ways the current study is unique and novel over previously published impingement studies

- The first ever flow visualization study in a single row narrow impingement channel using PIV
- Flow physics are connected to heat transfer behavior
- RANS ability to predict the heat transfer and flow physics
- The underlying reasons of notorious behavior of RANS for predicting impingement heat transfer
- First attempt to implement Large Eddy Simulation in a single row narrow Impingement channel

- Benchmark data for a single row narrow impingement channel for improving existing turbulence model
- Feasibility of LES in impingement channel for future industrial application

Intellectual Contribution

The flow physics in an impinging jet is very complex and is not fully understood yet [64]. The flow field in an impingement problem is comprised of three different distinct regions: a free jet with a potential core, a stagnation region where the velocity goes to zero as the jet impinges onto the wall, and a creation of wall jet region where the boundary layer grows radially outward after impinging. Hence impingement problems are difficult to simulate numerically using the conventional RANS models. It is worth noting that the typical RANS model contains a number of calibrated constants, and these have been formulated with respect to relatively simple shear flows. As a result, typically these isotropic eddy viscosity models fail in predicting the correct heat transfer values and trends in impingement problems where the flow is highly anisotropic. A relatively recent review paper [65] commented that common RANS-based models over predict stagnation heat transfer coefficients by as much as 300% when compared to measured values. Even the best of the models, the $v^2 - f$ model, can be inaccurate by up to 30%.

Even though there is a myriad number of experimental and numerical works published on single jet impingement, the knowledge gathered from these works cannot be applied to real engineering impingement cooling applications as the dynamics of flow changes completely. Olsson and Fuchs [66] reported that Large Eddy Simulation (LES) can provide results that are within 10% of measured values with the choice of appropriate subgrid scale (SGS). Dewan et al. [65] further

underlines the lack of experimental flow physics data on multiple jet impingement and the authors emphasized how important it is to have experimental data to validate CFD tools and to determine the suitability of different SGS models.

In the open literature there is not enough study where experimental heat transfer and flow physics data are combined to explain the behavior for gas turbine impingement cooling application. The experimental flow field and heat transfer data from this work will be analyzed to understand the relationship between flow characteristics and heat transfer for the three types of novel geometry mentioned above.

There has not been any effort made on to implement LES technique on array impingement problems. Nowadays with growing computational power and resources, CFD is widely used as a design tool. To support the data gathered from the experiment, LES is carried out in narrow wall impingement cooling configuration. The results will shed light on more accurate information on impingement flow physics phenomena where experimental techniques are limited and the typical RANS models yields erroneous results.

Dissertation Research Impact

This research highlights the importance of understanding flow physics in impingement heat transfer applications. According to the author's knowledge, this is the first work in a narrow wall impingement cooling configuration where flow and heat transfer are connected together via particle image velocimetry (PIV), computational fluid dynamics (CFD) and heat transfer analysis using temperature sensitive paint (TSP). Prior to this work, no study was found where a Large Eddy Simulation (LES) technique was validated against the experimental data in array

impingement cooling channels. The results from this work reveal the potential of implementing LES in impingement cooling channels and highlights the accuracy of LES as a reliable design tool for future impingement cooling studies.

CHAPTER 3: INVESTIGATION TECHNIQUES

Temperature Sensitive Paint

Temperature Sensitive Paint (TSP) is a combination of luminescent molecules and a polymer binder. The surface for testing can be painted with TSP and the result would be a temperature distribution on the surface from this technique. The painted surface is illuminated with 460nm wavelength light in order to excite the molecule. Once the molecules are excited with the proper wavelength, the molecules returns to its original state by emitting larger wavelength. This process is graphically represented in the Jablonski diagram in Figure 9

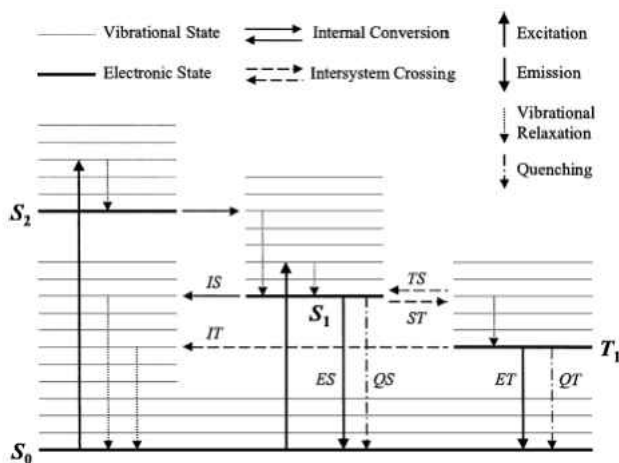


Figure 9 Jablonski energy level diagram adopted from [67]

The calibration curve for TSP consists of intensity ratio vs temperature difference. The intensity of the painted surface is recorded with a PCO CCD camera of resolution 1600X1200 pixels. Once the calibration curve is formed these are applied to the test section measurement. Before the experiment, the cold surface intensity is recorded at know temperature condition. Then the surface is heated with a hear source, and the unknown term in the whole process is the temperature with known intensities for the heated surface. Applying the calibration curve in the whole process gives a surface temperature distribution. This entire process of obtaining temperatures from the TSP calibration curve and then later heat transfer coefficients is performed by means of in-house developed MATLAB codes.

Extensive research has been completed on TSP and PSP (Pressure Sensitive Paint) and the author suggests Sullivan and Liu [68] and Liu [67] as thorough literature on TSP and PSP properties and characteristics for any who may wish to learn more.

Particle Image Velocimetry

Particle Image Velocimetry (PIV) is a non-intrusive measurement technique which is used to measure the detailed flow field of the area of interest. The concept of PIV is, seed particles (0.5 μm - 5 μm in diameter) are injected into the fluid medium. This particle laden flows acts as fluid tracers and follow the motion of the fluid. The size of the particles is small enough such that they don't change the flow physics of the flow to be investigated. These seed particles are illuminated in a 2D plane by a very thin light sheet using a combination of lenses and a high power Nd:YAG laser. The illuminated flow is then recorded in quick succession at two instances within a very short time duration (10-20 μs). Thus an image pair of particle motion is captures. By measuring

the particle displacement during the two image acquisition and the time interval between the two images the particle velocity can be estimated. Within a specified region (interrogation region) the most probable displacement is estimated through cross-correlation of the image pairs. The whole process ultimately results in a qualitative 2D velocity field over a plane where the laser sheets are illuminated.

Reynolds Averaged Navier-Stokes Equation (RANS)

The author has collected information from sources such as [69], [70], [71], [72], [73], [74], [75], [76], [77], [78], [79] for this section. Turbulence is one of the most complicated phenomena to understand and solve correctly. A fluid motion is considered to be turbulence if it is rotational, intermittent, chaotic and dissipative. The system of equation that governs the turbulent flow can be described by the Navier-Stokes equations. The instantaneous continuity and Navier-Stokes momentum transport equations in Cartesian tensor notation and using the repeated suffix summation convention are given by:

$$\frac{\partial \rho}{\partial t} + \frac{\partial}{\partial x_j} (\rho u_j) = 0 \quad (16)$$

The momentum equation for the x_i -component of velocity u_i

$$\frac{\partial \rho u_i}{\partial t} + \frac{\partial \rho u_i u_j}{\partial x_j} = \frac{\partial p}{\partial x_j} + \frac{\partial \sigma_{ij}}{\partial x_j} + F_i \quad (17)$$

Scalar conservation:

$$\frac{\partial \rho \varphi}{\partial t} + \frac{\partial \rho \varphi u_j}{\partial x_j} = \frac{\partial}{\partial x_j} \left(\tau_\varphi \frac{\partial \varphi}{\partial x_j} \right) + \frac{\partial p}{\partial t} + u_i \frac{\partial p}{\partial x_i} + S_\varphi \quad (18)$$

σ_{ij} is called the stress tensor components due to deformation and bulk dilation. For Newtonian fluids the instantaneous deformation stress is [76]:

$$\sigma_{ij} = \mu \left(\frac{\partial u_i}{\partial x_j} + \frac{\partial u_j}{\partial x_i} \right) + \left(\mu^b - \frac{2}{3} \mu \right) \delta_{ij} \frac{\partial u_l}{\partial x_l} \quad (19)$$

and the equation of state:

$$p = p(\rho, T) \quad (20)$$

The above equations (16-20) describe the mathematical representation a turbulent flow at a particular instant. These equations are a representation of every turbulent flow. In order to investigate the effect of fluctuations on the mean flow properties, the equations for turbulence are obtained by Reynolds decomposition. This is achieved by applying replacing the flow variables by the summation of the mean and fluctuating components.

$$\phi = \bar{\phi} + \phi' \quad (21)$$

The flow property is defined as:

$$\bar{\phi} = \frac{1}{\Delta t} \int_0^{\Delta t} \phi(t) dt \quad (22)$$

The time average of the fluctuating components is by definition zero.

$$\bar{\phi}' = \frac{1}{\Delta t} \int_0^{\Delta t} \phi'(t) dt \quad (23)$$

Using equations (21-23) and applying it in equations (16-20) the equations for mean flow can be obtained.

The continuity equations for mean flow:

$$\frac{\partial \bar{\rho}}{\partial t} + \frac{\partial}{\partial x_j} (\bar{\rho} \bar{u}_j) = 0 \quad (24)$$

The mean momentum equation:

$$\frac{\partial \overline{\rho u_i}}{\partial t} + \frac{\partial \overline{\rho u_i u_j}}{\partial x_j} + \frac{\partial \overline{\rho u_i' u_j'}}{\partial x_j} = -\frac{\partial \overline{p}}{\partial x_j} + \frac{\partial}{\partial x_j} \left[\mu S_{ij} + \left(\mu^b - \frac{2}{3} \mu \right) S_{11} \delta_{ij} \right] - \left[\frac{\partial \overline{\rho' u_i'}}{\partial t} + \frac{\partial \overline{\rho' u_i' u_j'}}{\partial x_j} + \frac{\partial \overline{\rho' u_j' u_i'}}{\partial x_j} + \frac{\partial \overline{\rho' u_i' u_j'}}{\partial x_j} \right] + f_i \quad (25)$$

It is important to note that the mean momentum equation is very similar to the instantaneous momentum equation but in the process of applying Reynolds decomposition some new terms have evolved in the mean momentum equation. These are products of fluctuating velocities and are responsible for convective momentum transfer due to different scales in the turbulent flow. The extra term that has arisen due to the time averaging process are called Reynolds stresses. The six additional stresses are called Reynolds stresses. Three normal stresses and three shear stresses. The respective variance of the x,y,z velocity fluctuations are responsible for producing normal stresses. Since variance is the squared deviation of the velocity fluctuations, it is never zero. The shear stress are correlation between two different velocity components.

Where

$$S_{ij} = \left(\frac{\partial u_i}{\partial x_j} + \frac{\partial u_j}{\partial x_i} \right); S_{ii} = \frac{\partial \overline{u_i}}{\partial x_i} \quad (26)$$

Time averaged Scalar equation:

$$\frac{\partial \overline{\rho \phi}}{\partial t} + \frac{\partial \overline{u_j \rho \phi}}{\partial x_j} + \frac{\partial \overline{\rho u_j' \phi'}}{\partial x_j} = \frac{\partial}{\partial x_j} \left(\tau_\phi \frac{\partial \overline{\phi}}{\partial x_j} \right) + \frac{\overline{Dp}}{Dt} - \left[\left(\frac{\partial \overline{\rho' \phi'}}{\partial t} + \frac{\partial \overline{u_j \rho' \phi'}}{\partial x_j} \right) + \frac{\partial}{\partial x_j} \left(\overline{\rho' u_j' \phi'} + \overline{\rho' u_j' \phi'} \right) \right] + \overline{S_\phi} \quad (27)$$

Mean equation of state:

$$p = R\bar{\rho T} = R(\bar{\rho T} + \bar{\rho' T'}) \quad (28)$$

With the improvement of computer power several numerical models known as “Turbulence model” are available to solve this complicated flow. Several turbulence models exist in today's engineering applications to solve turbulent flow. These are called Reynolds-averaged Navier-Stokes (RANS) equations. In real life all the flow in engineering applications is turbulent. Predicting the accurate behavior of a turbulent flow is the goal of a turbulence model. Turbulence is a three-dimensional, unsteady in nature. Hence solving this problem accurately is almost impossible. Turbulence can be thought of as an eddy. There is a wide range of eddies in a turbulent flow.

k-ε Turbulence Model

The $k - \epsilon$ is one of the most widely used turbulence models for engineering applications. A single length and velocity scale are used to describe this particular two-equation model. The Reynolds-averaged momentum equation can be written as:

$$\frac{\partial \bar{u}_i}{\partial t} + \bar{u}_j \frac{\partial \bar{u}_i}{\partial x_j} = -\frac{1}{\rho} \frac{\partial \bar{p}}{\partial x_i} + \frac{\partial}{\partial x_j} \left(\nu \frac{\partial \bar{u}_i}{\partial x_j} - \overline{u'_i u'_j} \right) \quad (29)$$

As can be seen from the equation, it is that the time-averaged momentum equations yield six additional unknown equations. These are: $\overline{u'^2}$, $\overline{v'^2}$, $\overline{w'^2}$, $\overline{u'v'}$, $\overline{u'w'}$, $\overline{v'w'}$. These Reynolds stresses are nonlinear and need to be modeled. Since the Navier-Stokes govern only velocity and pressure of the fluid flow, the Reynolds stress terms must be correlated with the mean flow by removing the fluctuation velocity component. This is called the closure problem.

In two equation models, the Reynolds averaged momentum equation is closed using Boussinesq eddy viscosity hypothesis. This hypothesis states that there exists a correlation between the viscous stresses and Reynolds stresses on the mean flow. Newton's law of viscosity states that viscous stresses are proportional to the rate of deformation of fluid elements. For an incompressible fluid

$$\tau_{ij} = \mu \left(\frac{\partial u_i}{\partial x_j} + \frac{\partial u_j}{\partial x_i} \right) \quad (30)$$

Boussinesq proposed that Reynolds stresses is proportional to the mean rate of deformation. Again for an incompressible fluid:

$$\tau_{ij} = -\overline{\rho u'_i u'_j} = \mu_t \left(\frac{\partial \bar{u}_i}{\partial x_j} + \frac{\partial \bar{u}_j}{\partial x_i} \right) - \frac{2}{3} \rho k \delta_{ij} \quad (31)$$

To balance the equation a one third term is allocated at the right hand side of the expression. This also implies that it is an isotropic assumption. The turbulent eddy viscosity, ϑ_t is computed from a velocity and length scale. The hypothesis behind this is by equating a diffusion process to the turbulent convective mixing process, it can be shown that the eddy viscosity is proportional to the product of the turbulent velocity scale and the length scale.

The diffusion process time scale

$$\frac{l^2}{\vartheta_t} \sim \frac{l}{u} \quad (32)$$

$$\vartheta_t \sim l * u \quad (33)$$

The velocity is calculated from the turbulent kinetic energy equation $u \sim k^{0.5}$. The length scale is determined from the dissipation, $\varepsilon \sim \frac{k^{3/2}}{l}$. The process of describing the entire energy cascade

process using a single length and velocity scale is one of the major drawback of two equation model.

Finally the eddy viscosity coefficient becomes,

$$\nu_t = C_\mu \frac{k^2}{\varepsilon} \quad (34)$$

Where C_μ is a universally constant for high Reynolds number.

The instantaneous turbulent kinetic energy can be expressed as:

The mean turbulent kinetic energy can be expressed as:

$$k = \frac{1}{2} \overline{u_i u_i} = \frac{1}{2} (\overline{u^2} + \overline{v^2} + \overline{w^2}) \quad (35)$$

The exact transport equation of the mean turbulent kinetic energy can be written as:

$$\frac{\partial k}{\partial t} + \overline{U_k} \frac{\partial k}{\partial x_k} = - \overline{u_i u_k} \frac{\partial U_i}{\partial x_k} + \frac{\partial}{\partial x_k} \left[\nu \frac{\partial k}{\partial x_k} - \overline{u_i u_i u_k} - \frac{1}{\rho} \overline{p u_i} \delta_{ik} \right] - \nu \overline{\frac{\partial u_i}{\partial x_k} \frac{\partial u_i}{\partial x_k}} + \frac{P}{\rho} \left(\frac{\partial u_i}{\partial x_j} + \frac{\partial u_j}{\partial x_i} \right) \quad (36)$$

In a concise form the above expression can be written as:

$$\frac{Dk}{Dt} = P_k + D - \varepsilon + PS \quad (37)$$

The pressure-strain (PS) is usually neglected in $k - \varepsilon$ model. Each and every term in the above equation has a physical meaning and significance.

$P_k = - \overline{u_i u_k} \frac{\partial U_i}{\partial x_k}$: is called the production term. Turbulence is generated through this term. This term also can be interpreted as production of turbulent kinetic energy by mean flow velocity gradient.

$D = \frac{\partial}{\partial x_k} \left[\nu \frac{\partial k}{\partial x_k} - \overline{u_i u_i u_k} - \frac{1}{\rho} \overline{p u_i} \delta_{ik} \right]$: called the diffusion of turbulent kinetic energy by various mechanism. The first term is called the molecular diffusion term or viscous diffusion term. This term is closed and does not require modelling. The second and third terms are called the turbulent

transport momentum and pressure-velocity gradient correlations respectively. The turbulence convection and pressure diffusion are not closed and needs to be modeled. Most commonly they are modeled together using the generalized gradient diffusion hypothesis by Daly & Harlow (1970),

$$\overline{u_i u_l u_k} - \frac{1}{\rho} \overline{p u_l} \delta_{ik} = \frac{\partial}{\partial x_k} \left(C_s \frac{\varepsilon}{k} \overline{u_l u_k} \frac{\partial \overline{u_i u_k}}{\partial x_k} \right) \quad (38)$$

$\varepsilon = \overline{\frac{\partial u_l}{\partial x_k} \frac{\partial u_l}{\partial x_k}}$: called the turbulent dissipation or the dissipation of turbulent kinetic energy.

Turbulent dissipation happen with the correlation of the products of fluctuating velocity gradient. Similarly, from exact dissipation equation a model dissipation equation can be found. Details of the exact dissipation equation can be found “Fundamentals of turbulence modeling”.

$$\frac{Dk}{Dt} = \frac{\partial}{\partial x_k} \left(C_k \frac{k^2}{\varepsilon} \frac{\partial k}{\partial x_k} + \vartheta_t \frac{\partial k}{\partial x_k} \right) - \overline{u_l u_k} \frac{\partial U_l}{\partial x_k} - \varepsilon \quad (39)$$

$$\frac{D\varepsilon}{Dt} = \frac{\partial}{\partial x_k} \left(C_\varepsilon \frac{k^2}{\varepsilon} \frac{\partial \varepsilon}{\partial x_k} + \vartheta_t \frac{\partial \varepsilon}{\partial x_k} \right) - C_{\varepsilon 1} \frac{\varepsilon}{k} \overline{u_l u_k} \frac{\partial U_l}{\partial x_k} - C_{\varepsilon 2} \frac{\varepsilon^2}{k} \quad (40)$$

Total of eleven equations for eleven unknowns needs to be solved for a two equation model.

κ - ω Turbulence Model

Wilcox and Rubesin et al. [69] developed a two equation model called $k - \omega$ turbulence model. Two transport equations are used in this model. One is the turbulent kinetic energy and the second is the mean vorticity. The mean vorticity determines the length scale of the turbulence. The turbulent kinetic energy determines the velocity scale of the turbulence. Details of the $k - \omega$ model is can be found in [73]. One of the benefit of $k - \omega$ over $k - \varepsilon$ is that the model can be used

directly down to the wall through viscous sublayer, hence to model does not require any extra damping functions.

Reynolds Stress Turbulence Model (RSM)

Reynolds stress modelling are also known as second order modelling. The pressure strain effects are incorporated in RSM which does not appear in $k - \epsilon$ model. The pressure-strain correlations term primarily govern the anisotropy of the flow. From the experimental data it was also found that $k - \epsilon$ model cannot predict the normal stresses in certain flow situations because of imposing gradient diffusion hypothesis. As this hypothesis does not accurately capture the underlying process which are responsible for turbulence anisotropy. The advantage of using RSM is that production term is exact and do not require modelling. The drawback of RSM model is addition of 6 additional stress transport equation in 3 dimensions. Total of sixteen equations for sixteen unknowns needs to be solved for a two equation model requires more computation time.

v^2-f Turbulence Model

This model is a four equation turbulence model. In addition to k and ϵ , it has two more equations, the normal stress function and the elliptic function, in addition to k and ϵ . Capturing near wall-turbulence behavior is of utmost importance for heat transfer problems. The v^2-f turbulence model is able to better predict fluid behavior for impinging jet flows in comparison to other RANS models. Although DNS and LES can yield excellent model predictions, computational cost negatively affects the use of such models. The v^2-f model is a four-equation turbulence model developed by Parneix and Durbin [80]. The K-Epsilon model solves only two equations, k , which

is the turbulence kinetic energy, and ε , which stands for the dissipation rate. The v_2-f model solves the two original equations and also a velocity variance scale v_2 , and the elliptic relaxation function f .

Large Eddy Simulation (LES)

The continuity and Navier-Stokes equations in the tensorial form for an incompressible flow can be written as [70]:

$$\frac{\partial u_i}{\partial x_i} = 0 \quad (41)$$

$$\frac{\partial u_i}{\partial t} + \frac{\partial u_i u_j}{\partial x_j} = -\frac{1}{\rho} \frac{\partial p}{\partial x_i} + \vartheta \frac{\partial^2 u_i}{\partial x_i \partial x_j} \quad (42)$$

At large Reynolds number the small scales are nearly isotropic and exhibit similar behavior whereas the large scales are more anisotropic. The essence of LES is that a filtering operation is performed over the Navier-Stokes equations to separate out the small scales from the large scales. This filtering operation decomposes the velocity into resolved velocity and unresolved velocity,

$$u_i(x, t) = \bar{U}_i(x, t) + u'_i(x, t) \quad (43)$$

Once the filter is applied the new governing equations can be written as:

$$\frac{\partial \bar{U}_i}{\partial x_i} = 0 \quad (44)$$

$$\frac{\partial \bar{U}_i}{\partial t} + \frac{\partial \bar{U}_i \bar{U}_j}{\partial x_j} = -\frac{1}{\rho} \frac{\partial p}{\partial x_i} + \vartheta \frac{\partial^2 \bar{U}_i}{\partial x_i \partial x_j} - \frac{\partial \tau_{ij}}{\partial x_j} \quad (45)$$

The term τ_{ij} is called subgrid stress and needs to be modeled to close the equations. The subgrid stress with the resolved strain rate through an SGS eddy viscosity is given by

$$\tau_{ij} = \mu_{SGS} \bar{S}_{ij} \quad (46)$$

In the Smagorinsky SGS model the eddy viscosity can be expressed as

$$\mu_{SGS} = (C_s \Delta)^2 \sqrt{2 S_{ij} S_{ij}} \quad (47)$$

One of the drawback of SGS model is C_s is constant. Ideally C_s is not universal and depends on the flow behavior. Since the coefficient in Smagorinsky model cannot be negative it does not allow for the energy backscatter. To overcome these limitations other SGS models have been developed and used in the published literature. In a dynamic Smagorinsky model [72] the backscatter of energy is allowed and C_s is not a constant.

Where S_{ij} the strain rate. One of the drawbacks of the SGS model, is that C_s is constant. Ideally C_s is not universal and depends on the flow behavior. Since the coefficient in the Smagorinsky model cannot be negative, it does not allow for energy backscatter. To overcome these limitations other SGS models have been developed and used in the published literature. In a dynamic Smagorinsky model [72] the backscatter of energy is allowed, and C_s is not a constant. The WALE subgrid model [81] is an improved version of the Smagorinsky model. This model takes into account the effect of both the strain rate and the rotation rate of the smallest scales in turbulent flow. The subgrid scale viscosity in the Wall-Adapting Local Eddy-viscosity SGS model (WALE) model is defined as [81]:

$$\mu_t = C_w \rho \Delta^2 \frac{OP1}{OP2} \quad (48)$$

$$OP1 = (S_{ij}^d S_{ij}^d)^{1.5} \quad (49)$$

$$OP2=(S_{ij}^d S_{ij}^d)^{2.5} + (S_{ij}^d S_{ij}^d)^{1.25} \quad (50)$$

In the current study, to support experimental data, wall modeled Large Eddy Simulation (LES), and Reynolds Averaged Navier-Stokes (RANS) simulations were performed in the same channel geometry. The Wall-Adapting Local Eddy-viscosity SGS model (WALE) [81] is used for the LES calculation.

CHAPTER 4: EXPERIMENTAL SETUP

Curved surface Impingement

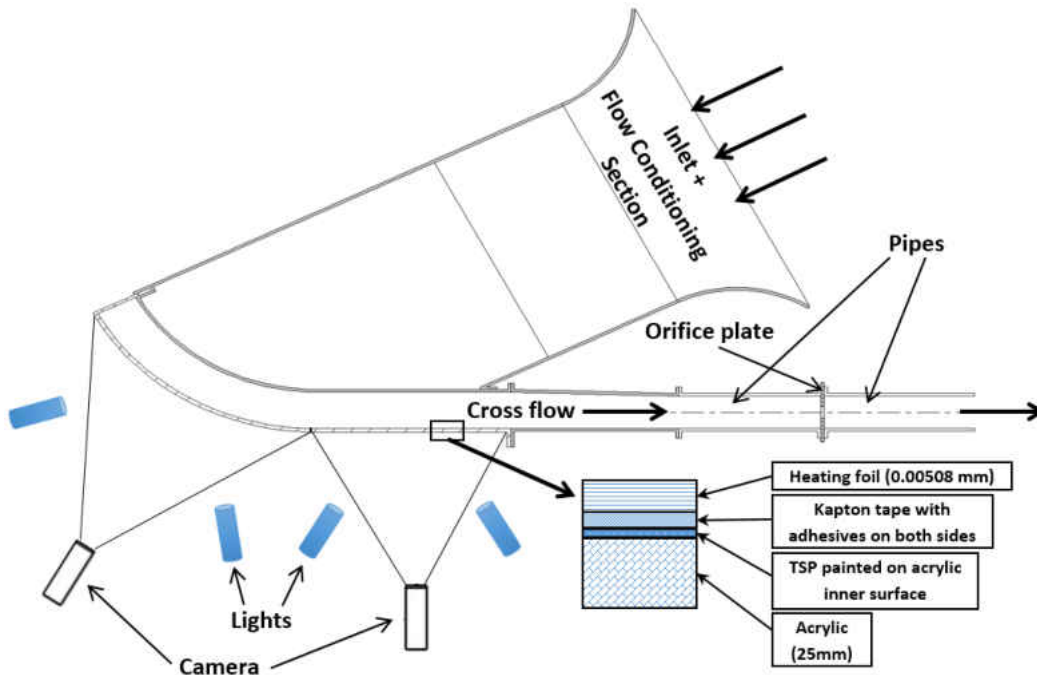


Figure 10 Test section for the curved surface impingement

As stated in [47], the experimental set up consists of an inlet plenum, an aluminum jet plate, a target wall, and two sidewalls. The inlet plenum is constructed with an aluminum honeycomb flow conditioner with two fine mesh screens on both sides. A hotwire probe was located after the flow conditioning system to measure the turbulent intensity inside the plenum. The probe was traversed across the plenum to acquire multiple data points to confirm flow uniformity. The jet plate is fabricated from an aluminum plate using a water jet cutter, producing sharp edged holes. The jet plate consists of 28mm holes with an $L/D=0.1$. The sidewalls are fabricated from acrylic with a constant height of $3D$. One of the sidewalls consists of pressure taps located between each jet

centerline, maintaining a constant S/D along the length of the target plate. The flow is guided to the jet plate via the plenum and impinges the target surface. Once the flow impinges the target surface it travels downstream through a constant cross-sectional area duct. At the end of the channel the duct transitions from a rectangular cross-section to a circular pipe, operating as a diffuser. The flow then passes through an orifice plate, measuring the flow that exits the impingement channel. The orifice plate is manufactured and setup following ASME PTC 19.5 [82]. The flow is entirely under suction, being pulled by a 250hp electric blower. A gate valve, located directly before the blower, controls the mass flow rate through the channel. Figure 10 shows the schematic of the test section. The test section, where the heat transfer is measured, is located on the target surface consisting of a constant area covering the two center jets and the respected downstream area. The heated area is comprised of temperature sensitive paint (TSP), a Kapton adhesive, and a foil heater. The foil heaters are made of type 321 stainless steel with a thickness of $t=5.08 \times 10^{-3}$ m and have an average electrical resistivity of $\rho_{el}=720 \times 10^{-7}$ Ω -m. Since resistivity is a function of temperature, the variation in local resistance was calculated at each data point. The maximum variation of resistivity was found to be $\sim 4\%$. The foil heaters are attached to the TSP using double-sided adhesive Kapton tape of thickness $t=2.54 \times 10^{-5}$ m. The foil is heated using a 120volt, 20amp VARIAC. During the experiment two sets of images are taken, a set reference (cold) images and a set of steady-state (hot) images. The excitation wavelength for the TSP is 460 nm wavelength, which excites the luminescent molecule. A set of 8 reference images are taken at the start of the experiment before any heat flux is applied to the target surface; these images are used as the reference temperature during post processing. After steady state is reached, $dT/dt=0$, another set of 8 images are taken. Images of the TSP surface are acquired using a PCO-

1600 thermo-electrically cooled CCD camera with a resolution of 1600 by 1200. The cameras are located perpendicular to the center of the curved and flat sections, independently. The viewing angles are more than 30° to ensure the TSP measurement will not be affected [83]. Prior to experimentation, calibration of TSP is performed on a separate test section in a dark room. A small copper coupon is painted with TSP and embedded with a US Sensor 50,000 Ohm thermistor with a resolution of ±0.05°C. A total of 8 image sets are taken over a range of 25°C to 85°C. These intensities are then normalized by taking the ratio of heated intensity to the reference intensity, forming a calibration curve based on Intensity Ratio vs Temperature. All of the acquired images are processed using Matlab's image-processing software using a code developed in-house that contains the TSP calibration. More information on TSP and the calibration process can be found in Liu [84].

A cross sectional view in the streamwise direction, of the curved channel can be seen in Figure 11. For each experiment case, the spanwise and streamwise spacing of jets was kept constant. All of the testing parameters are given in Table 5:

Table 5 Test matrix

Jet Plate	r/D	S/D	Y/D	Z/D	Re _j x 10 ³
Curved	31.57	5.79	4.49	3	55, 75, 100, 125

Resistance heating the stainless steel foil produced the heat flux generated on the target surface.

Equations 41 and 42 were used to calculate the amount of heat produced.

$$q''_{gen} = \frac{i^2 R}{A_s} \quad (51)$$

$$R = \frac{\rho_e l}{wt} \quad (52)$$

Based on the knowledge that acrylic is not a perfect insulator, a heat leakage test was performed on the experimental setup to quantify the amount of heat loss due to conduction (through the backside) and radiation. To calculate the amount of heat loss through the backside by conduction, the entire impingement channel was filled with fiberglass insulation along with thermocouples on the heaters surface, backside of the acrylic plate, and ambient. Performing tests at multiple heat inputs, the change in temperature across each surface was acquired to obtain a curve for heat loss versus temperature difference, described by equation 43. Using a similar method, a test for heat loss due to radiation was performed. The insulation was removed from the channel and the inlet and outlet were blocked to limit the amount of natural convection that occurs within the channel. Equation 44 describes radiation loss as a function of temperature difference. A finite difference approach was used to estimate the lateral conduction through the acrylic target plate. The variation in Nusselt number due to lateral conduction loss was less than 1%, hence this effect was neglected in all the calculations.

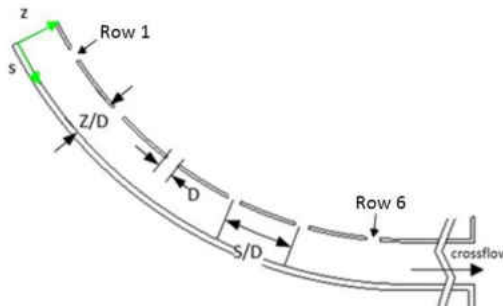


Figure 11 Detailed side view of the curved configuration

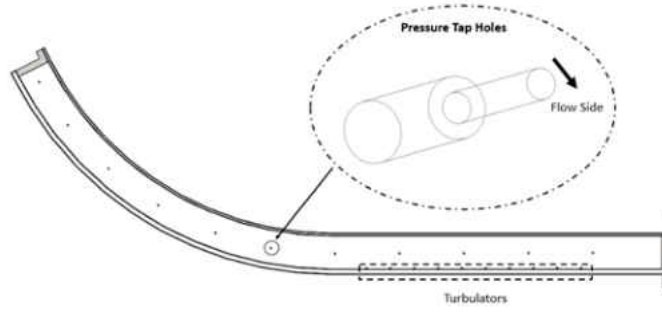


Figure 12 Pressure tap location

$$q''_{cond} = 4.61[T_w(x, y) - T_\infty] \quad (53)$$

$$q''_{rad} = 0.87\sigma[T_w^4(x, y) - T_\infty^4] \quad (54)$$

$$q''_{eff} = q''_{gen} - q''_{cond} - q''_{rad} \quad (55)$$

$$h = \frac{q''_{eff}(x, y)}{T_w(x, y) - T_\infty} \quad (56)$$

$$Nu = \frac{hD}{k_f} \quad (57)$$

The pressure data was obtained from one of the sidewalls that is fitted with pressure taps midway between the target plate and jet plate. The pressure taps are located between each jet center in the streamwise direction and continue down the impingement channel maintaining constant spacing. Figure 12 shows the detailed pressure tap mapping on the sidewall.

The pressure data gathered from these pressure taps are used to calculate the flow distribution inside the channel. Local channel mass flux to local jet mass flux ratio is calculated using equation 8 and compared to the analytical solution provided by Florschuetz et al. [13] in equation 49.

$$\frac{G_c}{G_j} \Big|_n = \frac{\frac{\pi/4}{(\frac{Y}{D})(\frac{Z}{D})} \sum_{i=0}^{n-1} \rho_i U_i}{\rho_n U_n} \quad (58)$$

$$\frac{G_c}{G_j} = \frac{1}{\sqrt{2}C_D} \frac{\sinh[\beta(\frac{x}{X} - \frac{1}{2})]}{\cosh(\frac{\beta x}{X})} \quad (59)$$

Array Impingement

As stated in [85], the channel consists of a target plate which is painted in the center region with temperature sensitive paint (TSP). Side walls with a height of three diameters separate the target and jet plate. The jet plate contains four spanwise rows of twenty streamwise holes each. The jet length is one diameter, $L/D=1$, as seen in the literature [13]. All test pieces were machined out of 19mm thick acrylic. The flow enters through the jet plate from the open atmosphere, impinges on the target plate and moves downstream. At the channel exit, the flow enters a diffuser which transitions the rectangular cross section of the channel into a three inch wide circle where the rest of the flow loop connects to. The flow loop, shown in Figure 13, consists of the test section where the flow is drawn from the atmosphere, it moves downstream through a gate valve, the flow then moves through a venturi to measure the flow rate, it passes through a flow metering gate valve, joins with the bleed flow, passes through the blower where it is then discharged into the atmosphere. Foil heaters are made out of $t=5.08 \cdot 10^{-5}$ m thick stainless steel type 321. The stainless steel has an electrical resistivity of $\rho_{el}=720 \cdot 10^{-7} \Omega m$. The resistivity is calculated at the mean

temperature of the entire heater array; resistivity variations due to uneven temperature profiles are less than 4%. The heaters are attached to the painted surface with the use of 2.54×10^{-5} m thick double-sided Kapton tape. The heaters are powered using a 120 volt, 20 amp variable alternating current (AC) power supply. A total of four 19mm wide heaters are placed on the target plate. The heater strips were connected in series with the use of 12.7 mm wide copper bus bars housed in slots located on both sides of the target plate. Pictures of the TSP are taken with a PCO1600 thermoelectrically cooled CCD camera with a resolution of 1600 by 1200; typical spatial resolution obtained is of 20 pixels per diameter. Reference pictures are taken at the start of each test alongside the reference temperature of the TSP. Once the test has reached steady state ($\partial T / \partial t \approx 0$), a set of test, or hot, images are taken. TSP calibration is performed on a different test section located in a black room. An acrylic piece is painted and attached to a copper block which contains a US Sensor 50000 Ohm thermistor with a resolution of $\pm 0.05^\circ\text{C}$; the block is attached to a thermoelectric heater that heats the block to multiple calibration temperatures. A total of 15 image sets are taken at temperatures ranging from 25°C to 85°C alongside a set of reference temperature and images. The images are processed by taking average intensities, normalizing them by the average intensity of the reference image. A TSP calibration curve is now generated which provides temperature as a function of image intensity ratio. The test images are processed using an in-house code which contains the TSP calibration. A more complete explanation of the TSP calibration and post processing is provided by Liu [84].

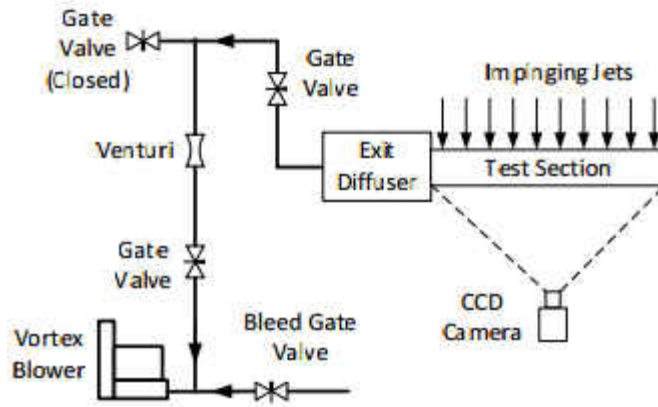


Figure 13 Flow loop setup [85]

The schematics for the test piece is shown in Figure 14. The heated area is shown by red line. This heat area is designed such that it represents a periodicity of the entire channel.



Figure 14 Heated area for the impingement channel

The geometric spacing for the study is shown in table 6.

Table 6 Test matrix

x/D	y/D	z/D	Re _j
3	8	3	10K-30K

Narrow Wall Impingement

As stated in [25], the test section and coordinate system for the narrow wall impingement channel can be seen in Figure 16. The streamwise and spanwise spacing is kept constant throughout the channel. The channel consists of an orifice plate containing jets with diameter of 7.5 mm (0.0075m), a target wall and two side walls. One of the side walls is instrumented with pressure taps. The taps were located in the middle between every two jets in the streamwise direction at half of the channel height. One end of the channel is capped while the other is left open. The jet length to diameter ratio, L/D , was 1, as seen in literature [14]. All test pieces are machined out of 19 mm thick acrylic sheets. A plenum was used to guide ambient air through the jet plate. After the flow impinges on the target wall, it moves downstream where it exits the channel into a dump diffuser. A 76.2 mm (3 in) pipe guides the flow from the diffuser to a gate valve used to control the flow which then passes through a calibrated venturi flow meter. A complete diagram of the flow loop is shown in Figure 16

The target plate was painted with temperature sensitive paint (TSP) for heat transfer measurement. Foil heaters are made out of $t_h=5.08*10^{-2}$ mm thick stainless steel (type 321). The stainless steel has an electrical resistivity of $\rho_{el}=720*10^{-4}$ Ω -mm. The resistivity is calculated at the mean

temperature of the entire heater array. The heaters are attached to the painted surface with the use of 2.54×10^{-2} mm thick double-sided Kapton tape. The heaters are powered using a 120 volt, 20 amp variable alternating current (AC) power supply. Pictures of the TSP are taken with a PCO1600 thermoelectrically cooled CCD camera with a resolution of 1600 by 1200; typical spatial resolution obtained is of 20 pixels per diameter. Reference pictures are taken at the start of each test alongside the reference temperature of the TSP. Once the test has reached steady state ($\partial T/\partial t \approx 0$), a set of test, or hot, images are taken. Then the temperature of the hot images can be acquired as a function of image intensity ratio by using a calibrated TSP temperature-intensity ratio curve. TSP calibration is performed on a different test section located in a black room. An acrylic piece is painted and attached to a copper block which contains a US Sensor 50000 Ohm thermistor with a resolution of $\pm 0.05^\circ\text{C}$; the block is attached to a thermoelectric heater that heats the block to multiple calibration temperatures. A total of 15 image sets are taken at temperatures ranging from 25oC to 85oC alongside a set of reference temperature and images. The images are processed by taking average intensities and normalizing them by the average intensity of the reference image. The test images are processed using an in-house code which contains the TSP calibration. A more complete explanation of the TSP calibration and post processing is provided by Liu [84]

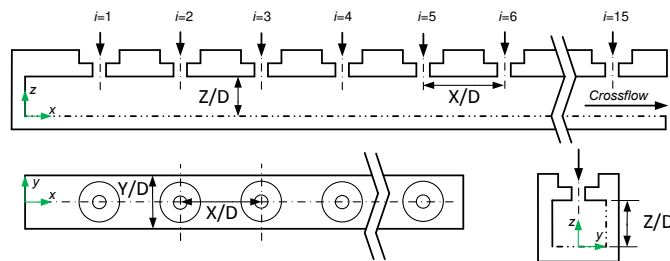


Figure 15 Test section schematic of the narrow wall impingement channel [25]

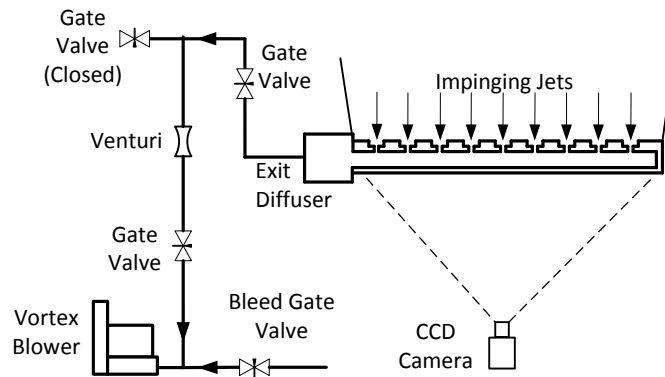


Figure 16 Flow loop test setup for impingement heat transfer [25]

Particle Image Velocimetry (PIV) was conducted in order to obtain a quantitative measurement of the flow field of interest. Flow was illuminated by a pulsed Quantel® Evergreen 200mJ Nd:YAG laser triggered at a specified time interval (15 μ s). The beam is focused using a single spherical lens, and the laser sheet is created as the beam passes through a cylindrical lens. The field of view for the measurement covers a sufficient area, as to image the entire narrow channel extent past the 5th jet. The spanwise location of the PIV measurement plane was on the channel centerline, on jet.

Flow was seeded using a Laskin type TSI® oil droplet generator. Seed particles were fed at the inlet of the impingement jet array above the feed plenum as seen in Figure 17 and Figure 18. Because flow particles were introduced upstream of the impingement jets, uniform seeding of each jet was possible. Mean particle size was approximately 1 μ m, with a typical particle image density of \sim 10 particles per interrogation region. The PIV test case shown here consists of 1800 ensemble averaged instantaneous image pairs in order to adequately estimate the mean statistics of interest. Statistical convergence for mean quantities is achieved with \sim 100 image pairs. Images were acquired at a rate of 15hz and processed using LaVision's DaVis 8 software. An Andor Zyla

5.5 megapixel (2560 x 2160 pixels) CMOS camera equipped with a 55mm focal length lens, was used for image acquisition. A more robust cross-correlation can be achieved by increasing particle image contrast; this was realized by pre-processing all images with the sliding background method within Davis 8. Velocity correlations were then made using a multipass algorithm with an initial window size of 48 x 48 pixels with 8 passes of a Gaussian shaped interrogation window size of 24 x 24 with a 75% window overlap. Spurious vectors are minimized by using the universal outlier detection scheme implemented within DaVis 8; this is an extra post-processing step after vector calculation. Resulting spatial resolution of the velocity field is approximately 0.53 mm x 0.53 mm. No post-processing filters or vector interpolation techniques were used.

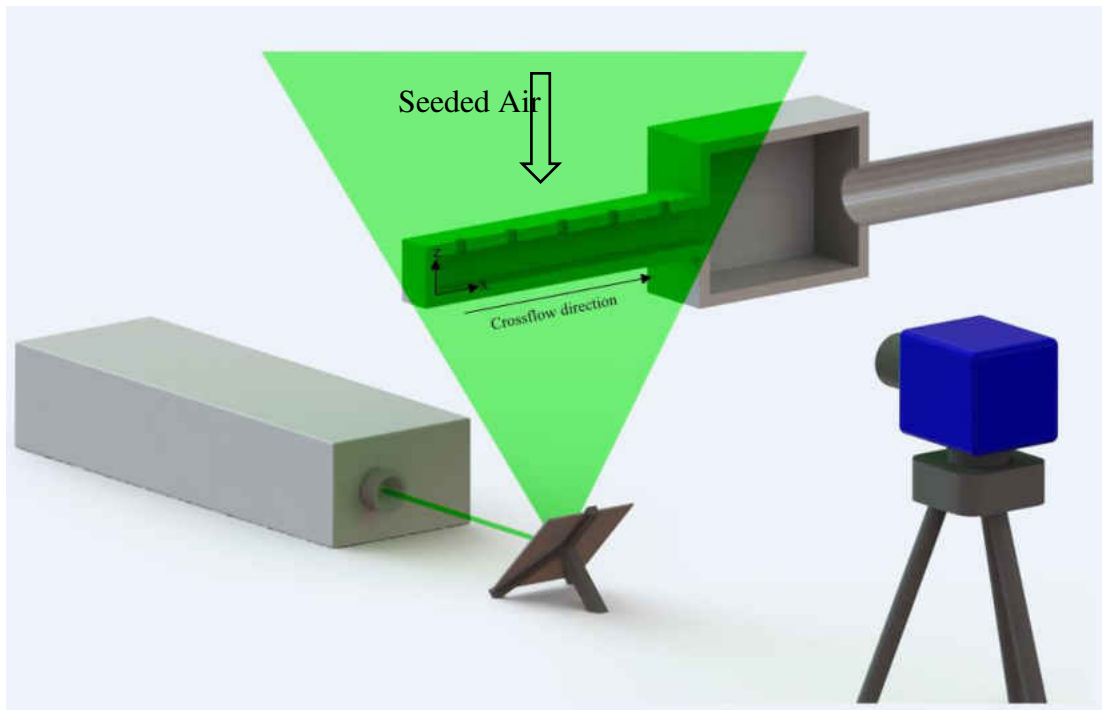


Figure 17 PIV setup

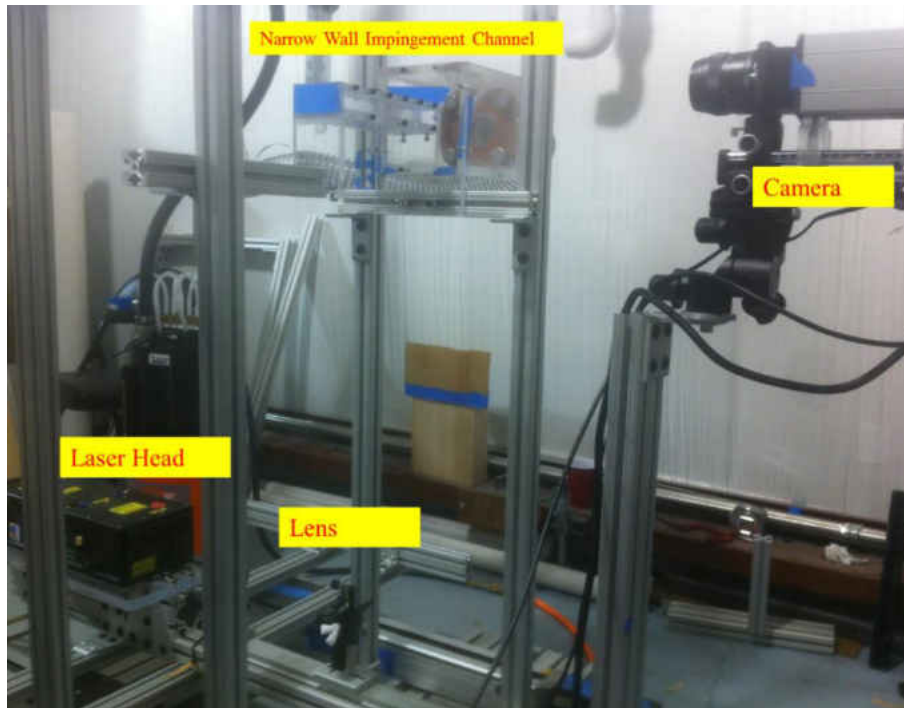


Figure 18 Experimental set up

CHAPTER 5: NUMERICAL SETUP

Curve Surface Impingement

Boundary Condition

As stated in [47], all boundary conditions are selected to be as closed as possible to the experimental conditions. In order to implement some conditions simplifications had to be made due to the physics of the problem. The Inlet boundary condition was simplified by shortening the plenum to reduce cell count and computation time. The inlet turbulent intensity and length scale was measured using a hotwire probe. Results obtained from the hotwire were used in CFD for inlet boundary condition. The stagnation inlet boundary condition was applied to the inlet of the plenum, where ambient pressure and temperature were specified. The plenum walls, sidewalls, jet plate and outlet pipe were all considered no slip, adiabatic walls. Turbulators are also considered to be adiabatic, no slip condition. The impingement-curved surface is considered, as the target wall is also no slip wall. A uniform heat flux boundary condition was applied to the target wall. The boundary conditions are shown in Figure 19.

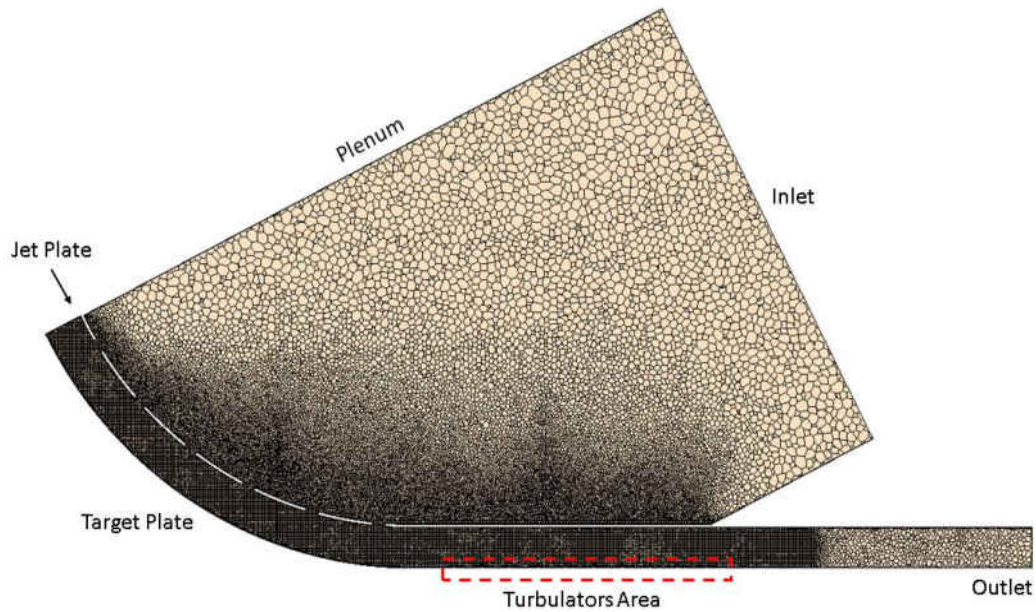


Figure 19 Computational domain

Mesh

A polyhedral mesh and combination of control volumes was chosen to model the problem at hand. Polyhedral mesh was chosen due to smooth growth behavior away from the wall, location of the jet holes, and turbulators. Carefully using volumetric control around turbulators and impingement plate a uniform mesh was created which can be seen in Figure 19. Density and growth cell rate were adjusted in order to decrease the global cell count. Blending cell factors were also adjusted in order to smooth the transition between control volumes and regular polyhedral mesh growth. Proper resolution of the boundary layer is critical; to achieve desired accuracy and proper physical behavior. The entire boundary layer must be contained within a proper prim layer thickness. To achieve a near-wall y^+ value close to the order of one, 20 prism layers were specified at the target

wall and also the all y^+ wall function was used. For all the turbulators, W-shaped and 90° , a similar mesh scheme was used. Figure 20, Figure 21, Figure 22 show the mesh for all the turbulators.



Figure 20 Mesh of the 90° turbulators



Figure 21 Mesh of the W-1-shaped turbulators



Figure 22 Mesh of the W-2 shaped turbulators

Grid Convergence

A mesh sensitivity analysis was carried out in order to obtain a mesh independent solution. Harrington et al. [60] performed a time averaged URANS and iteration averaged RANS simulation and reported that they produced the same result. Based on this previous work the last 1000 iterations for heat transfer coefficient are averaged and used to calculate Nusselt Number. The overall base size of the mesh is modified by +/- 12.5%, thus obtaining a finer and coarser grid, can be seen in Figure 23. The sensitivity showed a change in Nusselt Number of less than one percent from 16 Million cells to 23 Million cells. However the deciding factor for choosing the higher density mesh was due to the range of the y^+ values at the target wall. The finer mesh yielded a $y^+ < 1$, which is ideal for heat transfer and v^2-f turbulence modeling.

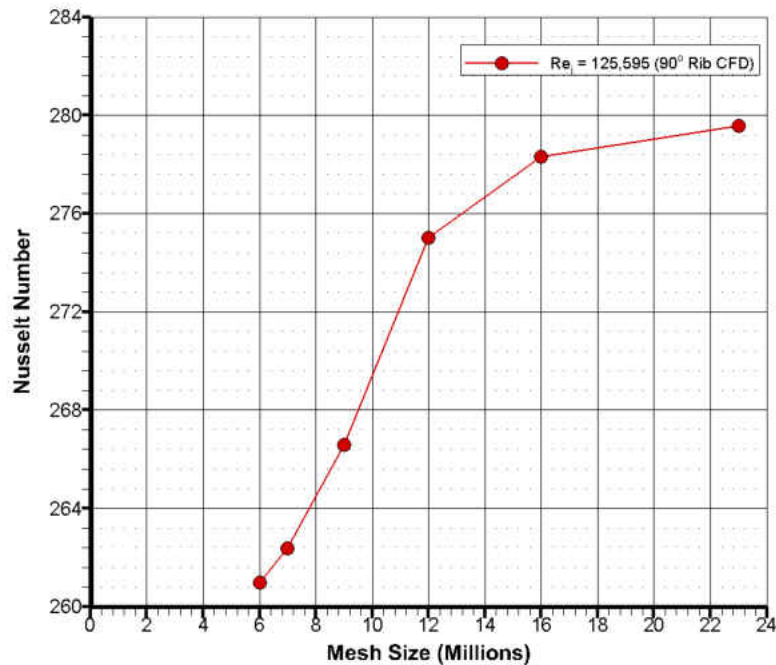


Figure 23 Grid convergence study

Array Impingement

A wide array impingement configuration experimentally and numerically studied in the current study. The jet plate for the impingement consists of a constant streamwise spacing of $x/D=3$ and constant spanwise spacing of $y/D=8$. The jet-to-target plate distance was $3D$ in the current study. Figure 24 shows the impingement configuration studied for the current study.

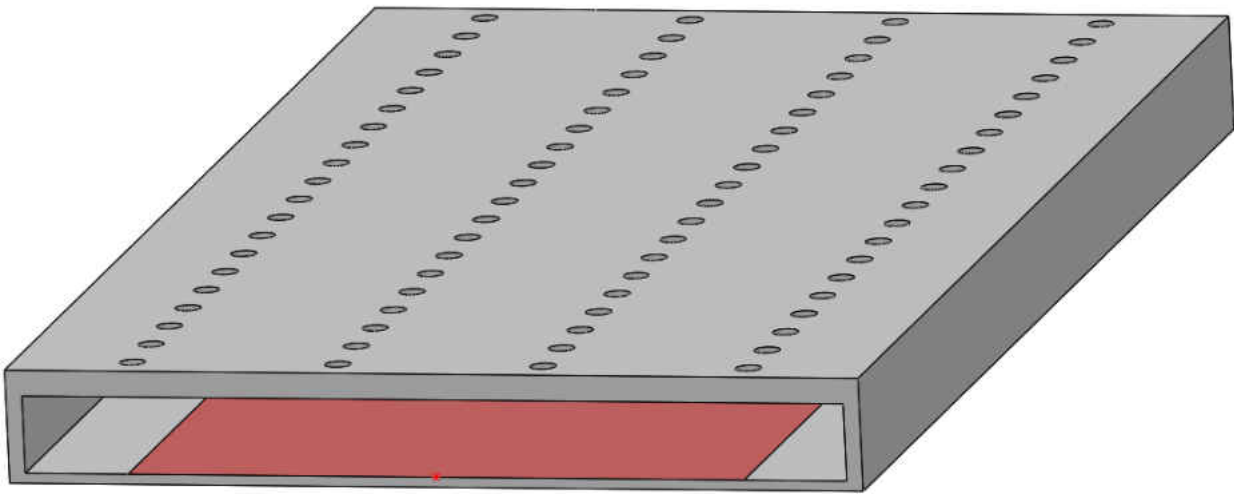


Figure 24 Wide array impingement configuration

Boundary Condition

Figure 25 shows the computational setup for the wide array impingement study. A stagnation inlet boundary condition was applied to the top face located 3 jet diameters from the face where jets originate. This boundary condition is considered as plenum inlet. A constant heat flux boundary condition was applied to the target wall. The experimental setup for the wide array impingement configuration contains four lateral rows of jet. In order to reduce the computational domain and

computational time half of the entire domain was simulated using a symmetry boundary condition as shown in Figure 25. A pressure outlet boundary condition was applied at the outlet.

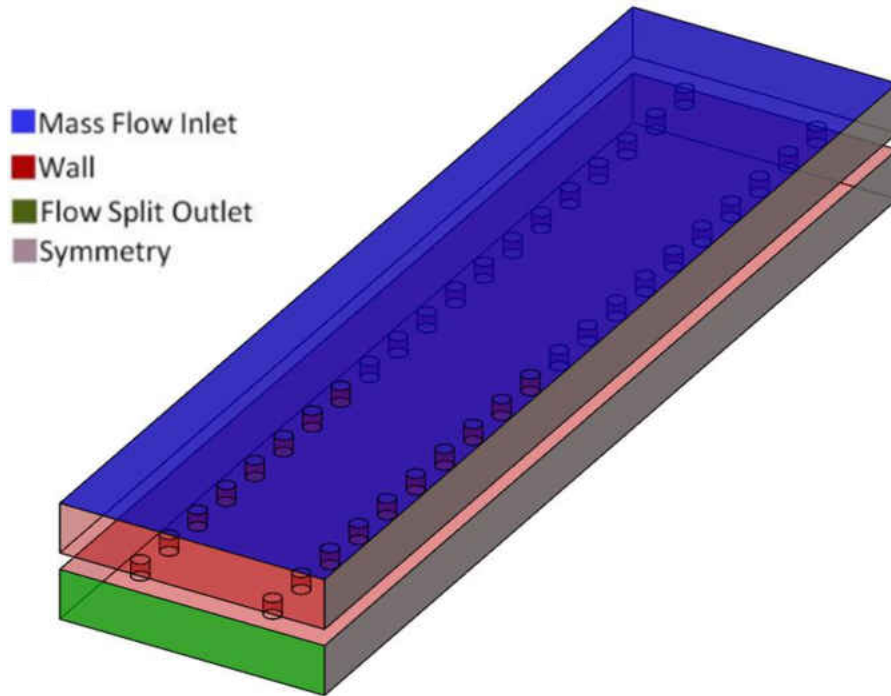


Figure 25 Computational Setup and boundary conditions

Mesh

A mesh was generated using unstructured grids with hexahedral elements using ANSYS ICEMCFD, version 15.0. Figure 26-30 show the mesh structure used for numerical calculations. Cell orthogonality was ensured by applying O-grid type blocks for all the jets. Very fine grids were used near the jet shear layer, jet cores and near the target wall region. Since the two jets are very close to each other special care was taken to refine the mesh in between jets.

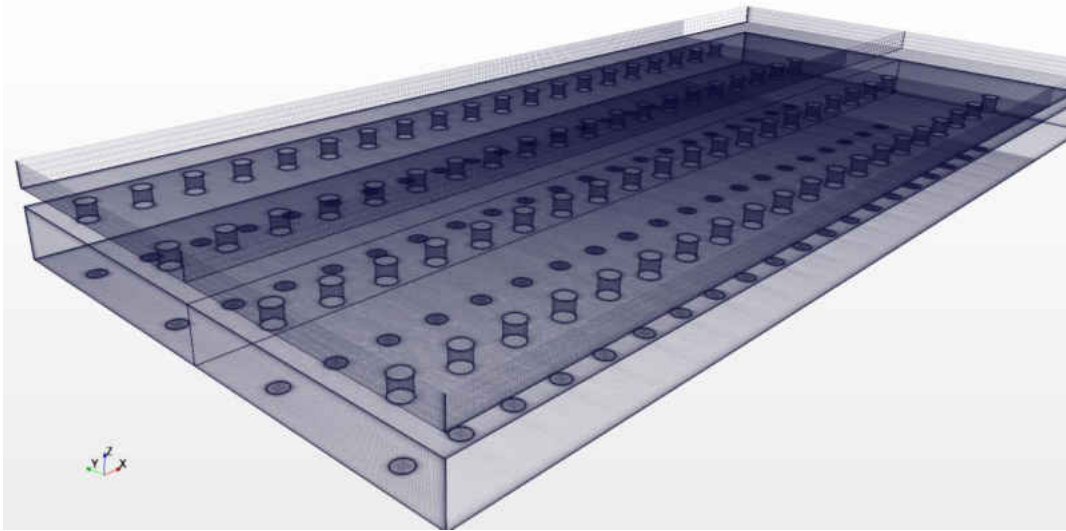


Figure 26 Detailed Mesh

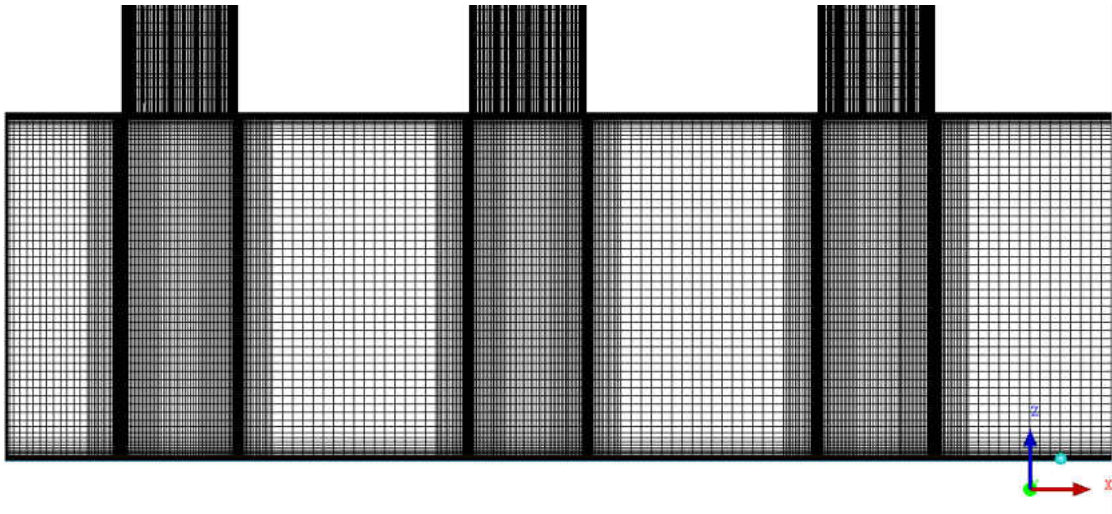


Figure 27 Shear layer refinement

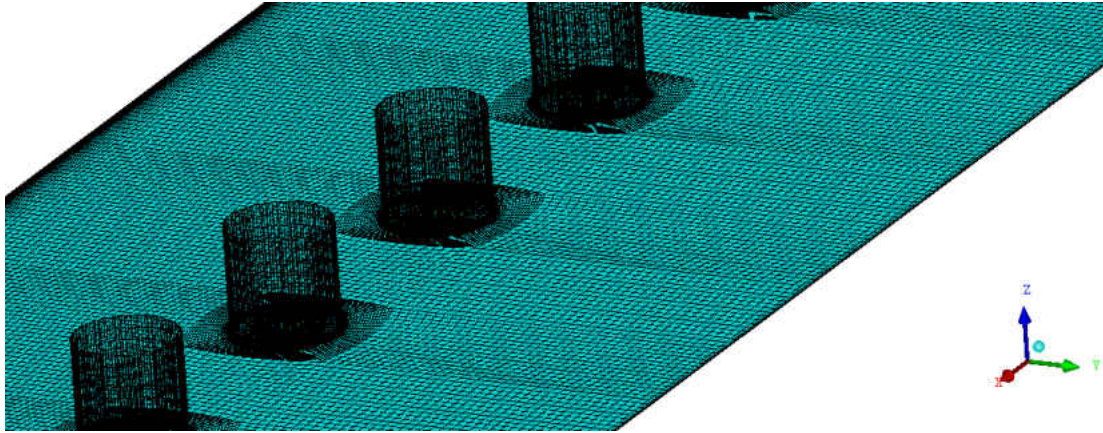


Figure 28 Mesh near the jet

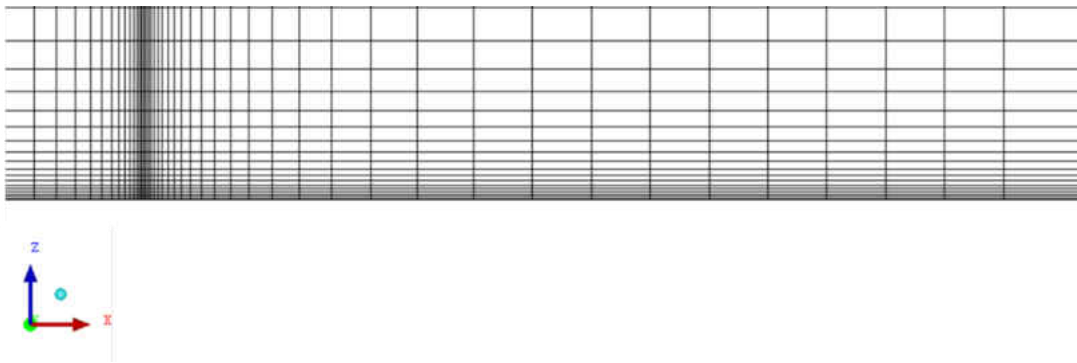


Figure 29 Near wall refinement

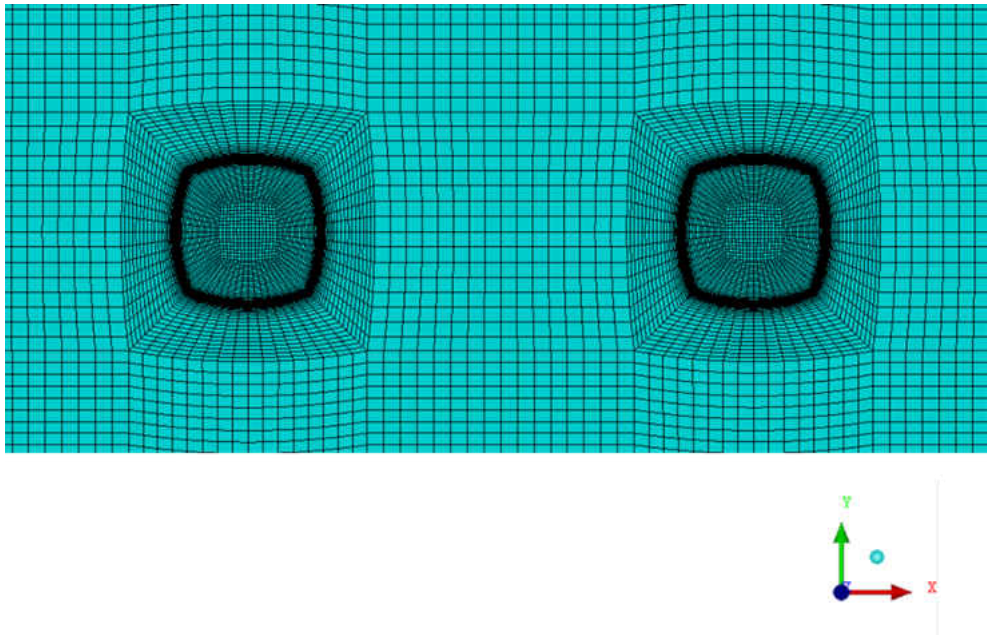


Figure 30 Mesh with O-grid block structure

Grid Convergence

A mesh sensitivity study was done in order to obtain a grid independent solution. v^2-f turbulence model was used for the numerical calculation. The assumptions used to model the numerical problem are steady state, ideal gas, and three dimensional turbulent model. A segregated flow solver was used using a 2nd-order upwind scheme. A segregated fluid temperature model was also employed using a 2nd-order upwind scheme. The residuals for continuity, momentum, velocity and pressure probes in the jet shear layer were closely monitored to ensure convergence. Once the solution has reached steady state the last 5000 iterations for the flow field and heat transfer coefficient were averaged for final results.

Figure 31 shows the grid independent study used for the array impingement configuration. The grids were refined gradually from 10 million cells to 23 million cells. For each cases target wall

averaged Nusselt number was used to monitor grid independent solution. The finest mesh (23 million cells case) was used for the study.

The $y^+ < 1$ was ensured for all the cases. Figure 32 shows the target wall y^+ at the target wall for the current study.

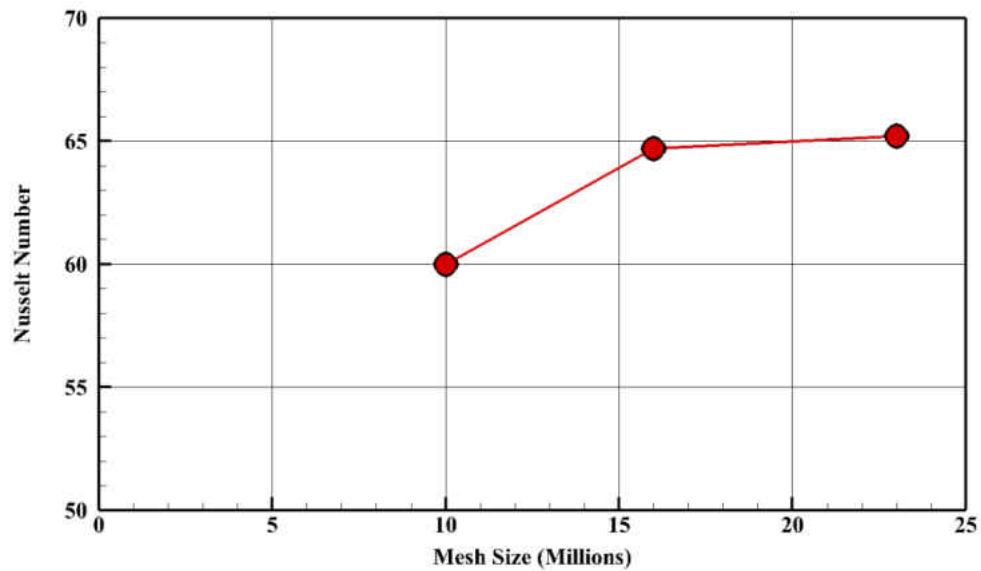


Figure 31 Grid independence study

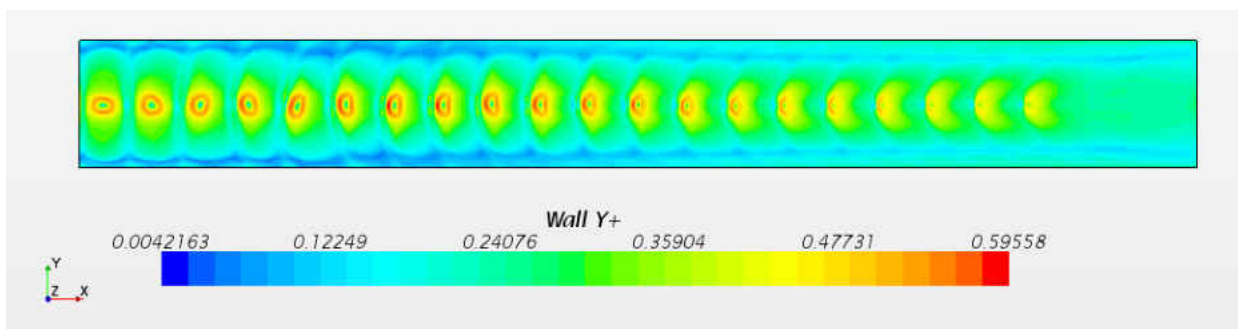


Figure 32 Target wall y^+ distribution for the finest mesh

Narrow Wall Impingement

Mesh

As stated in [86], for LES calculations, a mesh was generated using unstructured grids with hexahedral elements using ANSYS ICEMCFD, version 15.0. Figure 34 and Figure 34 shows the mesh structure between two jets. Similar meshes exist throughout the computational domain. Cell orthogonality was ensured by applying O-grid type blocks for all. Maximum local z_1^+ values were < 1.0 at the target wall for all the cases. Very fine grids were used near the jet shear layer, jet cores and near the target wall region. Same mesh was used for RANS calculation.

Piomelli and Chasnov [71] have described meshing criteria for wall bounded LES calculations.

These are:

Table 7 Mesh criteria by [71]

Δx^+	$<100-600$
Δy^+	$<100-300$
Δz^+	$<25-30$

In the current study the grid spacing were chosen such that it follows the criteria shown in Table

7

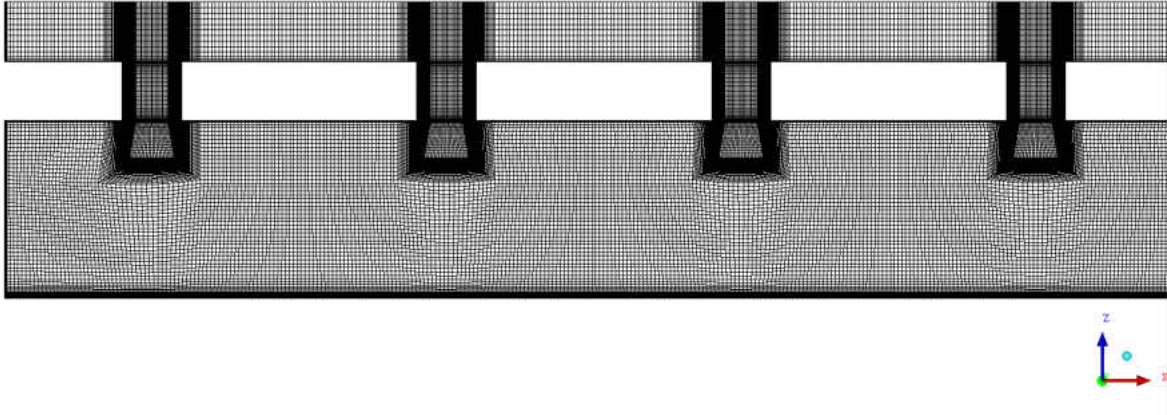


Figure 33 Mesh at the centerline plane of the channel

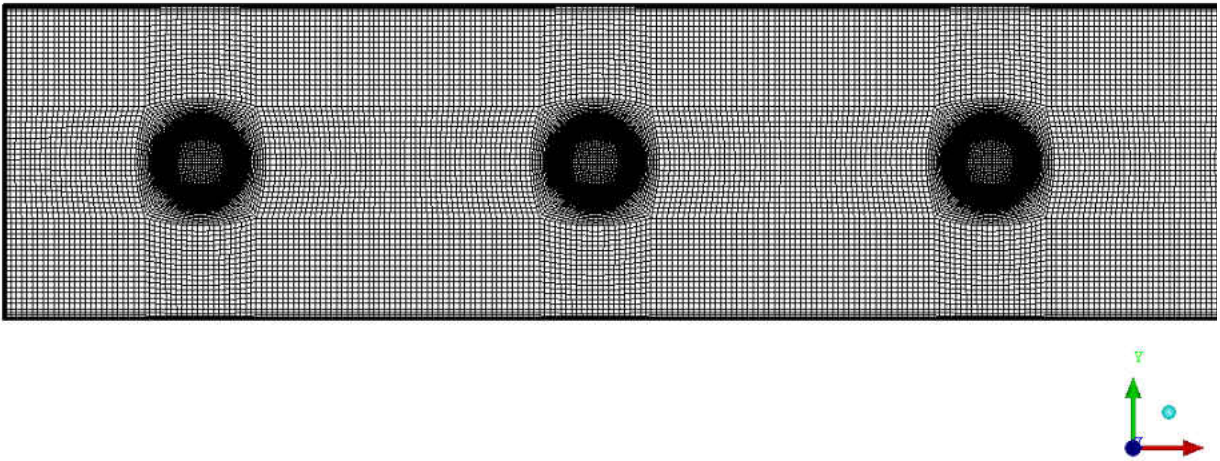


Figure 34 Mesh from the top

Table 8 Mesh criteria for the present study

Dimensionless grid spacing	Piomelli and Chasnov [71]	Present Study
Δx^+	<100-600	50
Δy^+	<100-300	60
z^+	<25-30	<1

Boundary Condition

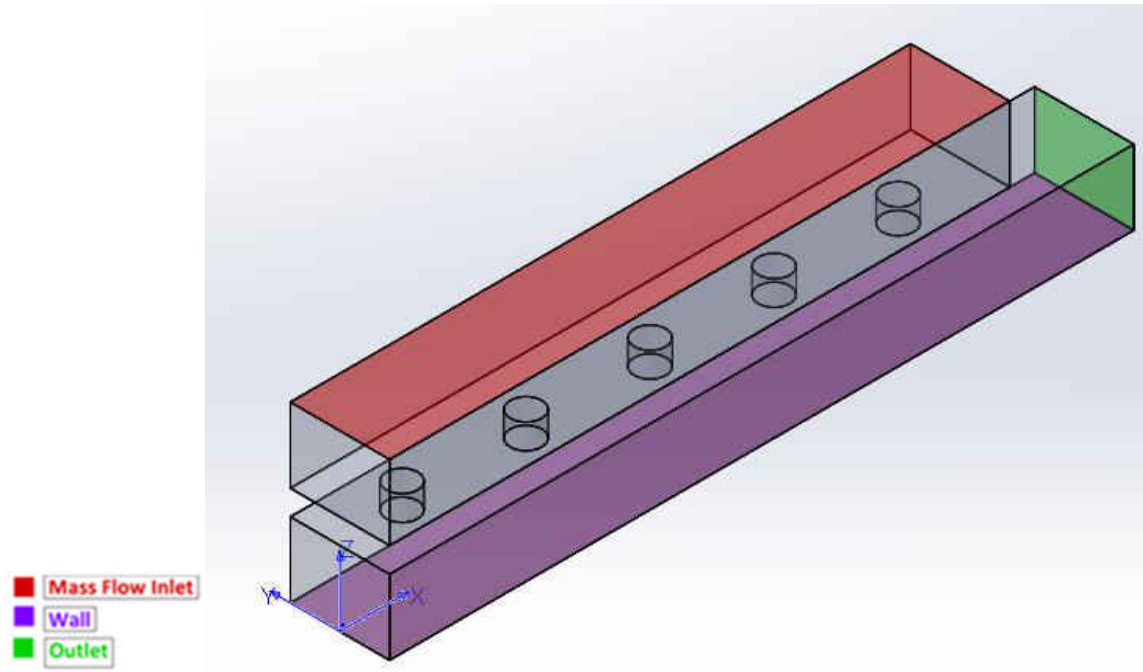


Figure 35 Computational setup for the five jet impingement study

Figure 35 shows a detailed description of the geometry and boundary conditions used for numerical calculations. A mass flow inlet boundary condition was applied to the top face located 1 jet diameters from the face where the jets originate. At the outlet pressure outlet boundary condition was applied. All the calculations were performed using a commercial CFD solver: StarCCM+. A second order discretization method was used in the simulations and a segregated flow solver was used for all the calculations. The LES simulation was run for 8 flow through times to reach statistical convergence.

Grid Convergence

Figure 36 shows the statistical convergence of mean and second order statistics of the flow variable. Details of the grid convergence are given in the appendix section.

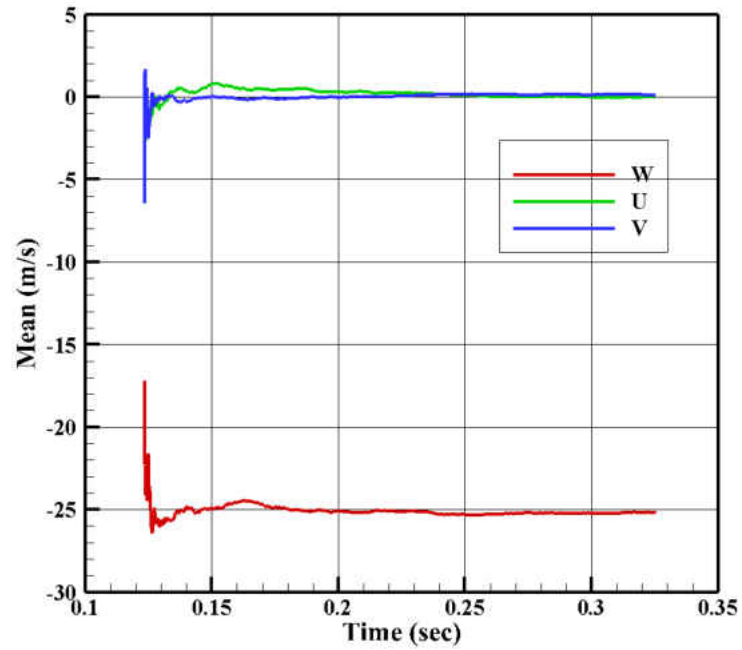


Figure 36 Grid Convergence

CHAPTER 6: RESULTS

Curve Surface Impingement

Flow Distribution

As stated in [47], the pressure loss of a system is represented by discharge coefficient. In this study, an array averaged jet discharge coefficient was calculated for all the test configurations. Jet discharge coefficient can be defined as

$$C_d = \frac{\dot{m}_{actual}}{\dot{m}_{ideal}} \quad (60)$$

The total actual mass flow rate was measured from the orifice plate located at the downstream of the test rig. Pressure measurements were taken on one of the sidewalls using pressure taps connected with a Scanivalve pressure transducer. The ideal flow rate was calculated from the sidewall pressure data (p_i) using one-dimensional isentropic flow relation through the jet holes.

$$\dot{m}_{ideal} = \rho_i U_i A_i \quad (61)$$

$$U_i = a \sqrt{\left[\left(\frac{p_0}{p_i} \right)^{\frac{\gamma-1}{\gamma}} - 1 \right] \frac{2}{\gamma-1}}, \quad a = \sqrt{\gamma R_{air} T_0} \quad (62)$$

Where p_0 is the total pressure inside the plenum and T_0 is the plenum air temperature. Figure 37 shows an array averaged discharge coefficient for all the jet Reynolds numbers. The discharge coefficient remains constant for all the Reynolds number tested. The discharge coefficients calculated from the experiments were used for flow distribution in the channel for each configuration shown in Figure 37

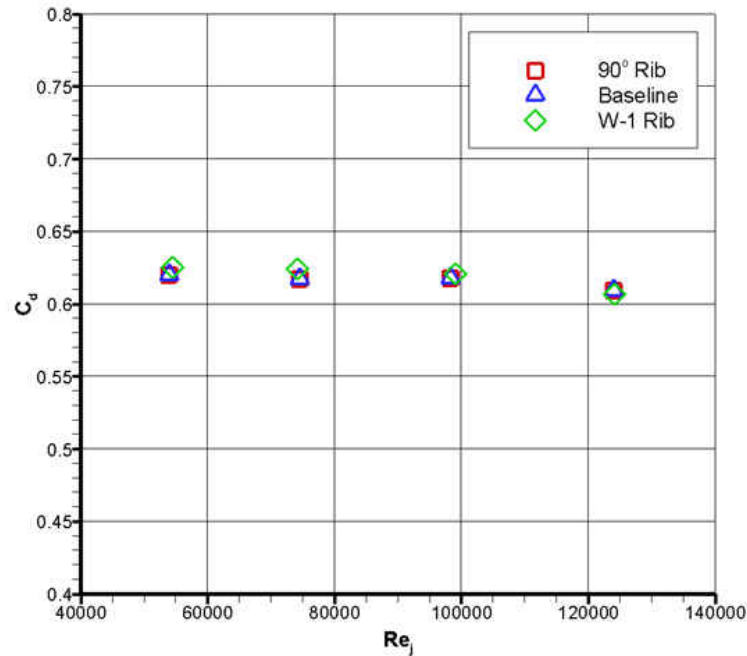


Figure 37 Array-averaged discharge coefficients

The flow distribution measurement technique was validated by comparing the model proposed by Florschuetz and Isoda [13]. The pressure data collected from the sidewall, and using equation 8 and 9, were used to calculate streamwise flow distribution inside the channel. Since the current geometric configuration ($S/D=5.79$, $Y/D=4.49$, $Z/D=3$) falls within the range of domain tested by Florschuetz and Isoda [13] the streamwise flow distribution was compared with the 1-D analytical model given by Florschuetz et al. Figure 38 shows the local crossflow distribution tested at average jet Reynolds number of 55,000. For the other Reynolds number, the distribution showed similar behavior and matched well with the Florschuetz correlation suggesting that the local crossflow to jet mass flux ratio is independent of jet Reynolds number. It is apparent from Figure 38 that the

curvature and the presence of different shaped turbulators located at the downstream do not have a much impact on altering the crossflow and pressure distribution inside the channel.

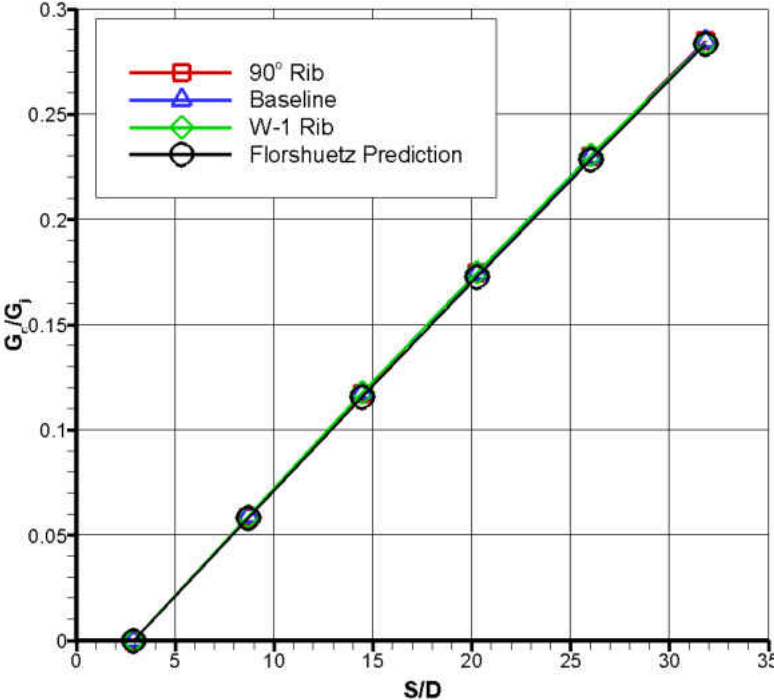


Figure 38 Experimental local G_c/G_j distribution for $Re_j = 55,000$

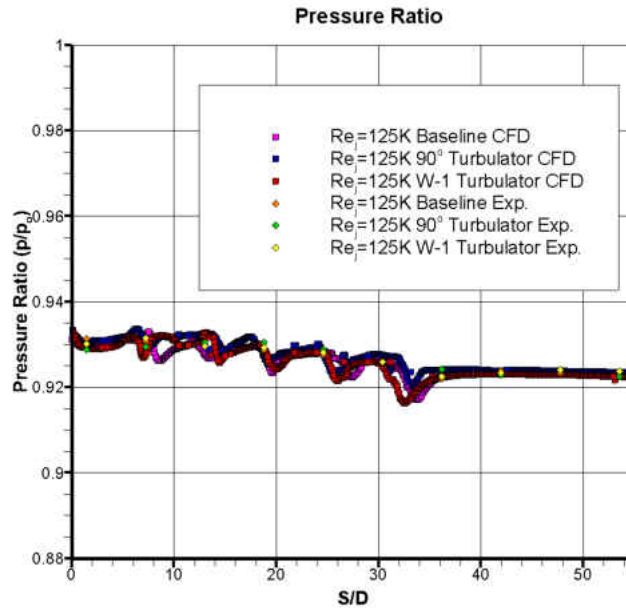


Figure 39 Pressure ratio distribution

Figure 39 shows the pressure ratio (p/p_0) distribution for the baseline, 90° turbulators, and W-shaped turbulators cases under the jet Reynolds number of 125K. The pressure data measured from the sidewall of the test section are normalized with respect to plenum pressure. For all the configurations, pressure distributions show fairly uniform behavior at the downstream section of the channel. CFD analysis was carried out to validate experimental data. Both CFD and experimental results show good agreement of pressure distribution. In the presence of turbulators, the pressure ratio exhibits very similar behavior to the baseline configuration. Since the channel blockage ratio (ratio of rib height to channel height, e/Z) is $\sim 4.76\%$ for the current rib configuration, not a significant pressure drop occurred inside the channel. For the other Reynolds number cases similar behavior was observed.

Experimental Heat Transfer Result

El-Gabry and Kaminski [57] described the importance of obtaining local heat transfer distribution for impingement cooling. First, designs that are based on averaged heat transfer are more likely to fail in practical operation due to extreme temperature gradients and thermal stresses. A local heat transfer distribution provides the designer an insight of the thermal behavior. Second, results obtained from local temperature distribution can be used to validate CFD results so that CFD can be used as a reliable design tool in the industry. The baseline configuration was tested at four different jet Reynolds numbers. The heat transfer was measured from $Y/D = -4.46$ to $+4.46$, where $Y/D=0$ represents the center of the target plate in the streamwise direction) which provides a periodic behavior for the entire set up. Hence the heated area for the current measurement can be thought of as a representative of the entire jet array configuration. Jet diameter was used as a length scale for Nusselt number calculation.

Figure 43 shows the target wall Nusselt number contour comparison at the upstream and downstream section for the base line configuration at different jet Reynolds numbers. The horizontal gaps in all the Nusselt number contour profiles are the regions in-between heaters and have been cropped out for heat transfer calculation. The magnitude of heat transfer increases by increasing the jet Reynolds number for all the cases. The impinging positions on the target wall are clearly visible from the Nusselt number contour which shows higher heat transfer coefficients. The effect of crossflow becomes stronger from the fourth to sixth row of jets where the impinging positions of these three jet rows shifted downstream of jet centers. This shift can be attributed due to crossflow from the upstream jets gaining enough momentum to push the fourth to sixth jets to bend downstream. After $S/D \sim 35$, heat transfer decays significantly.

Turbulator Design

Three types of turbulators were tested: 1) 90° rib 2) W-1-shaped rib and 3) W-2-shaped rib. The W-1 shaped rib is defined as having the peaks of the W-shaped turbulator being in-line with the jet center line. The W-2 shaped rib is defined as having the valleys of the W-shaped turbulator in-line with the jet centerline. The rib configuration is similar from the study done by Maurer [46]. The turbulators are made out of Type 1 PVC and have a circular cross-section. The rib configuration is shown in Figure 40-42. and Table 9. The ribs used in the experiment do not participate in heat transfer.

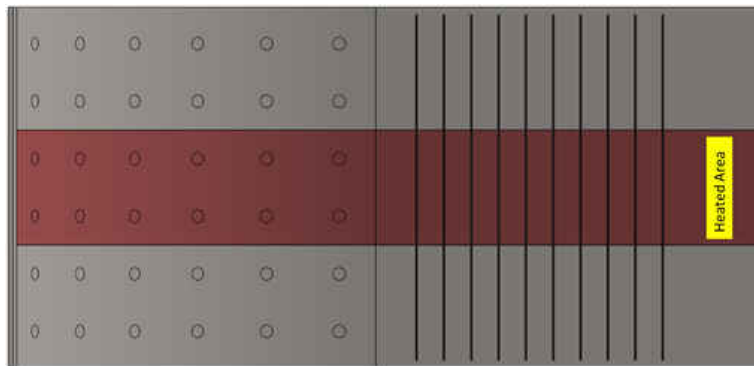


Figure 40 Turbulator - (90° rib)

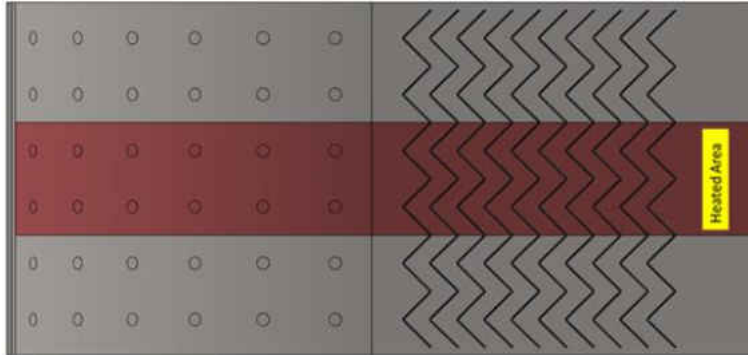


Figure 41 Turbulator- (W-1 shaped rib)

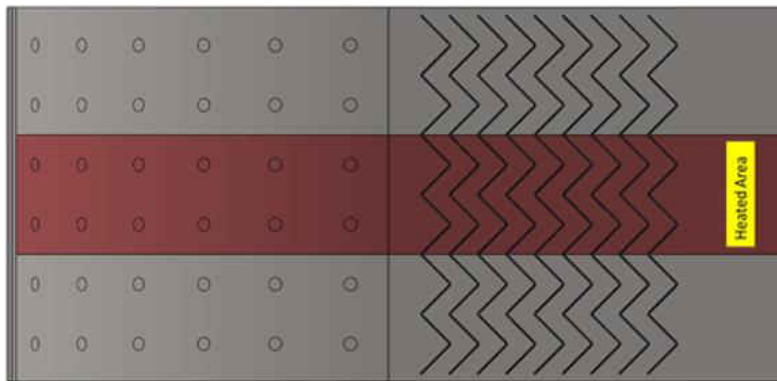


Figure 42 Turbulator- (W-2 shaped rib)

Table 9 Rib parameters

Rib Type	P/e	e/Z	Rib angle of attack	Number of Ribs
90° Rib	15	0.0476	90°	10
W-1Shaped	15	0.0476	45°	10
W-2Shaped	15	0.0476	45°	10

Post-Impingement Heat Transfer

Since the crossflow is not strong enough to have an impact on the heat transfer distribution for the downstream flat section, ribs were placed to trip the flow to promote higher heat transfer. Three different types of ribs were used for heat transfer augmentation. It was found that the presence of ribs does not have any impact on the upstream heat transfer distribution. Figure 43 shows the

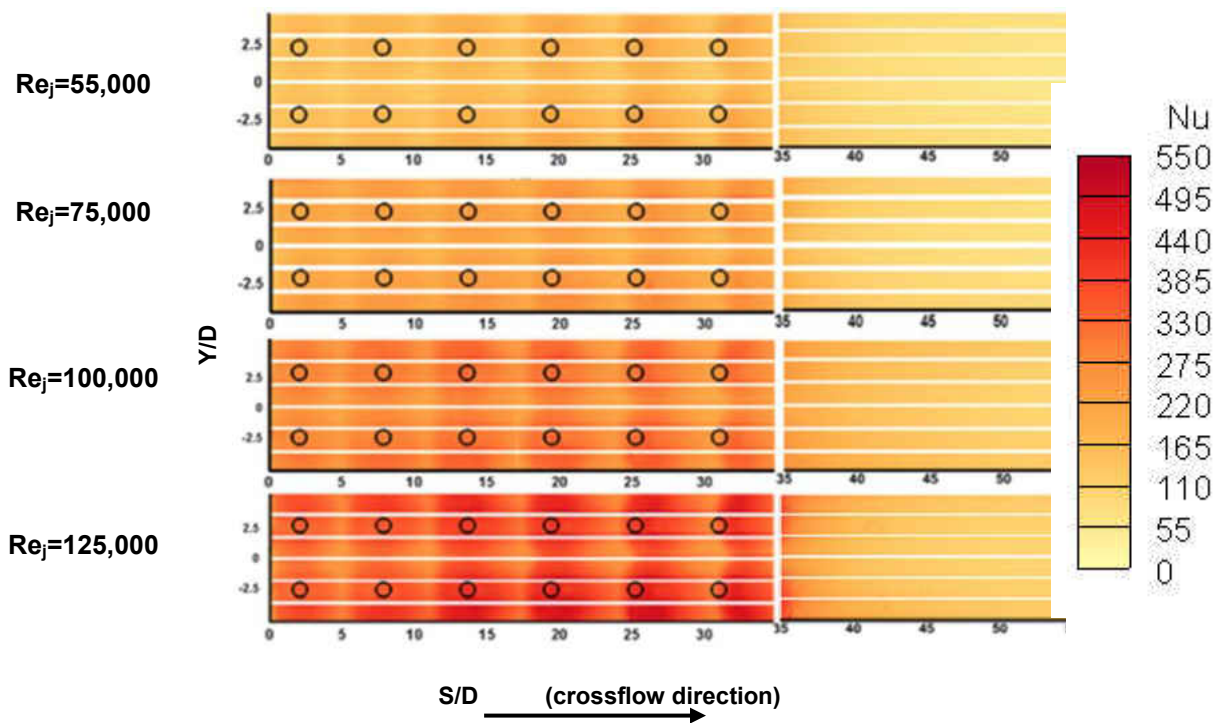


Figure 43 Nusselt number profile for the baseline configuration; Upstream curved section (left) & downstream flat section (right)

comparison of the heat transfer distribution between the turbulator cases and baseline case at downstream. The Nusselt number profile shows a repetitive pattern in heat transfer for all the turbulator features. All the features (W-1 shaped, W-2 shaped, and 90°) show improvement in heat transfer at the downstream section of the channel when comparing to baseline case for the same jet Reynolds numbers. For the 90° rib heat transfer increases right after each rib location. The first rib

disrupts the incoming boundary layer generated from the upstream crossflow and initializes the local mixing of the flow. After that, the ensuing ribs generate similar mixing through the downstream region. For the W-1 shaped ribs, higher heat transfer is observed at the rib peaks (rib tips that are facing the upstream flow). The rib peaks for the W-1 shaped ribs are aligned with the jet center location thus strong crossflow coming from the jet has a greater impact on the mixing of the flow near the rib tip. To understand the impact of crossflow and rib orientation on heat transfer, another configuration W-2shaped rib was tested. For the W-2 shaped rib configuration, the rib valleys are aligned with the jet centerline as oppose to the W-1 shaped rib where rib peaks were aligned with the jet centerline. Hence for the W-2 shaped configuration strong cross flow from the jet centerline will impact on the rib valley. From the W-2 shaped heat transfer result, it was observed that strong crossflow coming from the jet centerline does not have much impact on heat transfer when the rib valleys are aligned with jet centerline. Figure 44 shows that rib orientation with respect to cross flow has a greater impact on local heat transfer distribution. This suggests that while designing the W shaped rib in an impingement problem, the orientation of rib peak with respect to jet center location needs to be taken into consideration.

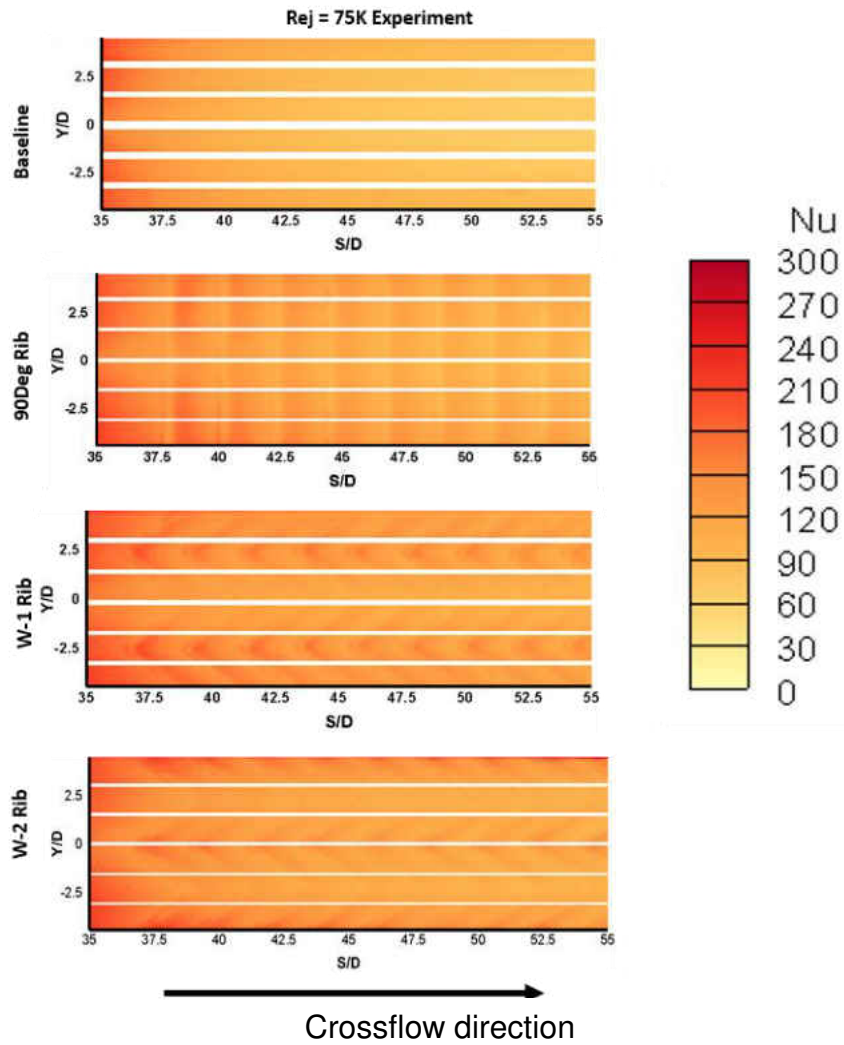


Figure 44 Heat transfer distribution in the post-impingement region for $Re_j = 125K$

Figure 45 shows the laterally averaged Nusselt number for the baseline case where no turbulator is present at the downstream flat section of the channel. The overall uncertainty in Nusselt number was calculated to be to 9.4%. Figure 45 shows the laterally averaged Nusselt number compared to the correlation developed by Florschuetz et al. [15] Although the average jet Reynolds numbers tested in the current study exceeds the Reynolds numbers tested by Florschuetz et al., the correlation is given for comparison to a known standard. It should be noted that the Nu peaks

continue to increase up to the 5th row, and this is not typically observed for impingement on flat target surfaces or predicted by Florschuetz et al. correlation. In fact, the authors' previous study (Harrington et al. [60]) on the same rig but on a flat target plate did not show this trend either. This observation is to an extent supported by computational results to be presented later, and merits further investigation with in-depth flow-field measurement (such as provided by PIV) in the future for the underlying physical reasons.

From the laterally averaged data, it is observed that the peak Nusselt number values are lower for the first two row of jets due to the curvature of the target plate, then increase from rows 3 to 6. It is also observed that heat transfer decays considerably after the sixth row, resulting in low heat transfer in this region.

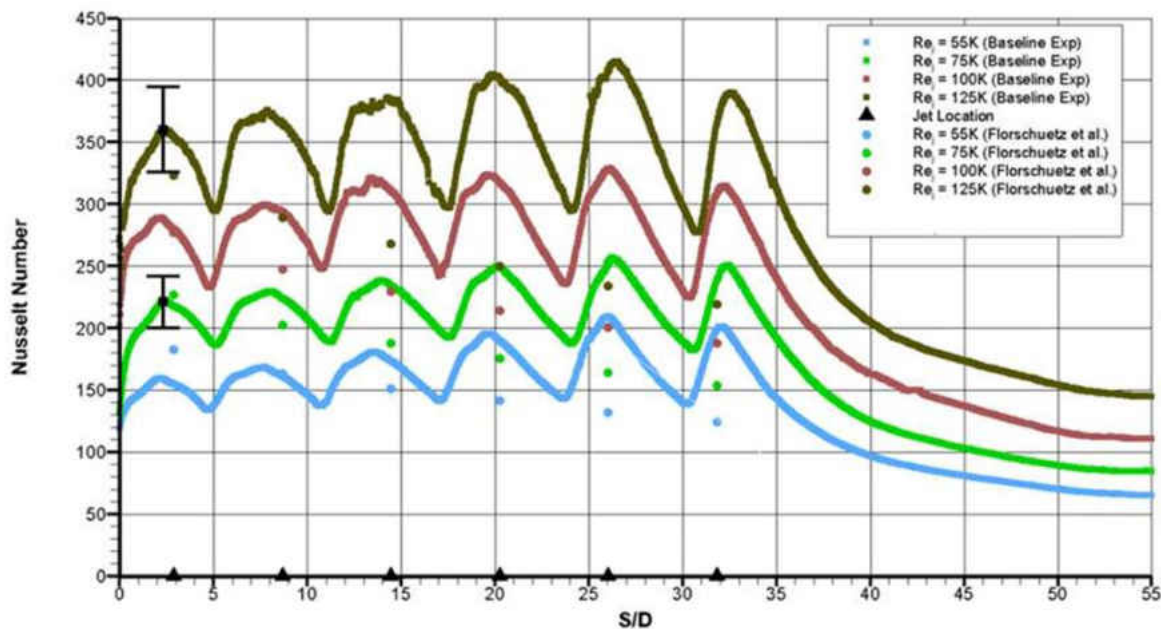


Figure 45 Laterally averaged Nusselt numbers for baseline curved surface (upstream and downstream)

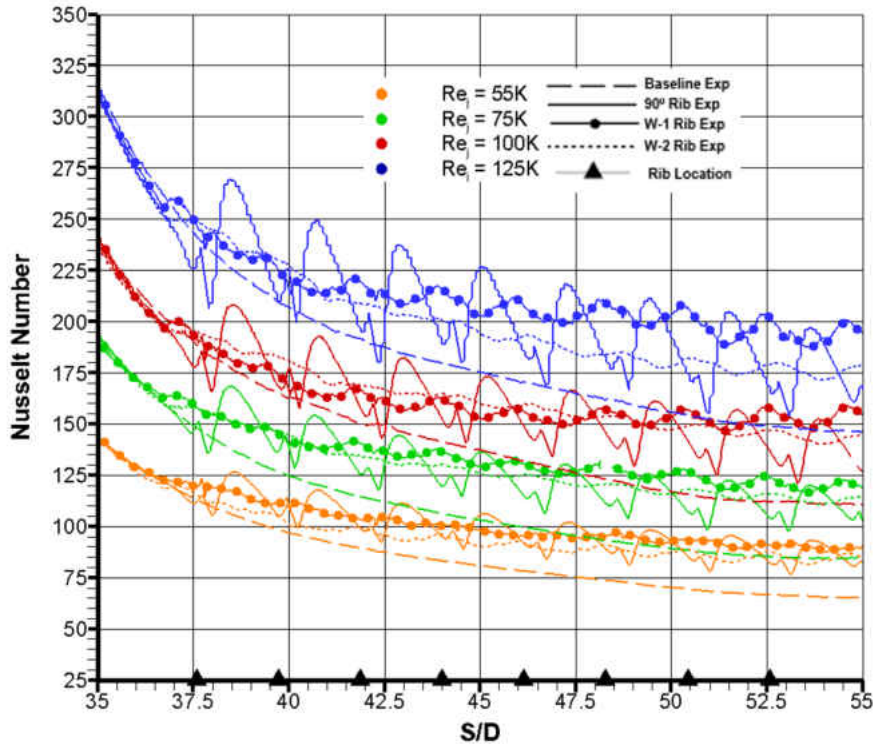


Figure 46 Laterally averaged Nusselt numbers at the downstream section (Baseline, 90° turbulators, and W-shaped turbulators)

Since the downstream section of the channel is somewhat similar to the channel flow configuration with the presence of turbulators, heat transfer coefficient based on bulk temperature from the energy balance was calculated. It was found that there is negligible difference on heat transfer results based on the plenum temperature and the bulk temperature. Hence, all the heat transfer calculation presented in the current study is based on plenum temperature. Figure 46 shows the laterally averaged Nusselt number at the downstream flat section for all configurations. The upstream distribution of heat transfer remains similar since the jet hole shape and Reynolds numbers are the same for all the configurations. At the downstream, for the both 90° and W-shaped (W-1 and W-2) turbulators the heat transfer increases compared to the baseline case. It was

observed that there is initially little difference in heat transfer between the baseline and turbulator cases, but further downstream this difference increases. As the crossflow comes in contact with the constant repetition of turbulators the turbulence increases throughout the downstream region leading to higher heat transfer. The locations of the turbulators (90°) and turbulator centerlines (W-shaped) are shown by the black triangle symbol in Figure 46 The profile shows a repetitive pattern in heat transfer for all the turbulator cases. Between the two types of turbulators tested, the W-shaped tabulator produced a more uniform heat transfer distribution. When compared to W-1 & W-2, turbulators W-1 shaped turbulators produced higher heat transfer than W-2 turbulators as the benefit of crossflow is maximized when rib peaks are aligned with jet center hole for the W-1 configuration.

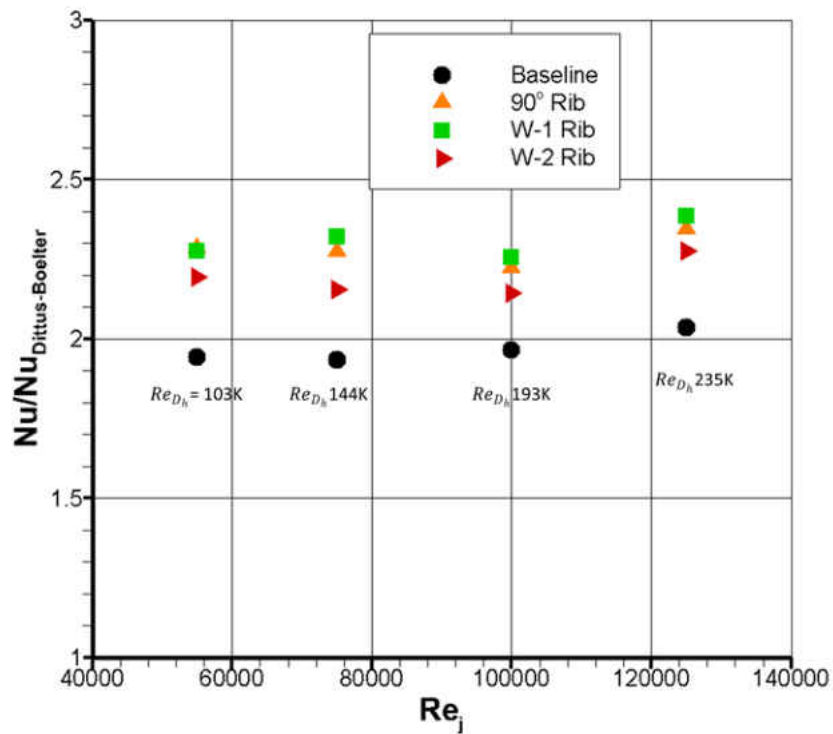


Figure 47 Heat transfer enhancement for the channel

Figure 47 shows the enhancement factor for the three types of configurations used in the current study. The enhancement factor was calculated by taking the surface average Nusselt number from each case and normalizing it with respect to the Dittus-Boelter correlation.

$$Nu_{DB} = 0.023 Re_{D_h}^{0.8} Pr^{0.4} \quad (63)$$

For all the jet Reynolds number, all the features show enhancement in heat transfer. The Nusselt number increases by a factor of ~ 1.94 for the baseline case, ~ 2.3 for the W-1 turbulator case and ~ 2.15 for the W-2 turbulator case respectively to that of Dittus-Boelter. The upstream flow structure caused by crossflow interaction is expected to have increased levels of turbulence. Even though there is no noticeable difference for enhancement factor using three different types of turbulators, it was found that the heat transfer is more uniform using W-shaped turbulators. This is more desirable from the design point of view as the temperature gradient is more uniform for W-shaped rib hence less thermal stress.

CFD Comparison

The downstream post-impingement heat transfer area was compared with CFD calculations. Figure 48 shows the Nusselt number contour obtained from the experiment and CFD for average jet Reynolds number of 125K. The Nusselt number contour from CFD shows good agreement with the experiment. The incoming crossflow generated from the upstream is deflected by the ribs and the flow follows different patterns for different turbulators, which are captured well by CFD.

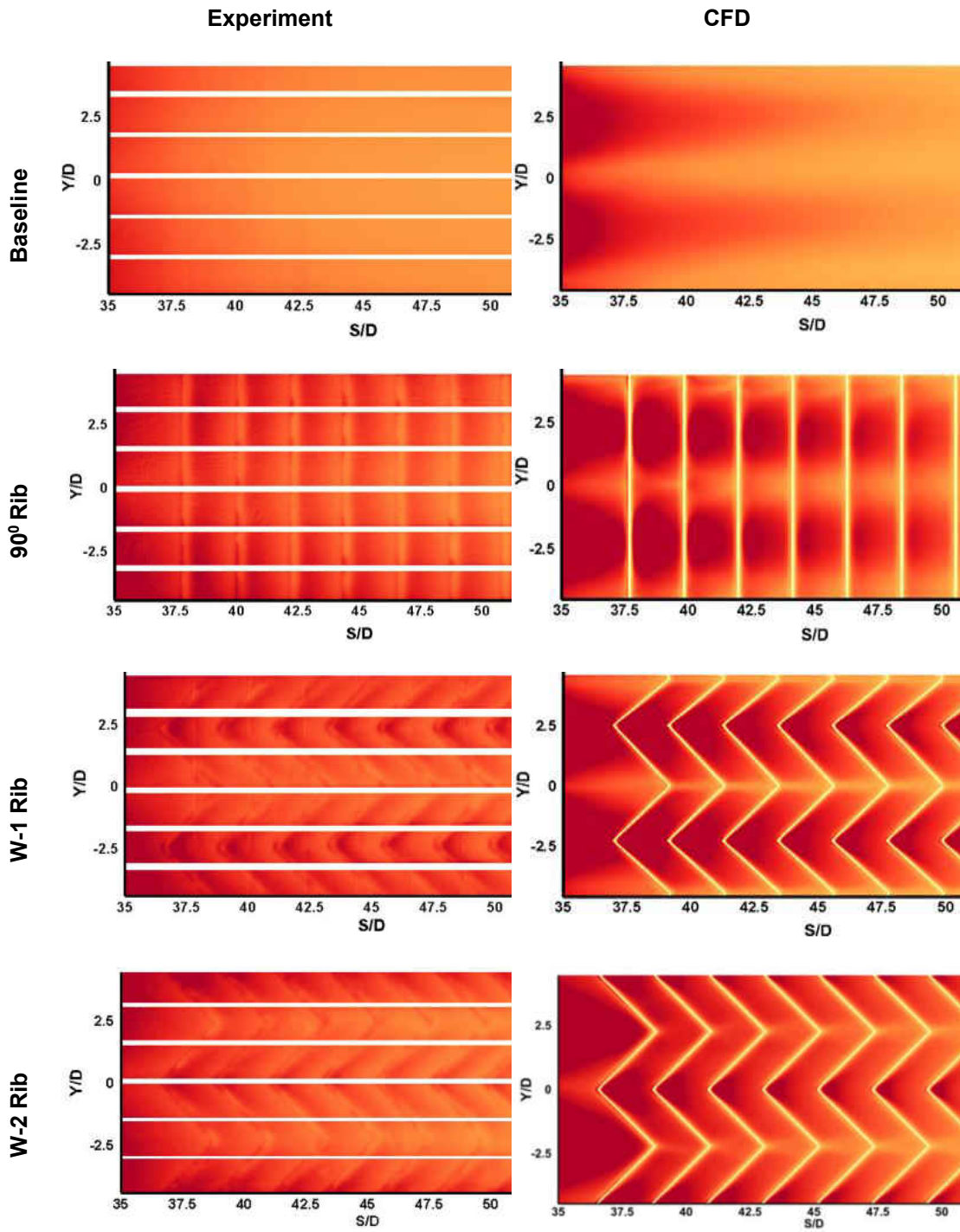


Figure 48 CFD comparison of Nusselt number for $Re_j=125K$

Figure 49 shows the laterally averaged Nusselt number from the experiment compared to CFD for the upstream impingement region. Zuckerman and Lior [87] reported that the v^2-f model can predict Nusselt number within 2–30% of the experimental value. The current CFD Nusselt number calculation shows that it is well within the experimental values obtained. It is also observed that from the fourth to sixth jets the location of the stagnation point predicted by CFD does not agree well with the experimental results. This indicates that CFD under-predicts the effect of crossflow. Hossain et al. [88] studied an aerothermal investigation of impingement heat transfer in a single row narrow impingement channel using Particle Image Velocimetry (PIV), CFD and Temperature Sensitive Paint (TSP). The authors found that CFD failed to predict the jet trajectory when compared to the PIV data. The current CFD prediction is consistent with the study done by Hossain et al. [88].

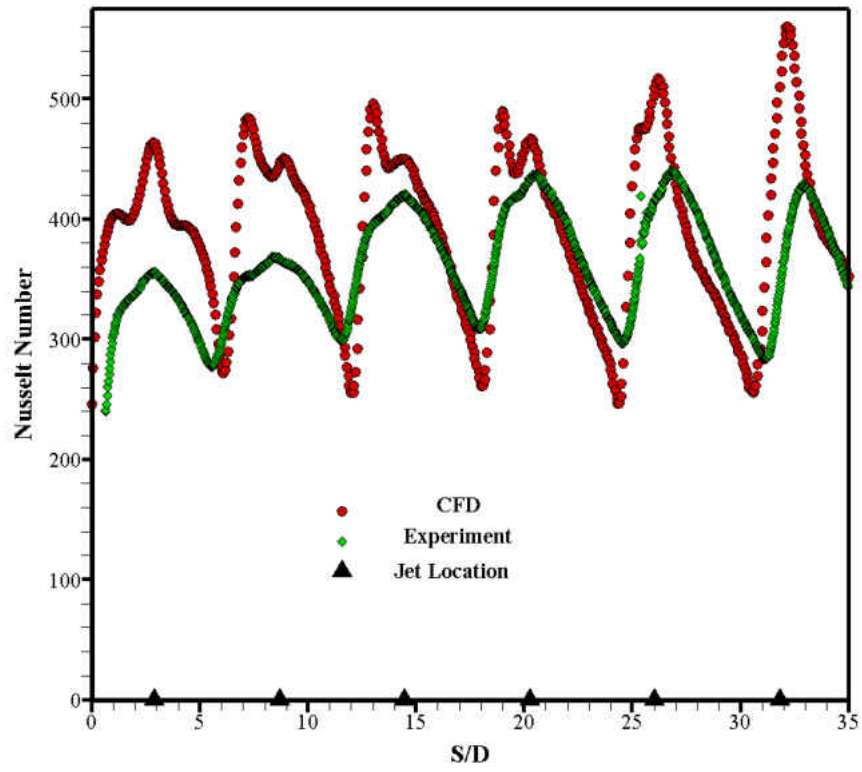


Figure 49 CFD vs Experiment: impingement heat transfer (Upstream)

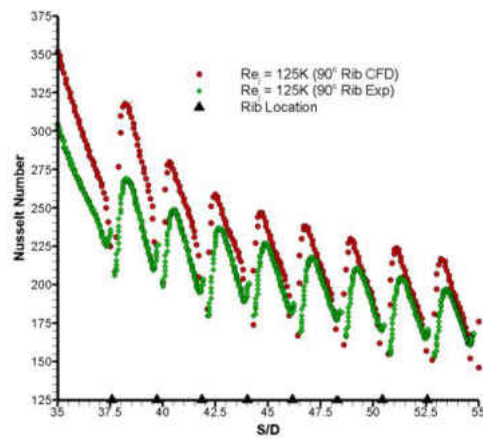


Figure 50 Laterally averaged Nusselt number comparison for 90° Turbulators ($Re_j=125K$)

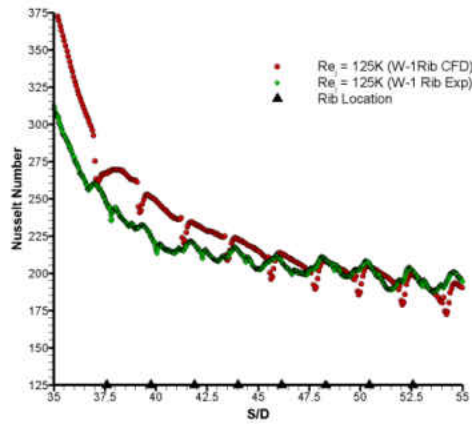


Figure 51 Laterally averaged Nusselt number comparison for W-1 shaped Turbulators ($Re=125K$)

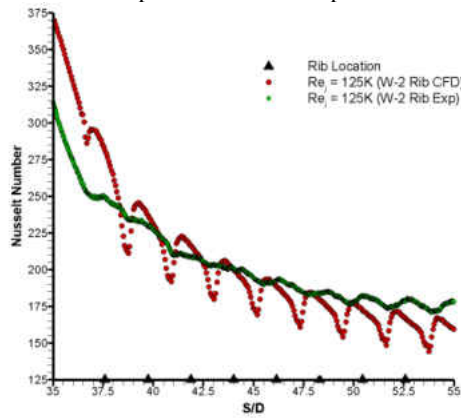


Figure 52 Laterally averaged Nusselt number comparison for W-2 shaped Turbulators ($Re=125K$)

Figure 50-52 show the laterally averaged Nusselt number from the experiment compared to CFD for 90° , W-1, and W-2 shaped turbulators. Figure 50 shows a higher peak averaged Nusselt number produced by the 90° turbulators due to large temperature gradient. CFD was able to predict the trend of the laterally averaged Nusselt number from the experiment well. Similar levels of augmentation were achieved using 90° and W-1 turbulators. However, the pattern of heat transfer for the W shaped turbulator (W-1 and W-2) and 900 rib shows different behavior. As described by Figure 51, the W-1 shaped turbulator shows uniform heat transfer distribution compared to the

90° turbulators. Due to multiple rib tips on the W-1 shaped turbulator configuration, multiple counter rotating vortices are created. Behind the rib, air flow is separating, which leads to a recirculation and low pressure region. In the process, fluid flow is diverted from the rib tip towards the trailing edge of the rib. The secondary air flow structures created by the W-1 shaped turbulators leading to a higher level of turbulence and mixing and therefore a more uniform behavior in heat transfer than 90° turbulator. Figure 52 shows the effect of rib orientation with respect to crossflow for the W-2 shaped turbulators. Since the strong crossflow exiting from the last row of jet are not aligned with the rib peak, the benefit of the crossflow is not being maximized for this configuration. Therefore the peak in heat transfer is not as prominent as W-1 shaped turbulators for the W-2 configuration.

To understand the mixing process between the 90° and W-1 turbulator, CFD was used to extract the complex flow features at the downstream section of the channel where ribs are located. Figure 53 (a, b, c, d) shows the detailed flow visualization at the downstream section of the channel in the direction of cross flow. The streamlines calculated from the CFD reveals the flow direction created by the 90° and W-1 turbulators. Velocity magnitude is also enacted on the streamline path in Figure 53. Figure 53(a) shows the streamlines corresponding to the 90° rib. For the 90° rib, the streamlines follow the crossflow direction and no secondary flow features were identified. Since the flow has to travel in one direction for the 90° turbulator, there is no mechanism for the flow to accelerate unlike the W-1 turbulator where the flow accelerates near the rib tip as can be seen in Figure 53 (b). Due to multiple rib tips on the W-1 shaped turbulator configuration, multiple counter rotating vortices are created. Behind the rib, the air flow is separates, which leads to a recirculation

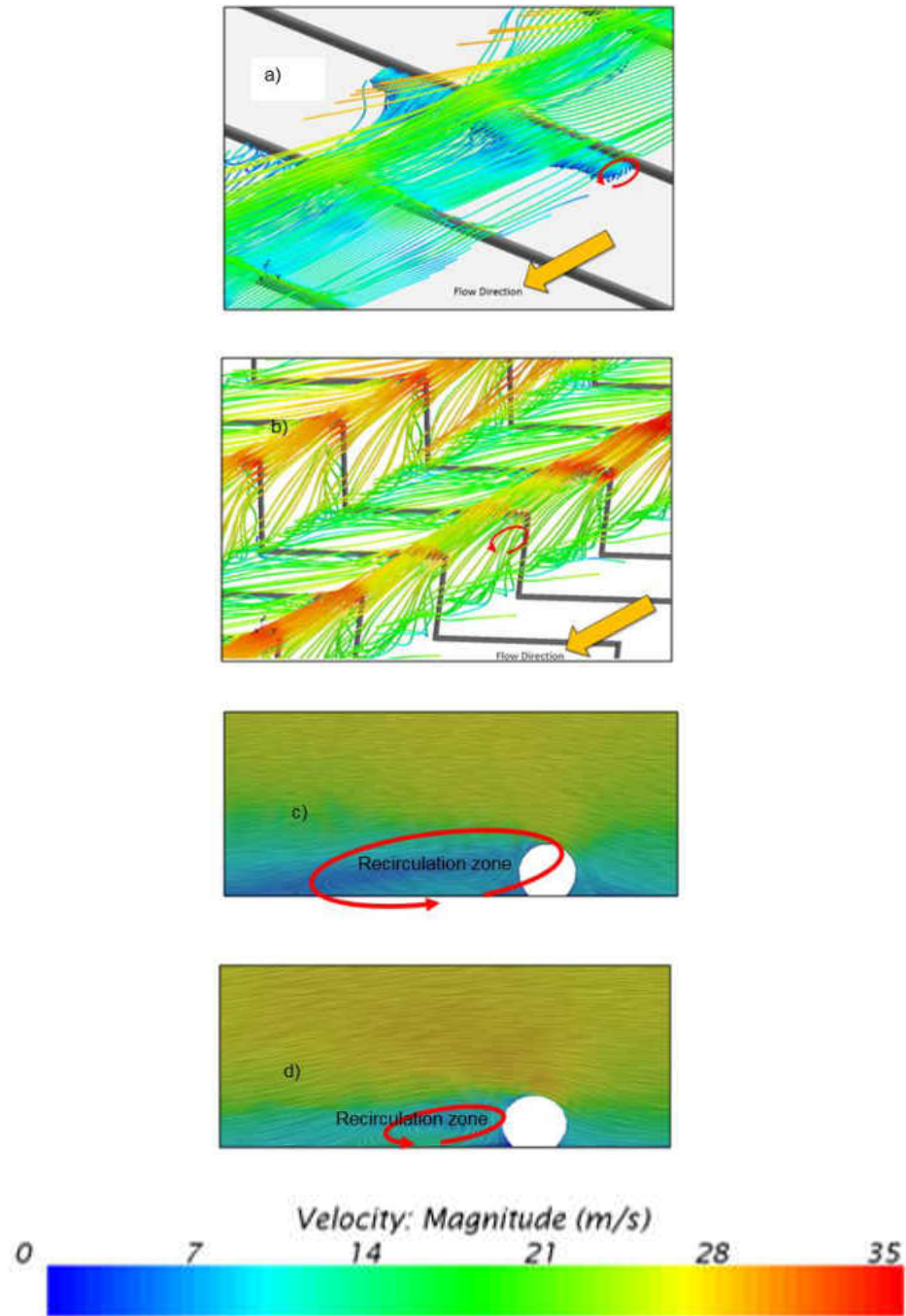


Figure 53 Flow streamlines: a) 90° turbulator b) W-1 shaped turbulator c) Primary recirculation zone for the 90° turbulator d) Primary recirculation zone for the W-1 shaped turbulator

and low pressure region. In the process, fluid flow is diverted from the rib tip towards the trailing edge of the rib. Thus, the overall mixing for the W-1 shaped turbulator is better than the 90° rib.

Array Impingement

Temperature sensitive paint was used to obtain a local heat transfer distribution across the entire target surface. The impingement configuration is interesting because the current array configuration fall outside of the Florschuetz test matrix. Table 10 highlights the difference between current configuration and the Florschuetz configuration. This array impingement geometry is adopted from [59]

Table 10 Variation of the geometry

	Current Study	Florschuetz Study
x/D	3	5-15
z/D	3	1-3

The total number of rows in the streamwise direction is 20 while the number of rows in the spanwise direction is four. The jet-to-target plate spacing was kept constant at $z/D=3$. Little research has been conducted on array with low streamwise jet spacing. The heat transfer and flow characteristics of the current wide array impingement configuration with low streamwise spacing is studied to better understand the physics of the flow for average jet Reynolds number of 20,000. PIV was used for experimental flow visualization. Finally CFD was used to compare the experimental results.

Experimental Heat Transfer Results

Local heat transfer profile was obtained using temperature sensitive paint (TSP). El-Gabry and Kaminiski [57]

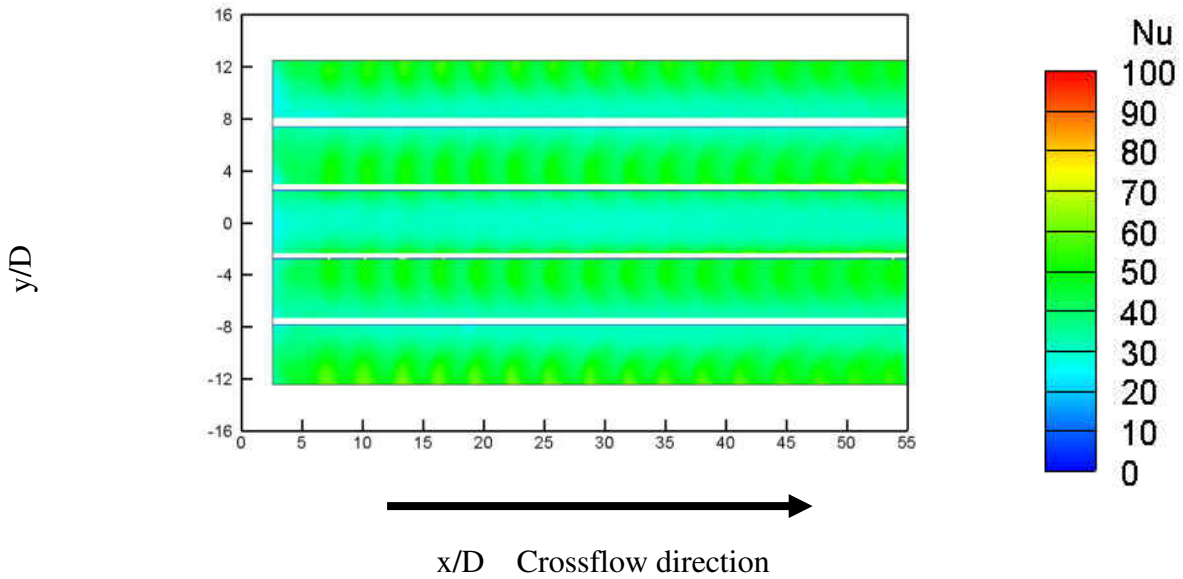


Figure 54 Nusselt number profile for $Re_j=10,000$

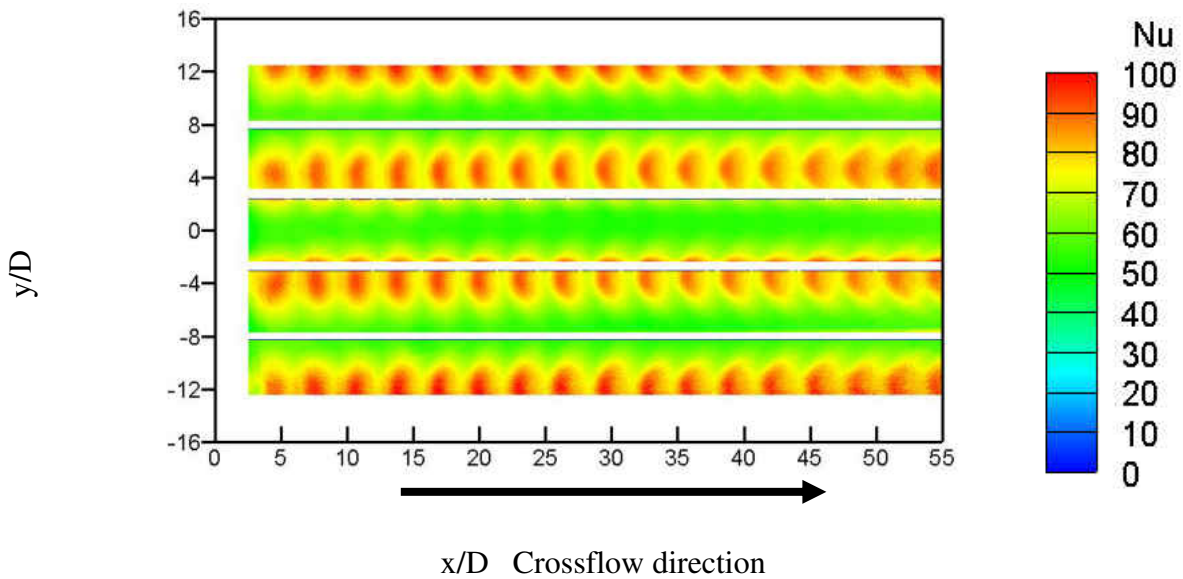


Figure 55 Nusselt number profile for $Re_j=20,000$

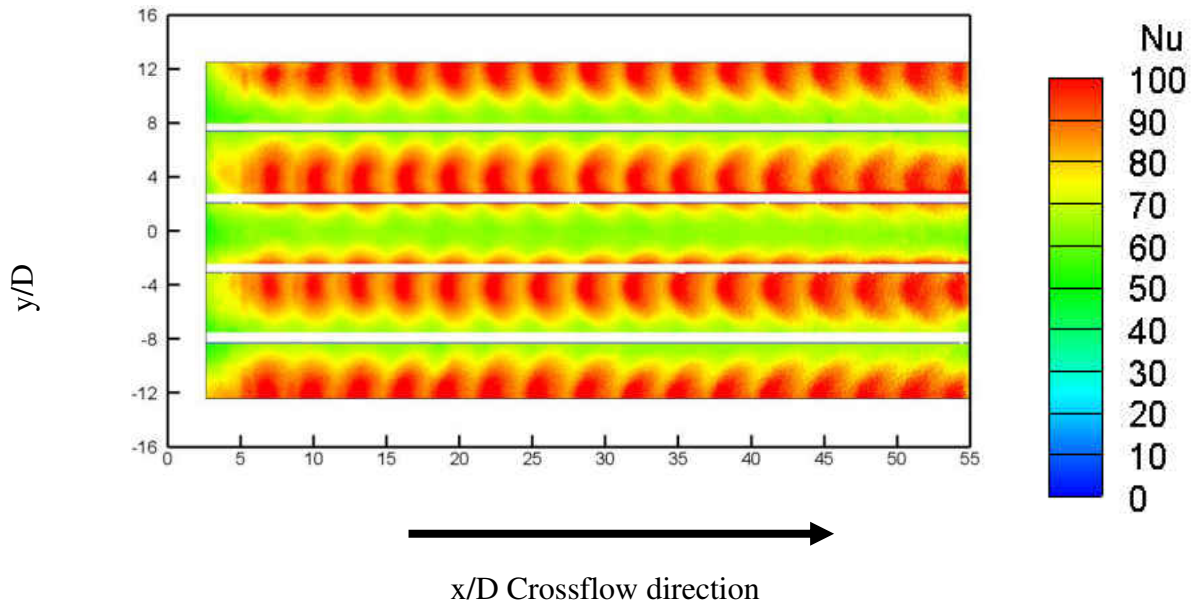


Figure 56 Nusselt number profile for $Re_j=30,000$

emphasized the importance of acquiring the local heat transfer distribution for impingement cooling. First, a local heat transfer distribution gives insight about the temperature gradient to the designer. As a result designs based on local heat transfer are less likely to fail in practical operation. On the other hand designs based on averaged heat transfer are more likely to fail in practical operation due to lack of information on the temperature gradient. Second, results obtained from local temperature distribution can be used to validate CFD results so that CFD can be used as a reliable design tool in the industry. Figure 54-56 show the Nusselt number profile for three different jet Reynolds number. The heated area on the target plate was designed in way that it provides a periodic behavior for the entire heat transfer setup. The heated area for the heat transfer calculation ranges from ($y/D=-12.5$ to $+12.5$, where $y/D=0$ represents the center of the target plate in the streamwise direction. The horizontal gaps in all the Nusselt number contour profiles are the

regions in-between heaters and have been cropped out for the final heat transfer calculation. The first jet and the last two jets heat transfer distribution was not possible to measure due to location of the bas bars situated beneath the corresponding jets. Therefore Figure 54-56 represents the jet rows from 2-18. Figure 54-56 show the magnitude of Nusselt number increases as the jet Reynolds number increases. Jet diameter was used as length scale for the calculation of Nusselt number. The impinging positions of the jets are visible near the stagnation region where the heat transfer is the highest. The thermal imprint of the first few jets are similar to an oval shape, further downstream as x/D increases, the Nusselt number profile is distorted due to the crossflow and produced a kidney shape thermal imprint of the target surface. To further understand this mechanism a 3D iso-contour of velocity magnitude was generated from the 3D CFD simulation. Figure 57 shows iso-contour of velocity magnitude.

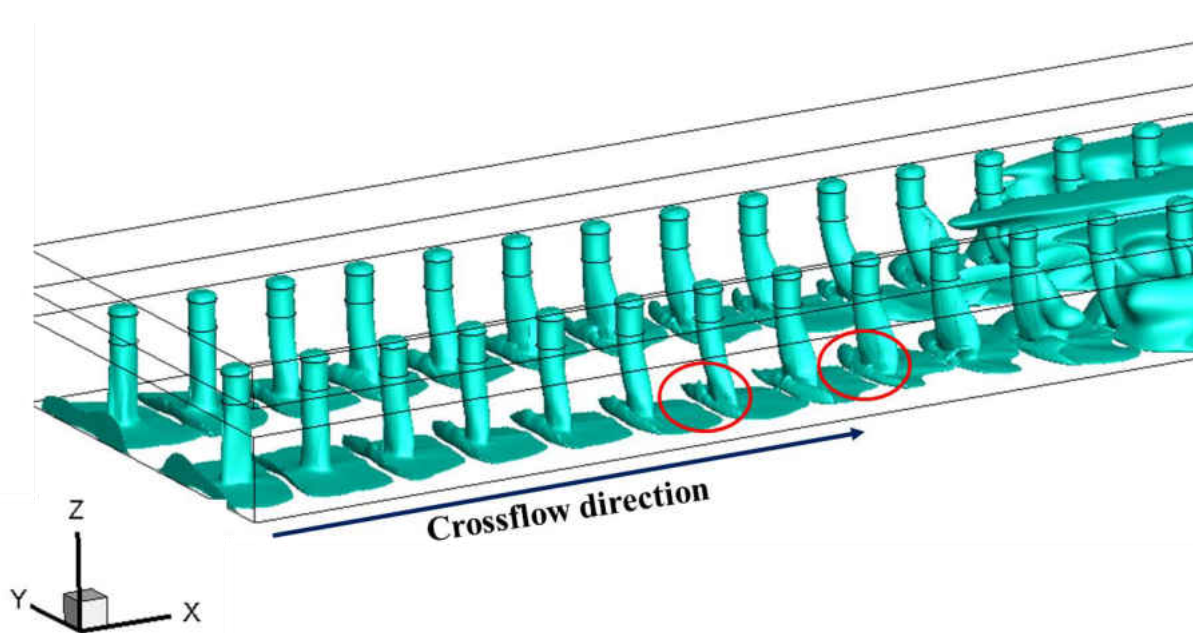


Figure 57 Iso-surface of velocity magnitude (25 m/s)

Figure 57 shows the jet bending mechanism due to crossflow generated by jet to jet interaction. Initially the first few jets behaves like an orthogonal jet. As the crossflow gains momentum it starts to force the jet to bend in the direction of crossflow. As the wall jet interacts and wall jet recirculation zone develops, the crossflow from the previous jet push this wall jets to go pass around the next jet. This phenomena caused the jets to bend and this is consistent with the thermal imprint behavior obtained from the experiment shown in Figure 54-56.

The heat transfer characteristics were further analyzed by averaging all the values in the spanwise direction and plotting them in spanwise direction. Figure 58 shows the lateral averaged Nusselt number for all the jet Reynolds number. The jet locations are shown by a triangle symbol in Figure 58. The Nusselt number generated by the first five jets has the highest peak value in the entire array. The bending of the jets can be observed after the seventh jet as the Nusselt number starts to deviate from the corresponding jet centerline. The value of Nusselt number starts to decrease after sixth jet. This is expected due to crossflow is gaining momentum to bend the jets. Near the exit of the channel the heat transfer start to increase due to enhance mixing inbetween jets. Similar trends of heat transfer behavior was observed for the other Reynolds number tested in the experiment.

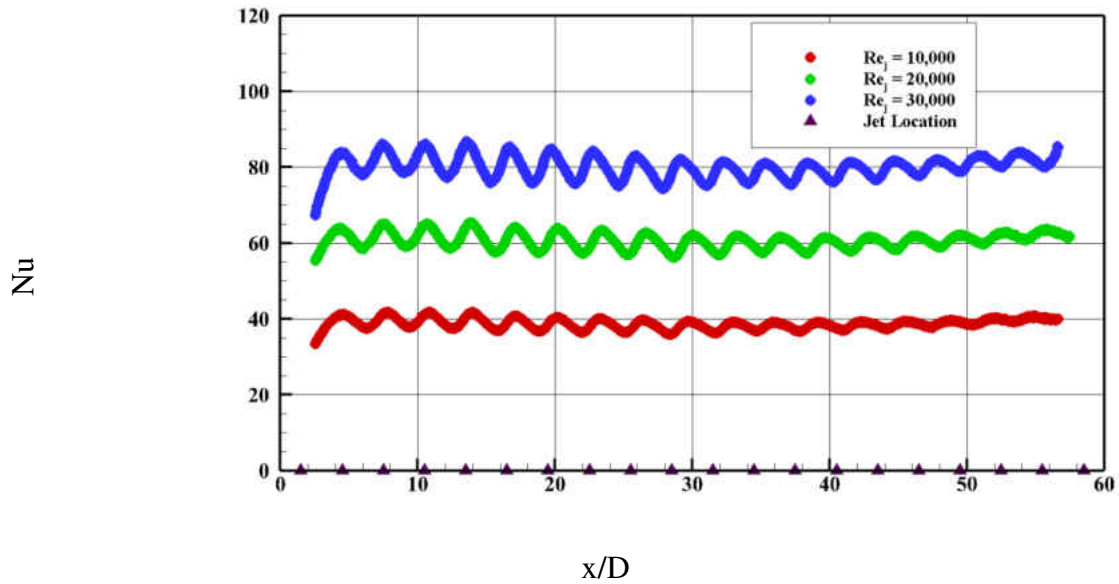


Figure 58 Laterally averaged Nusselt number profile

CFD Comparison

Heat Transfer: CFD was carried out for only jet average Reynolds number of 20,000. Figure 59 and Figure 60 shows the Nusselt number comparison between CFD and experiment. Even though the magnitude of Nusselt number prediction is higher in CFD than in the experiment, the thermal imprint of the jet shapes were predicted well by CFD.

Experiment

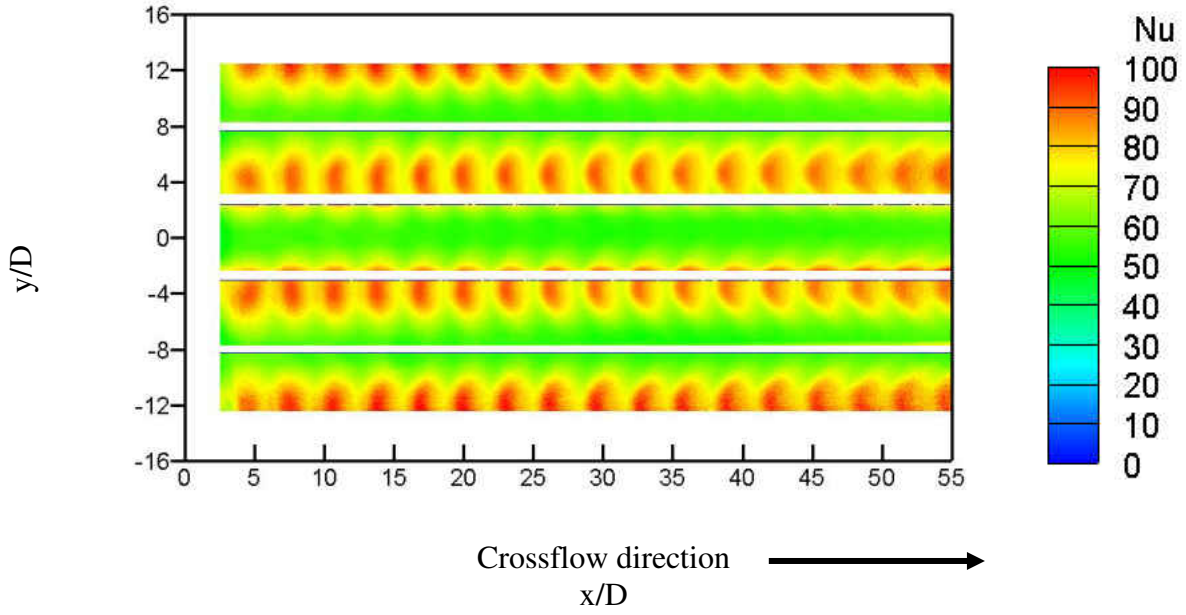


Figure 59 Nusselt number profile for $Re_j=20,000$ (Experiment)

CFD

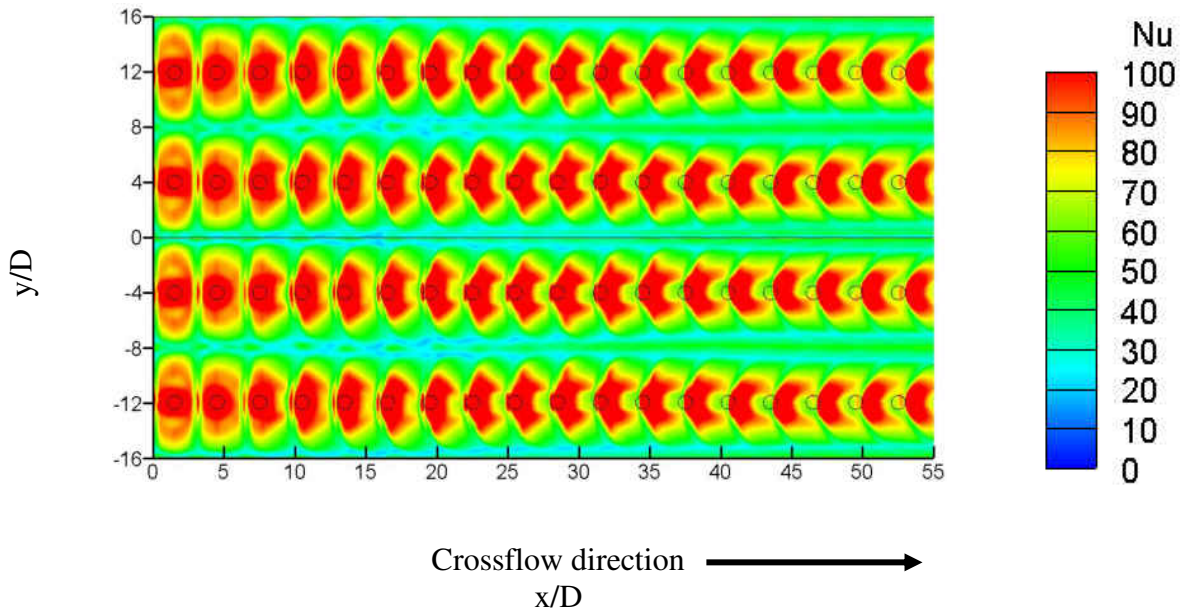


Figure 60 Nusselt number profile for $Re_j=20,000$ (CFD)

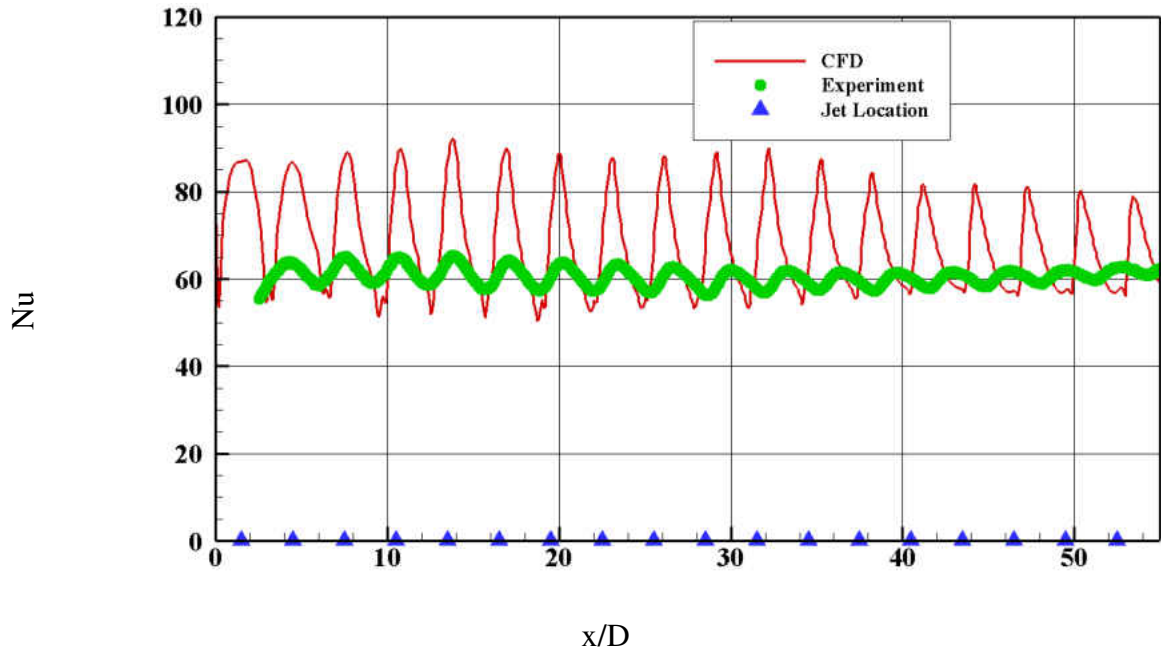


Figure 61 Laterally averaged Nusselt number comparison

Figure 61 shows the laterally averaged Nusselt number comparison for the jet Reynolds number 20,000. The magnitude of the heat transfer is high in CFD prediction which is a very common problem for impingement heat transfer. Discrepancies between CFD and experiment is observed after $\sim x/D$ 25. The lateral averaged Nusselt number profile deviates from the experiment after this location suggesting the bending of the jets are not accurately predicted by CFD.

Velocity Comparison:

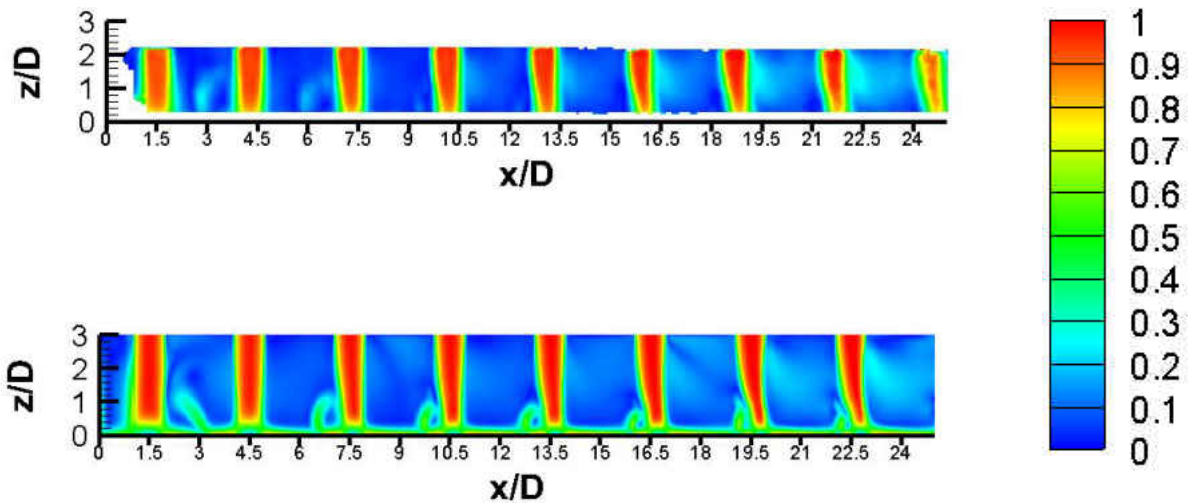


Figure 62 Velocity contour comparison between CFD (top) and Experiment (Bottom).

Figure 62 shows the velocity magnitude contour comparison between CFD and experiment. The location the PIV measurement plane is shown in Figure 63. The velocity values are normalized by the maximum velocity in the domain. The jet trajectory, mixing of the flow in between jets, the upwash, the diffusion in the jet shear are appears to be found different in CFD than in the experiment. Moreover the jets appears to be stronger in the CFD calculation.

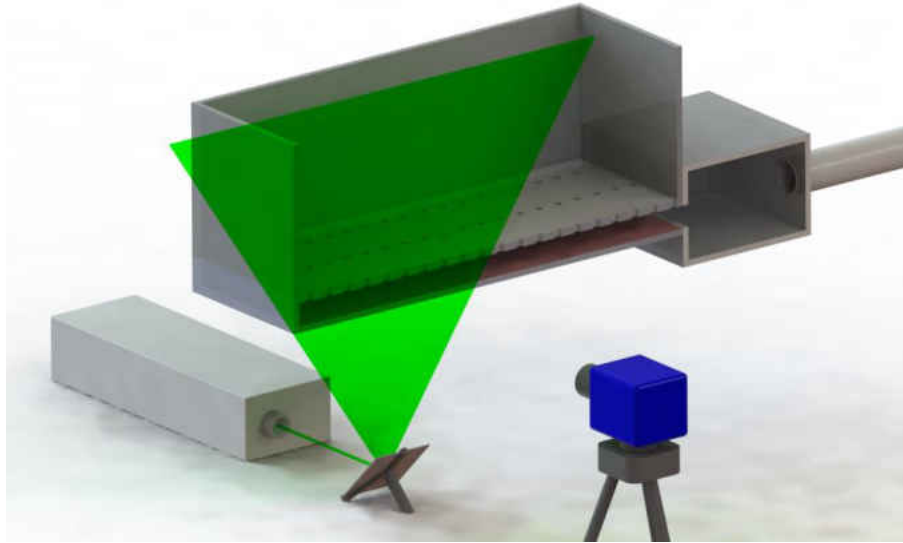


Figure 63 PIV layout for the first 10 jets

Narrow Wall Impingement

Heat Transfer: RANS vs Experiment

As stated in [88], Figure 64 and Figure 65 shows a detailed contour plot of Nusselt numbers at the target wall from the experiment and CFD for all the jets. The average jet Reynolds number for both CFD and experiment is 30,000. From the experimental thermal print, the first three jets appear to act similar to round impinging jets on an open, flat surface. Past this, the jets begin to take an elliptical shape; this change in shape can be attributed to the jets bending due to interaction with the crossflow. The area between the third and fourth jets can be considered the transition region where the crossflow begins to take effect on the heat transfer distribution of the channel. In order to gain more insight about the comparison and behavior of experimental and numerical heat transfer, spanwise averaged Nusselt numbers were calculated as shown in Figure 66. From this figure, it is clear that heat transfer distribution is significantly high for the first few jets in both the experiment and CFD near their stagnation region. Heat transfer at the stagnation region begins to decrease as the cross flow starts to gain enough strength to deflect the jets. In the experimental contour plot of Nu number, heat transfer starts to decrease after the 7th jet; towards the end of the channel, the Nu number peaks begin to even out, indicating that the jets do not impinge directly onto the target wall. Both in CFD and the experiment, the local heat transfer distribution is lower in between two jets. This can be attributed to the fact that fountain flow is created by two adjacent jets, pushing the flow upwards and hence lowering heat transfer in that region.

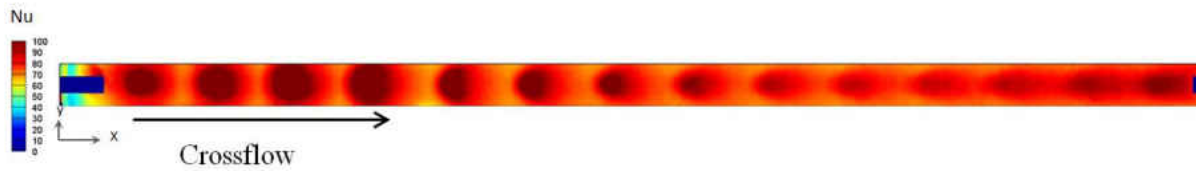


Figure 64 Nusselt number contour (experiment)

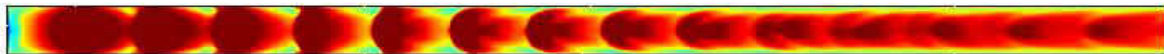


Figure 65 Nusselt number contour (CFD)

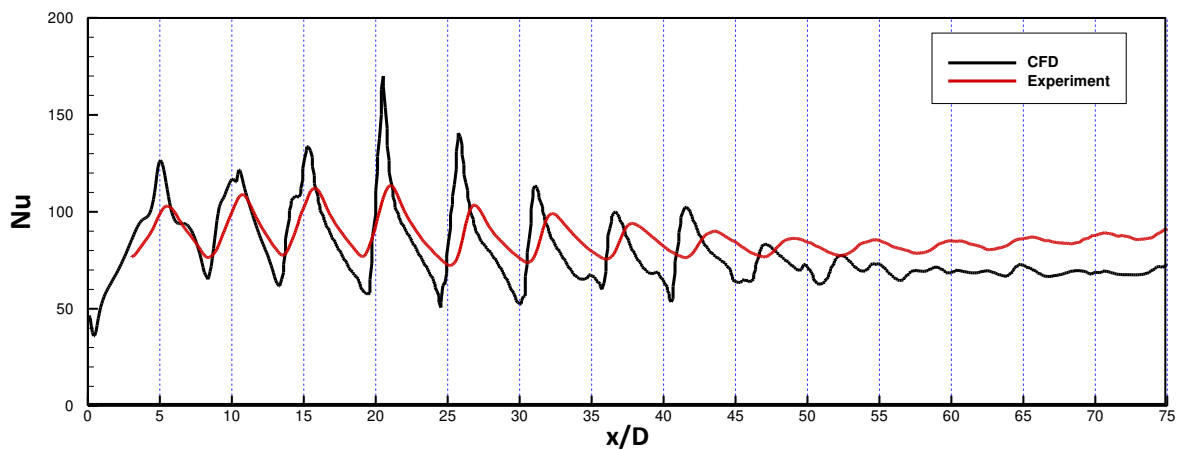


Figure 66 Laterally averaged target wall Nusselt number distribution at the target wall

Predicting stagnation heat transfer using RANS models is always difficult [87]. Near the stagnation region of the fourth jet, CFD over predicts heat transfer by approximately 55%. This location represents the largest discrepancy between CFD and experimental heat transfer. Even though the magnitude of heat transfer in CFD is higher for the first four jets, the overall trends are similar to the experiment. The x/D location of the peaks in heat transfer distribution for the first four jets is almost identical in both CFD and experimental results. However, the location of the peaks in CFD

calculations starts to lag behind experimental peaks after the 4th jet. This trend continues as the jet moves downstream. In the CFD calculations, the transition region begins later than the experimental results; the transition region for CFD begins after the sixth jet. It is apparent that the CFD is not capturing the crossflow effects well, hence the further transition region. Although the CFD significantly over predicts the spanwise averaged Nusselt number, it over predicts the overall area averaged Nusselt number by only 2% of the experimental results. More detailed experimental flow visualization is required to confirm the conjecture on the discrepancy between experimental and CFD heat transfer results.

Flow Visualizations: RANS vs Experiment

This difference of heat transfer in the experiment and CFD can be explained by the jet trajectory behavior at the location of the peaks through flow visualization and CFD. Jets are assumed to be faster in that region in CFD than in the experiment, and hence the jet bends less from the crossflow. This discrepancy accumulates in the CFD calculations and fails to match the experimental trend at the downstream portion of the channel. Figure 67 shows the location of the PIV planes where the data was collected and processed. Planes A, B, and C represent the velocity contour of the 2nd, 6th, and 14th jet, respectively.

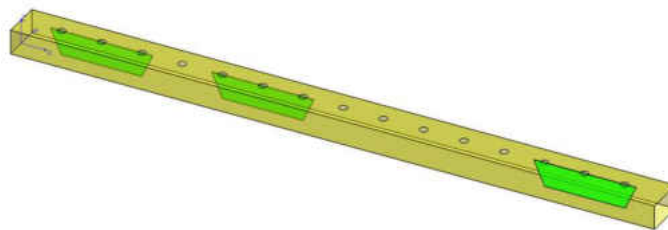


Figure 67 Measurement Planes for PIV experiment

The time averaged mean velocity field from the PIV measurements were compared with CFD calculations. The streamlines are plotted on the velocity magnitude contour plot to show the jet trajectory. Figure 68 shows a comparison between the experiment and CFD for the 2nd jet. The upwash fountain and recirculation due to collision between wall jets was captured well in CFD.

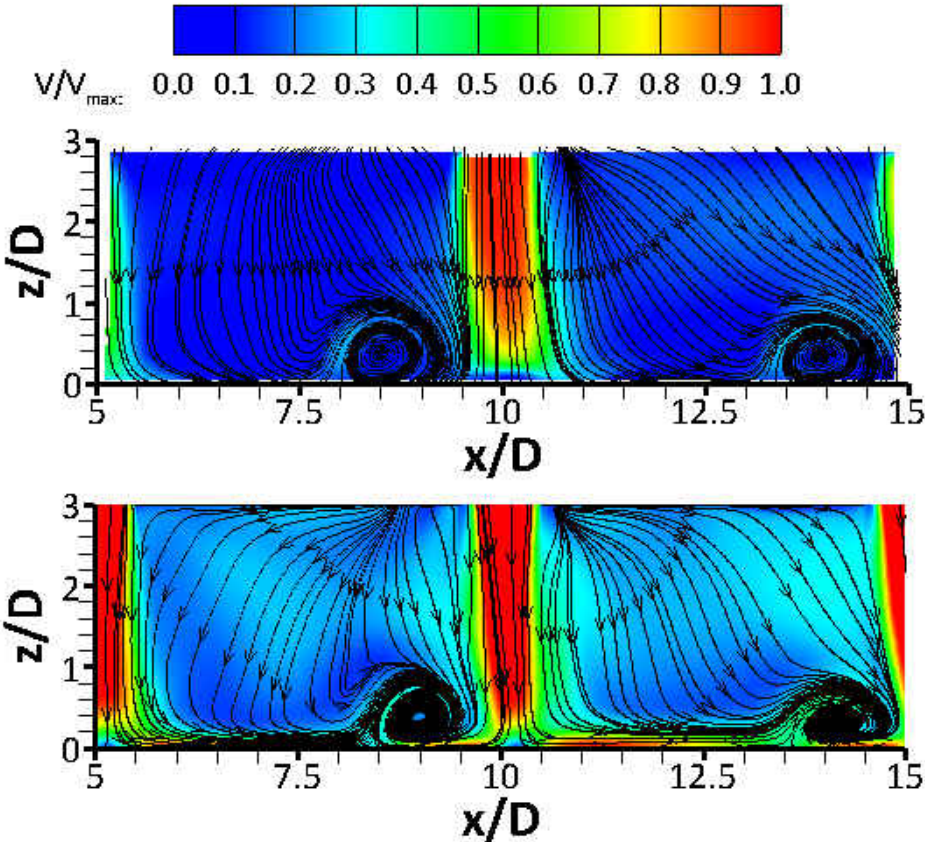


Figure 68 Jet axial velocity contour for the 2nd Jet; Experiment (Top) and CFD (Bottom)

Figure 69 shows the comparison for the 6th jet. As discussed earlier, the shifts of Nusselt number peaks in CFD calculations start after the 4th jet and continues to deviate from experimental results. The difference in jet trajectory between the CFD and experiment is clearly visible. The velocity is much faster for the 6th jet in CFD as compared to PIV; the jet also penetrates more in CFD. The difference in jet trajectory can be explained by the behavior of crossflow in the channel. The magnitude of crossflow velocity in CFD is much less than that of the experiment; the crossflow does not have enough momentum to bend the jets as in experiment. For example, when comparing the nondimensional crossflow velocity magnitude at $x/D = 27.5$, there appears to be very minimal effects of crossflow taking place for the CFD calculations when compared to the experiment. As a result, the transition region occurs further downstream in CFD.

To further verify, the jet trajectory was compared for the 14th jet to determine whether the dissimilarity can be observed further along the channel. A similar trend was indeed found at plane C, which can be seen in Figure 70. At this plane, the jets have significantly bended in the crossflow direction. This suggests that the transition region has already occurred before this jet, and the crossflow has built up enough momentum to significantly deflect the jets. When considering nondimensional crossflow velocity at $x/D = 69$, it is apparent that the crossflow effects are very similar between the experiment and CFD.

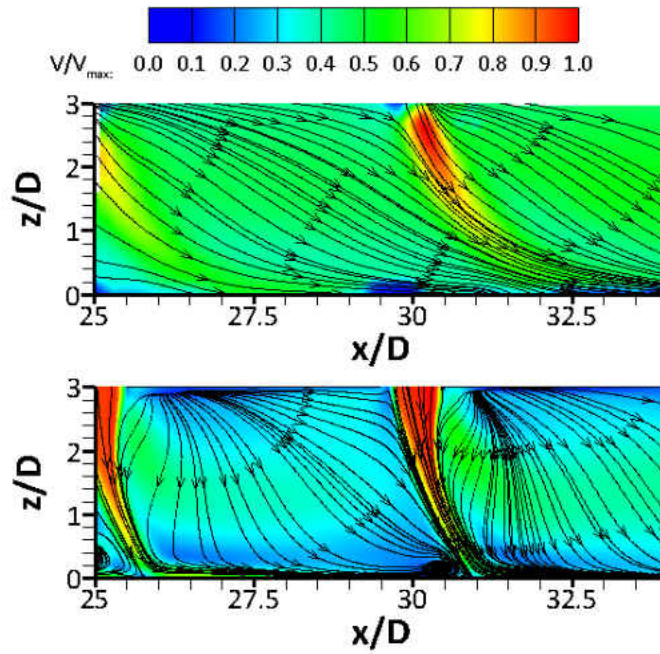


Figure 69 Jet axial velocity contour for the 6th Jet; Experiment (Top) and CFD (Bottom)

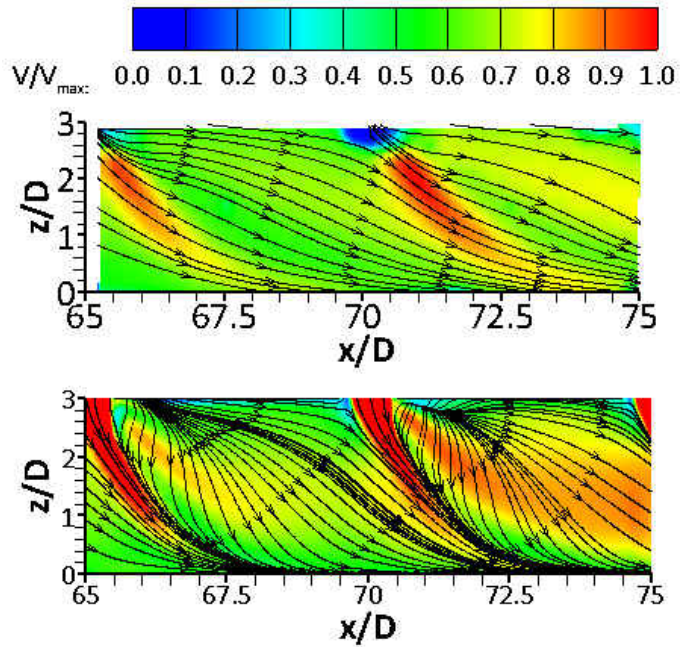


Figure 70 jet axial velocity contour for the 14th Jet; Experiment (Top) and CFD (Bottom)

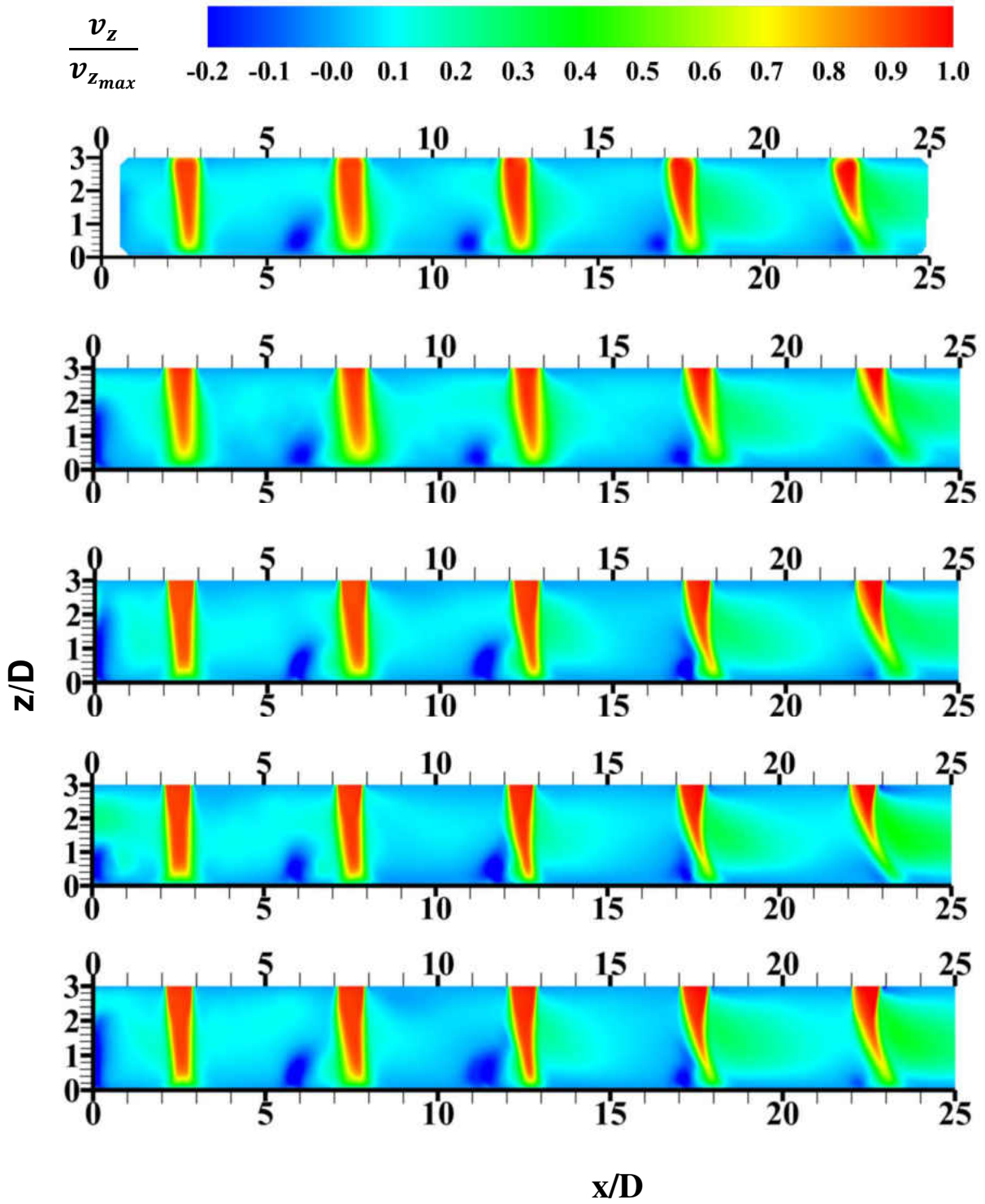
Simulating an impingement problem in a narrow wall channel is an inherently complex problem. Initially, the first few jets behave like orthogonal impinging jets. Past the transition region, the problem behaves as a jet in crossflow. Hence, simulating a narrow wall impingement channel involves modeling two different complex problems. Flow features like jet-to-jet interaction, stagnation flows, the upwash fountain flows, and recirculation due to collision of wall jets between adjacent jets makes the flow field inside the channel highly anisotropic. The discrepancies in the flow features in numerical calculation can be attributed to inherent inaccuracies of turbulence modeling [25].

CHAPTER 7: DETAILED FLOW FIELD ANALYSIS

Mean Axial Velocity Contour

As stated in [86], time averaged mean axial velocity fields from PIV measurements were compared with CFD calculations. All boundary conditions in numerical calculations are selected to be as close as possible to the experimental conditions. LES and three other RANS turbulence models (*SST $k - \omega$* , RSM, and *v^2-f*) were used to compare with experimental results. These three RANS turbulence models are typically used for industrial applications due to their accuracy on predicting mean components and lower computational expense for modeling various engineering problems.

Figure 17 shows the location of the PIV plane where data was collected, processed and analyzed. This plane is located at the centerline plane of the channel, on jet. The mean axial velocity values in the contours shown in Figure 71 were normalized by the maximum axial jet velocity for each respective model. PIV and LES shows excellent qualitative agreement of velocity contours for all jets at the midplane of the channel. The jet potential core, jet diffusion, jet shear layer, the upwash and the wall jet vortices were captured well by the LES. The jet bending due to crossflow from the third to fifth jet are accurately predicted in LES. The jet diffusion and the penetration of the potential core are also very similar to the experiment, when compared to the LES calculation.



Type ec

Figure 71 Axial velocity magnitude contour profile at the centerline plane ($x/D, z/D=0, 0$) of the channel

In general, for all the RANS simulations the flow field is somewhat different than in the experiment. In the RANS simulations, for the first three jets, the length of the potential core extends very close to target wall. The jet also penetrates more in RANS simulation. A larger difference is observed for the spreading and diffusion of all jets in the RANS models. The jets appear to have less spreading while travelling towards target wall. Also, the jet shear layer thickness appears to be much smaller in the RANS simulations. Further downstream, the bending of the jets due to crossflow is also different in the RANS simulations, compared to experiment. This difference in crossflow between experiment and RANS can be highlighted by the jet trajectory behavior through flow visualization of PIV. Jets are assumed to be faster in the RANS simulations than in the experiment, and hence the jet bends less from the crossflow. This discrepancy accumulates in the RANS calculations, and fails to match the experimental trend for the last three jets.

Shear Layer Thickness

From Figure 71 it was found that the spreading of the jet shear layer is different for PIV, LES, and RSM calculations. The first jet in the channel does not have any impact of crossflow from the neighboring jets. Since the effect of crossflow is minimum, the velocity profiled obtained from the first will have the least amount of distortion. This jet was used for calculating the shear layer thickness very close to the orifice to see the variation in shear layer thickness (δ) predicted by experiment and simulations. The shear layer thickness was calculated based on the distance between transverse location along the streamwise direction where $U^* = 0.1$ and $U^* = 0.9$ where U^*

is the ratio of local velocity to the maximum local velocity at $z/D=2.75$. Figure 72 shows the shear layer thickness at $z/D=2.5$ for the first jet.

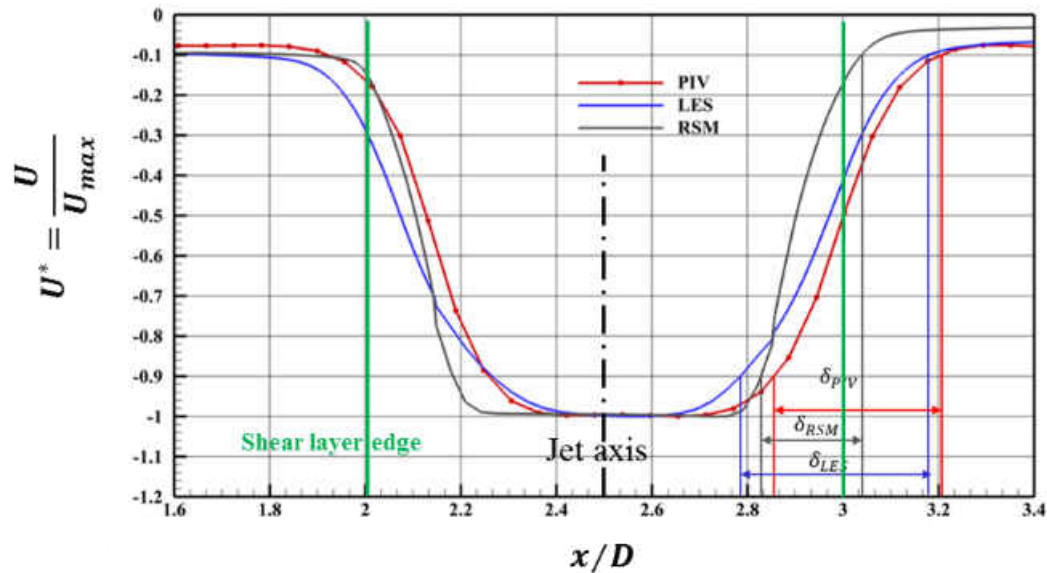


Figure 72 Jet shear layer thickness from PIV, LES, and RANS for the first jet

The shear layer thickness calculated from the velocity profile for PIV, LES, and RSM are $0.35D$, $0.39D$ and $0.21D$ respectively. From this calculation, it can be seen that PIV and LES show good agreement of predicting the jet shear layer thickness. Typical RANS models failed to predict the shear layer thickness; as a result, the velocity contour (in Figure 71) of the jets appears to be much thinner in RANS calculation.

Centerline Axial Velocity

Centerline jet velocity plays an important role determining stagnation point heat transfer in an impingement heat transfer problem. The wall-normal velocity component along the jet centerline can reveal information about the strength of the individual jet impinging onto a target surface.

Figure 73 shows the position of the center plane inside the channel and the location of the profiles (shown in red dotted lines) where the centerline jet velocities are extracted to gather information about the individual jets. Only the first three jet profiles were analyzed for this problem. As the crossflow accumulates and bends the jets downstream, the identity of the 4th and 5th jet diminishes. Hence the last two jets were not included in the discussion.

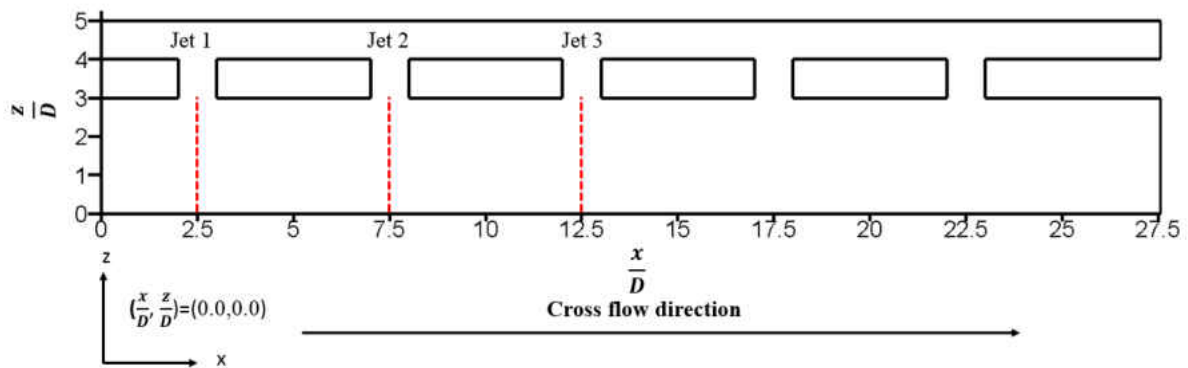


Figure 73 Centerline jet profile for the first three jets in the impingement channel

Figure 74 shows the mean axial velocity component along the wall-normal distance (z/D) on the geometric centerline of the first jet inside the channel. All jet velocity values are normalized by the centerline jet exit velocity of the individual jet, $v_{z_{max,local}}$.

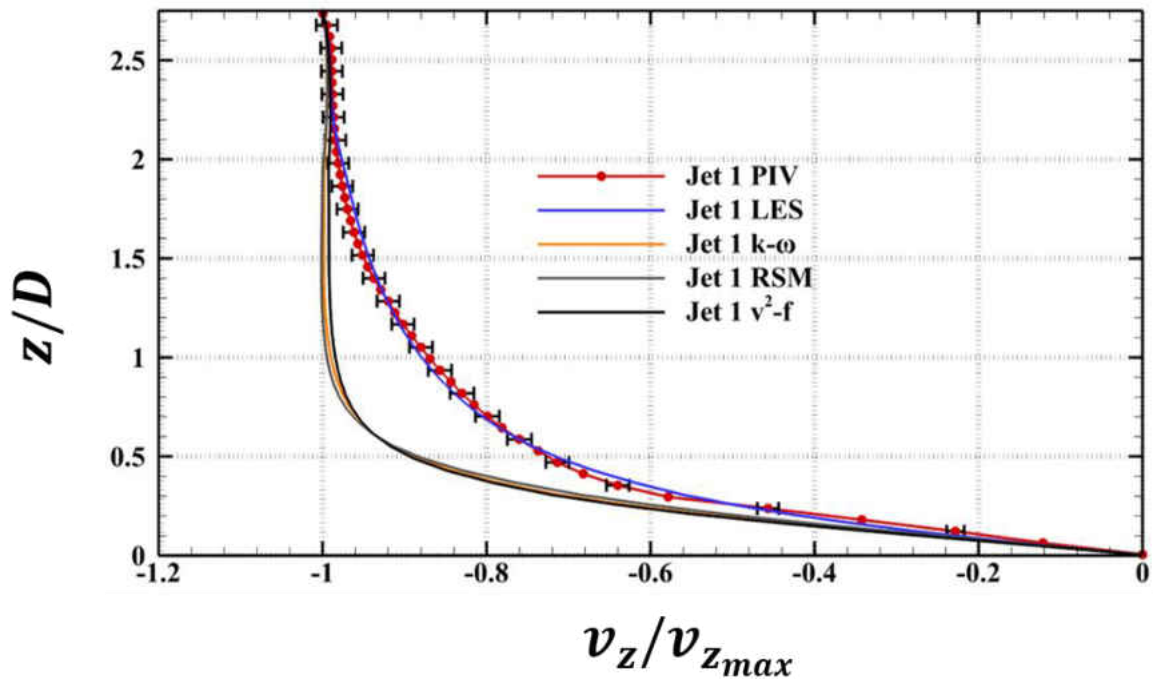


Figure 74 Axial mean velocity profile for the first jet

Since the crossflow has not taken any substantial effect on the first jet, the first jet can be treated as free impinging jet. Three different distinct region can be identified from the first jet velocity profile. These are: the potential core region, velocity decay region and the impingement wall jet region. The agreement between PIV and LES for the first jet centerline velocity profile is excellent, and both the profiles show very similar behavior. The potential core of the jet can be identified up to $z/D > 2$ for PIV and LES where the jet velocity remains constant in this region. Further downstream of the jet ($0.75 < z/D < 2$) the jet velocity starts to decay rapidly. Both PIV and LES shows good agreement in this region. Again further downstream of the velocity decay region, the jet appears to deaccelerate more rapidly, and the identity of the jet vanishes as it approaches the target wall.

A different jet behavior was observed for all of the RANS simulations for the first jet. The potential core of the jet appears to be very strong for the RANS simulations. With the length of the potential core extending up to $z/D > 1$ for all models. The decay region is also very small for the RANS calculations compared to PIV and LES. Predicting this stagnation point heat transfer is a very common problem for RANS models, as they generally over-predict. The difference in the jet velocity profile at the near-wall region helps explain the underlying reason for this discrepancy. The axial velocity profile shows higher near-wall velocities in RANS than to PIV, hence the jet impinges onto the target surface with higher momentum than in the actual experiment.

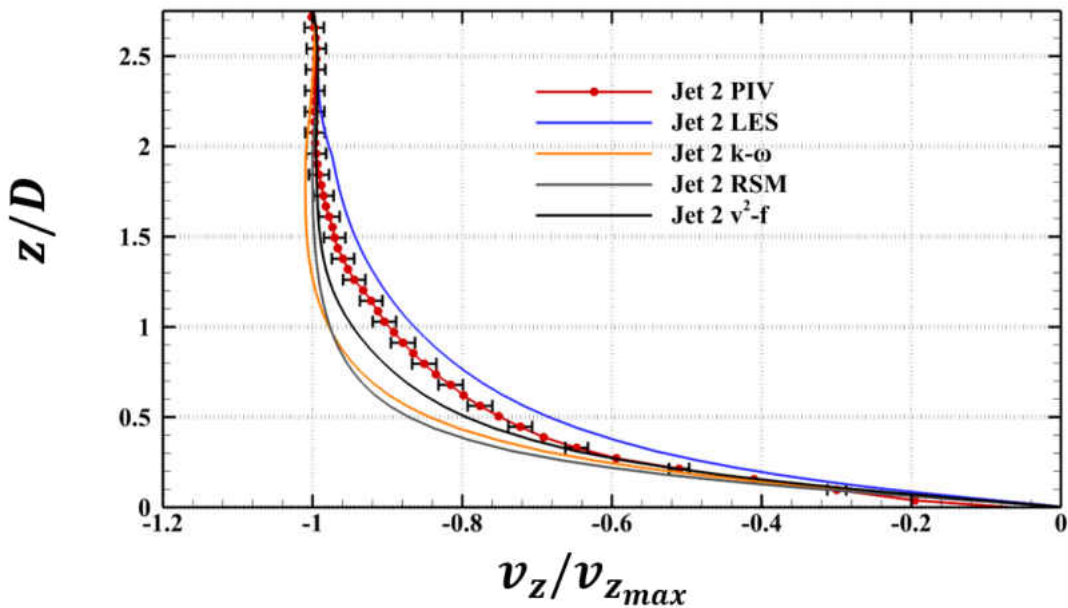


Figure 75 Axial mean velocity profile for the second jet

Mean axial velocity profiles for the second jet are presented in Figure 75. PIV and LES again, show reasonably good agreement for the second jet. Velocity profiles calculated from LES begin to deviate slightly from the PIV experiment after the potential core region. The velocity profile obtained from LES shows higher decaying rate than the profile calculated from PIV. The mismatch between the axial velocity profiles show the crossflow between the first jet and second jet are

different in LES and PIV. The potential core of the second jet is very similar to that of the first jet, which suggests that the cross-flow due to jet-to-jet interaction has not made a substantial impact on the second jet up to this region; the centerline profile of the first two jets remains similar $\sim z/D \sim 1.5$. The second jet profile starts to deviate from the first jet after this wall-normal location, however the upwash flow between the first and the second jets causes this deviation. Due to the shear caused by upwash of the wall jet and the axial velocity gradient, the flow slows down in the velocity decay region for the second jet. In all RANS simulations, the potential core prediction is different than the experiment even for the second jet. The length of the potential core extends to $z/D > 1.5$ for RANS where as in PIV this length is $\sim z/D > 2$.

Figure 76 shows the mean axial velocity profile of the third jet. All RANS models and LES predict reasonably well with the experimental data upto the potential core of the jet, $\sim z/D > 2$. From all the profiles, it is apparent that the third jet velocity, decays much faster than that of the first two jets. This is due to the crossflow accumulating from the previous two jets, causing higher shear, and turbulence in the flow field, hence the jet becomes weaker from $z/D < 2.0$.

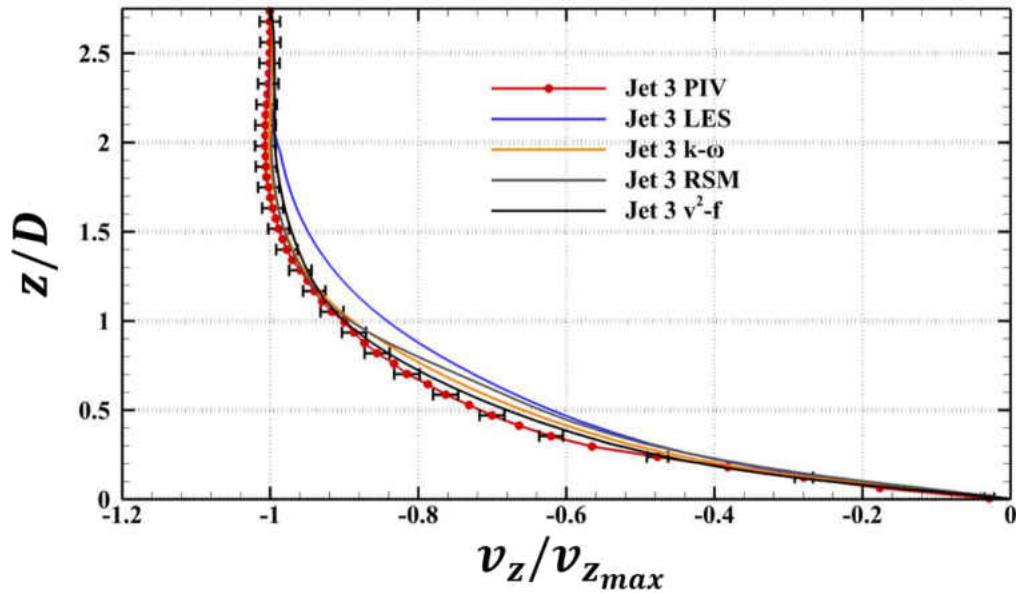


Figure 76 Axial mean velocity profile for the third jet

Streamwise Velocity Profiles

In order to quantify the accuracy of RANS and LES for predicting the streamwise velocity profiles, three axial locations were chosen ($x/D=10, 15, 20$). Figure 77 shows the location of the streamwise velocity profiles for comparison. Since the cross flow begins to take a more noticeable effect from second jet onwards inside the channel, and the fluid motion is primarily dominant in the wall normal direction prior to $x/D < 10$, these locations were chosen to be suitable for comparing with the PIV data. At each location for all models, the streamwise velocity components were non-dimensionalized by the streamwise velocity component value at $z/D=2.75$.

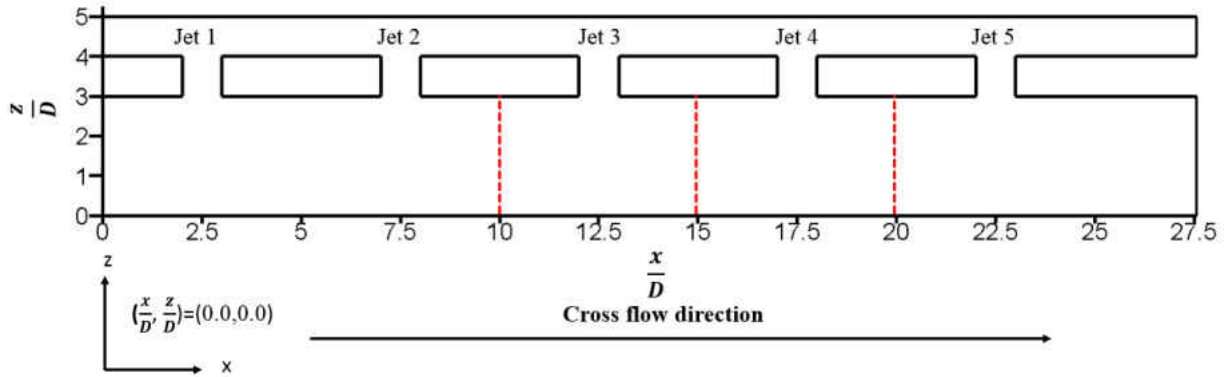


Figure 77 Streamwise velocity profile location (crossflow velocity)

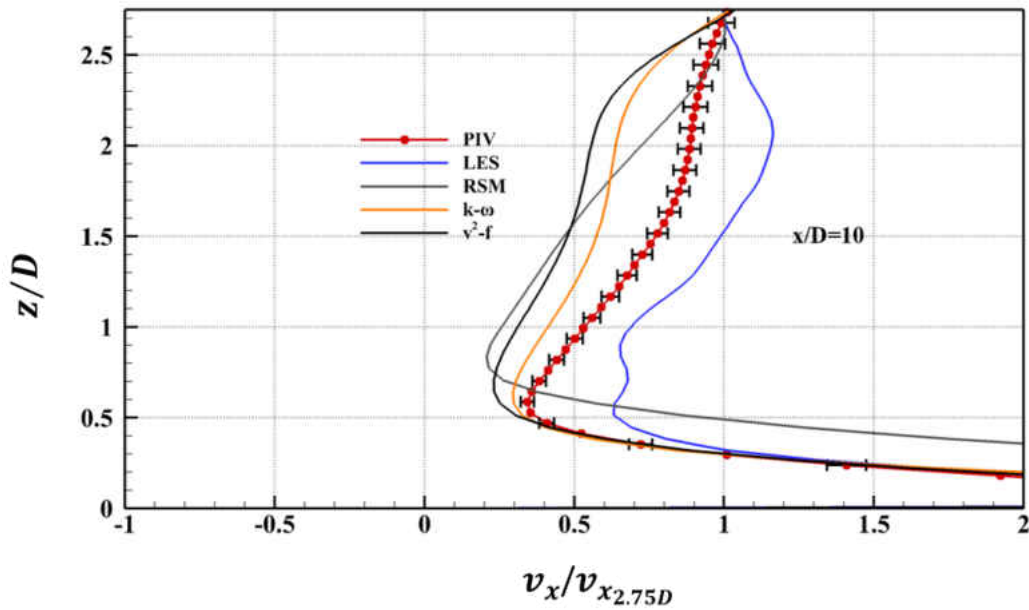


Figure 78 Streamwise velocity profile at $x/D=10$

Figure 78 shows the streamwise velocity profiles at an axial location of $x/D=10$. The profile calculated from LES shows reasonable agreement with PIV data near the wall jet region $\sim z/D < 0.5$. Discrepancies are seen between PIV and LES in the region ($z/D > 0.5$). The trend of the crossflow velocity profile exhibits similar behavior from PIV and LES. RANS is found to exhibit a completely different profile than PIV however. This highlights RANS inability to predict this flow

field accurately in both axial and streamwise components for locations $< x/D=10$. The magnitude of crossflow velocity predicted in RANS, is much lower than that of the experiment; this suggests the crossflow does not have enough momentum to bend the jets, as is seen in the experiment and LES. This helps to explain the observation that the extent of potential core is larger in RANS simulations for the first two jets, based on the previously discussed mean axial velocity profiles.

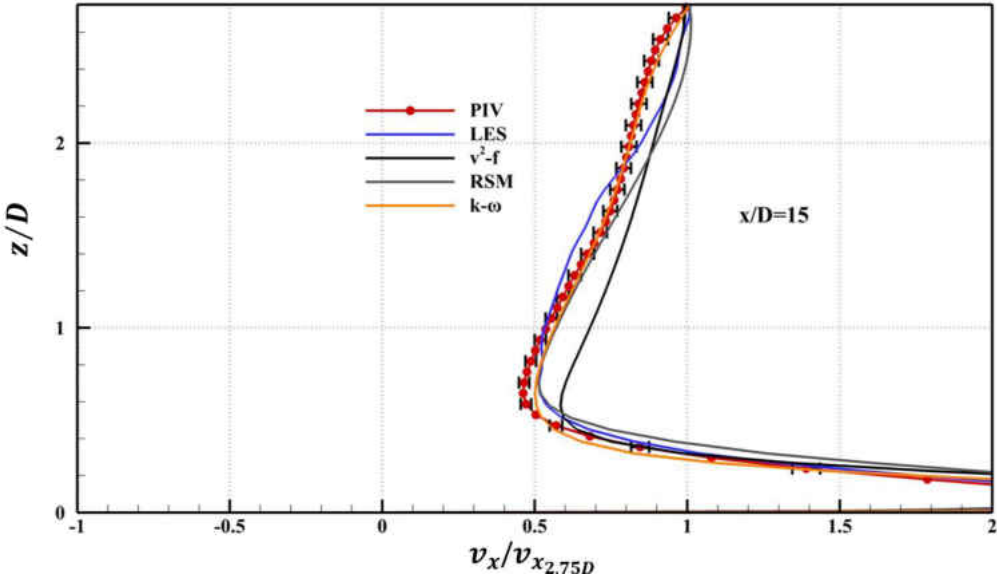


Figure 79 Streamwise velocity profile at $x/D=15$

Figure 79 shows streamwise velocity profiles at location $x/D=15$. It is interesting to note that at this location all RANS models agree well with the experiment, even though they failed to predict the axial velocity profiles at $x/D=10$.

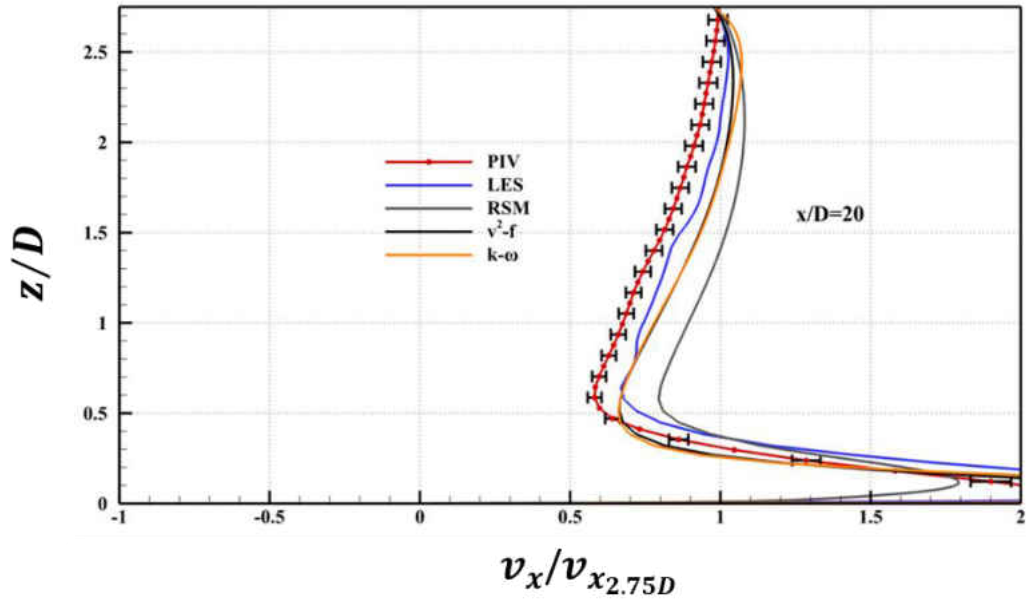


Figure 80 Streamwise velocity profile at $x/D=20$

Figure 80 shows streamwise velocity profiles at location $x/D=20$. All RANS and LES models agreed reasonably well with the experimental data, with the exception of the RSM model which very slightly overpredicts.

Mean Axial Velocity Profile at Different Wall Normal Distance

Mean axial velocity profiles at different wall normal distance were taken along the centerline plane of the channel. Figure 81 presents the axial velocity profiles in the streamwise direction for the entire channel at the $z/D=2.5$ location. All velocities were normalized by the maximum streamwise velocity magnitude along that line. To get a better understanding of the individual jet profile and their behavior, Figure 81 was split into five sections with a constant $5D$ axial spacing as shown in Figure 82 (a,b,c,d,e). Since all the RANS models exhibit similar behavior in predicting the axial

velocity profile, only the SST $k - \omega$ turbulence model was used to compare with the experimental data.

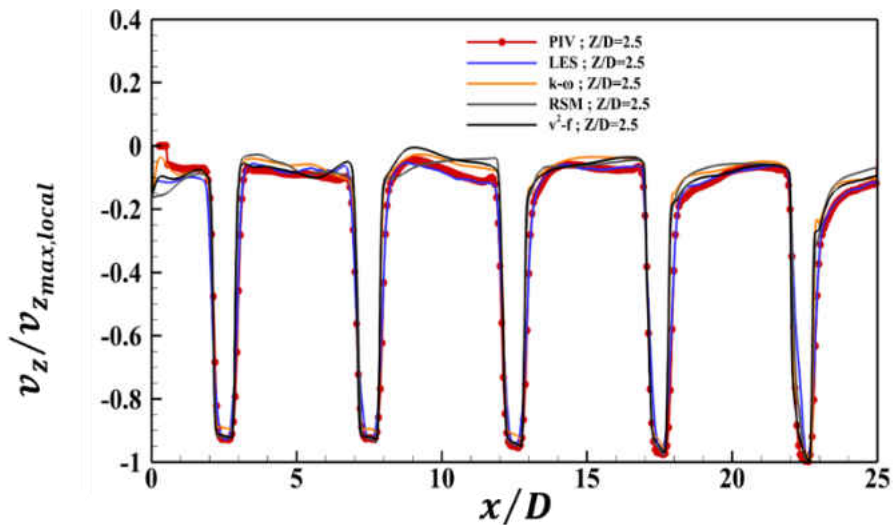


Figure 81 Axial velocity profile of v_z at $z/d=2.5$

From Figure 82 it can be seen that data obtained from PIV and LES are in excellent agreement for the majority of the profiles. The thin shear layer near the jet edges, and the width of the jet shear layer are accurately predicted by LES when compared to the PIV data. The axial velocity profile exiting from the jet orifice will propagate downstream towards the target wall and is responsible for the mixing and heat transfer on the target wall for the jet impingement problem. Hence for any numerical model, predicting the inlet velocity profile after the jet orifice is crucial for accurate prediction of heat transfer. From Figure 82 (a, c, e) it is clear that RANS failed to predict the axial velocity gradient in the jet shear layer for all the jets. Particularly of note, is the characteristic ‘top-hat’ profile which exists for the RANS predictions, in contrast to that predicted by LES, and measured by PIV. Figure 83 shows the axial velocity profile of v_z at $z/d=0.50$ above impingement

target plate. The distortion of the jet profile and creation of the wall jet and upwash due to crossflow can be identified from this profile.

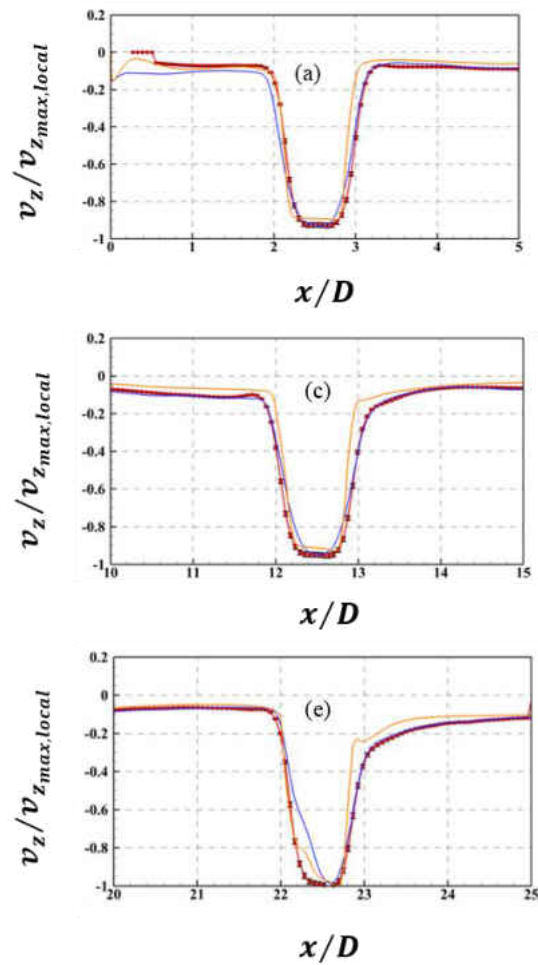


Figure 82 Axial velocity profile in the streamwise direction for $z/D=2.5$

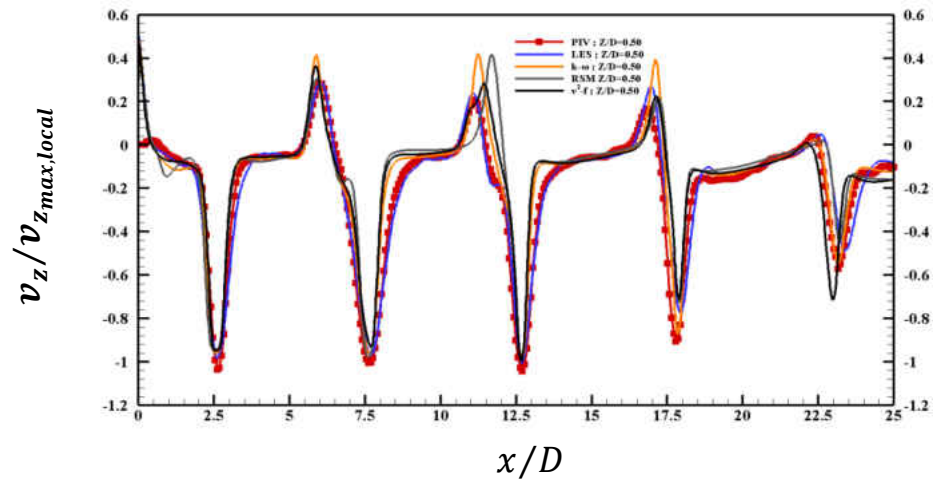


Figure 83 Mean axial velocity profile in the streamwise direction for $z/D=0.5$

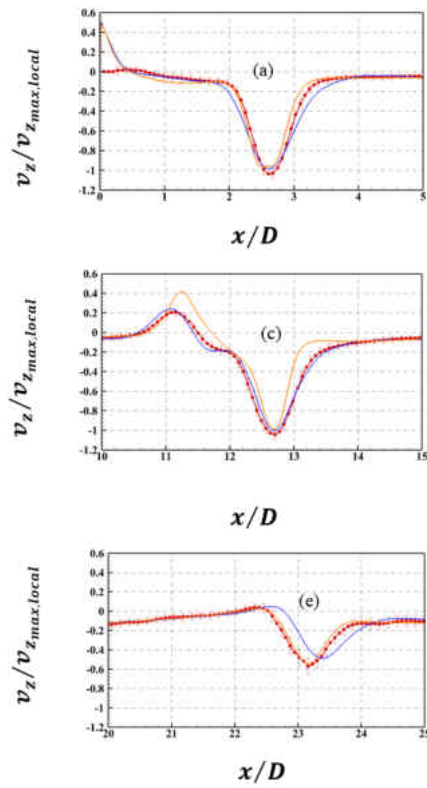


Figure 84 Axial velocity profile in the streamwise direction for $z/D=0.5$

Figure 83 shows the axial velocity profiles zoomed on, similar to that of Figure 81 ($z/D=0.50$). Both the LES and RANS shows a recirculation zone at $x/D < 1$. This recirculation zone was created due the presence of an end cap wall before the first jet. As the first jet approaches to the target wall, the flow interaction between the end cap and wall jet produce the recirculation zone. In the PIV, it was challenging to get data very close to the end cap wall due to reflections, hence the discrepancy between the experiment and numerical model can be understood near that region. Predicting the upwash flow by the numerical model is important because this flow eventually determines the heat transfer in between jets. The upwash flow created by the jet-to-jet interaction, and the wall jet collision can be identified by looking at the velocity profile from Figure 84. The change in the sign of the velocity profile indicates the upwash between jets. LES was able to predict the upwash accurately with the experiment for the first four jets. The location and magnitude of the upwash were not predicted well by RANS as shown in Figure 84 (c).

Jet Dynamics

Numerous studies have been performed on single jet impingement heat transfer. In the current study focus has been made on an impingement problem where flow, turbulence, instability and heat transfer can be connected. The heat transfer behavior depends on jet velocity, jet to target wall distance, shape of the nozzle, turbulence level, and entrainment conditions [27]. Jambunathan et al. [90] compiled a review of heat transfer data for a single round jet impingement. The authors [90] concluded that heat transfer correlations do not account for the effect of turbulence generated from the nozzle orifice. The study reveals that details of the nozzle geometry and the turbulence intensity at the nozzle exit are required to obtain a better understating knowledge on heat transfer.

Royne and Christopher [91] investigated the effect of nozzle geometry for jet impingement heat transfer problem. However, no turbulence data was reported in the results. Four different types of nozzle configurations were used in the experiment. Baughn et al. [92] studied the effect of ambient air entrainment into a heated impingement plate. The boundary conditions were clearly defined in the experiment. A long pipe ($72D$) was used to ensure fully developed turbulent velocity profile as inlet condition. Uniform heat flux was supplied at the target wall by electrical heating. The surface temperature was measured using a liquid crystal. This particular experimental result is considered as a benchmark test case to validate turbulence model for impingement heat transfer problem by ERCOFTAC [93]. Baughn et al. [92] studied heat transfer for different jet to target plate distance.

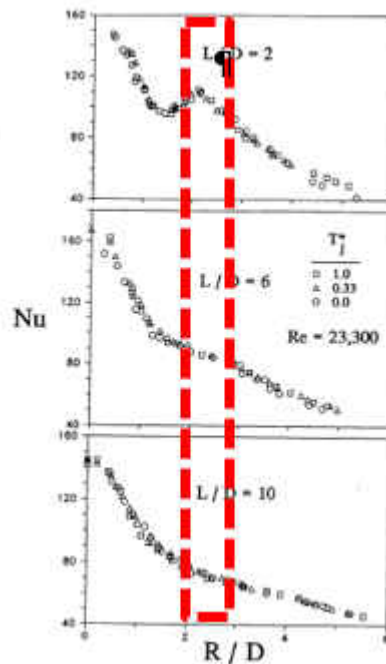


Figure 85 Heat transfer distribution for different jet to target wall distance [92]

From Figure 85 it is obvious that heat transfer is highest at the stagnation region. After the stagnation region, the heat transfer is expected to decrease. For $L/D=2$ (target plate to jet plate separation distance) a peculiar behavior of heat transfer was observed where a secondary peak in the heat transfer was noticed around $r/D \sim 2.2$ (also highlighted by red dotted lines). This behavior of heat transfer was inconsistent for $L/D > 2$. Uddin [94] performed large eddy simulation (LES) technique using the same boundary condition described in [92]. The numerical model used in [94] was able to predict the secondary peak accurately whereas the current state of the RANS model failed to predict the secondary peak in the heat transfer distribution. Donavon and Murray [95] studied the heat transfer distribution on a flat plate for different jet to target wall distance (0.5-8D) for a range of Reynolds numbers (10,000-30,000). They concluded that the secondary peak is observed for < 2 jet diameters. The study suggested that secondary peaks are due to an abrupt increase in turbulence in the wall jet region. Uddin [94] in his study summarizes the different interpretations for this secondary peak event in heat transfer. It is interesting to observe that there has not been any agreement on the physical interpretation of the secondary peak from different authors. Webb [96] attributed the reason of the secondary peak to a higher level turbulence in the boundary layer due to flow acceleration and intense shear. Behnia et al. [97] also provided a similar explanation. Viskanta [98] attributed the secondary peak to large scale toroidal structure created at the location on the target wall. Angeioletti et al [99] tested simultaneous visualization of the flow field using PIV and heat transfer for impinging jet configurations. The jet Reynolds number studied in the experiment was fairly low 1000-1500. The author noticed the secondary peak in heat transfer existed even at small Reynolds number for the small jet to target wall distance. From the flow visualization, it was concluded that the influence of coherent structures at the target wall

creating the non-uniformity in heat transfer. For higher jet to target wall distance these coherent structures were not observed in their flow visualizations study. The PIV image supports the argument in non-uniform heat transfer distribution in their results. Popiel and Trass [100] used a smoke-wire flow visualization technique to gain a deeper insight to understand the vortex structure of the impinging jet and the wall jet. The experiments were performed at high Reynolds numbers (10000-20000). The main objective of the study was to illustrate the behavior of natural free impinging jets at low separation distance. The study [100] depicts a clear view of vortex formation near the jet orifice.



Figure 86 Vortex formation in jet impingement and effect on heat transfer [100], [95]

If no external force is applied i.e., if the jet is natural, the first vortex will occur at a particular frequency called as the fundamental frequency of the jet. The vortex structures are termed as the eddies or scales of the jet. These eddies are repetitive in nature and remains coherent as the jet continues to grow downstream hence these are called the coherent structures of the flow. As the jet continues to grow these vortices merged together and the phenomenon is called vortex pairing. After the stagnation region, the boundary layer grows radially due to the presence of target wall, and the wall jet region is formed. This wall jet region is also dominated by shear layer. In the wall jet region the turbulence level is higher than the typical boundary layer on a flat plate because of

higher velocity gradient. The jet shear layer near the orifice is initially formed by Kelvin-Helmholtz instability mechanism. This particular instability occurs due to velocity different or density gradient between two fluids. For jet impingement problem, the onset of Kelvin-Helmholtz instability occurs due high velocity fluid issuing out from the jet orifice but surrounding fluid velocity is very small compared to jet velocity and hence the shear layer is formed. The small disturbance in the jet shear layer triggers the Kelvin-Helmholtz instability and the instability continues to grow exponentially. opiel and Olev [100] interpreted from their flow visualization of wall jets that these eddies are responsible for the secondary peak in heat transfer. Another way to explain their results are, the eddies pick up the heat from the heated wall carries the heat with higher momentum and result in a better mixing

Fourier transform of the pressure signals was used to understand the structural content of the flow. Several point probes were created inside the computational domain for this purpose. The point probes are located inside the jet core, jet shear layer, impingement area and inside the wall jet region. The time history of the pressure signal was recorded along these points from the beginning of the simulation. The dynamics of the flow can be analyzed by the power spectrum analysis from these single point measurements. These techniques are useful to find the natural frequencies of the jets. Liu & Sullivan [101] found the natural frequency of an impinging jet is the same for a free jet. Tsubokura et al. [102] also reported that the natural frequency of an impinging jet corresponds to a Strouhal number of 0.37.

The power spectral density of static pressure at different locations were calculated inside the channel. Figure 87 shows the location of the point in the jet shear layer for the first four jets.

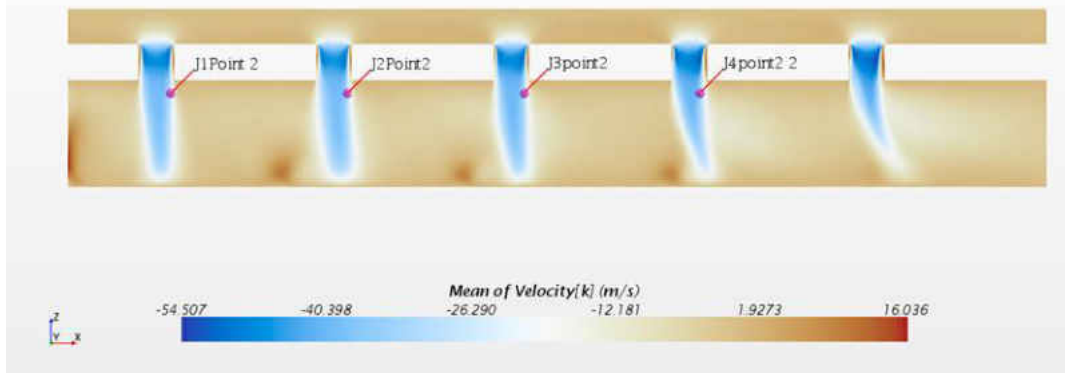


Figure 87 Locations for power spectral density in the jet shear layer

The frequency of the pressure signals are presented in the non-dimensional form called Strouhal number. The Strouhal number for the current study is defined as:

$$St = \frac{f \cdot D}{U_{jet}} \quad (64)$$

Where U_{jet} the jet exit velocity and D is is the jet diameter.

Figure 88 shows the power spectral density calculation at the jet shear location for all the jets. Two dominant frequencies can be observed at the jet shear layer for each jet. The Strouhal number of these frequencies are 0.64 and 1.36. Donovan and Murry [103] found three dominant peaks in the jet shear layer for a single round jet experiment. Schadow and Gutmark [104] reported similar frequencies at the exit of the jet. The highest frequency was attributed to a process called vortex roll up in the shear layer and the lowest frequency was attributed to a process called vortex merging [103]. The Strouhal number for these three peaks were approximately: 0.6, 1.1 and 1.6. The higher frequency can be attributed to a process called vortex roll up and the low frequencies can be attributed to a process vortex pairing. Han and Goldstein [105] found two peaks in the velocity spectra. The higher frequency was attributed to the vortex roll-up or passing frequency of the vortex. The lower frequency was attributed to vortex pairing.

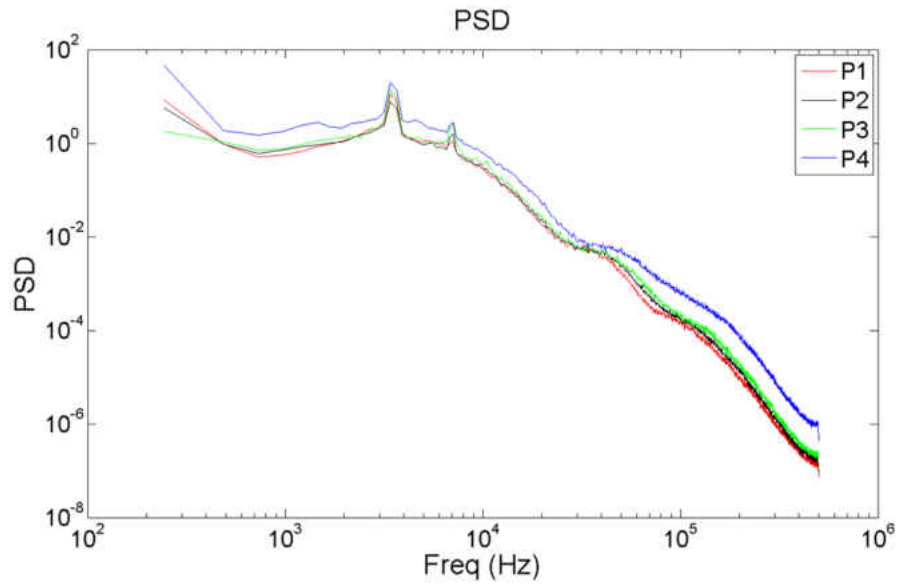


Figure 88 Power Spectral Density in the jet shear layer

The power spectra at the centerline of the jets are also calculated to find if there is any dominant frequency inside the jet potential core. Figure 89 shows the point probe locations where these values were calculated.

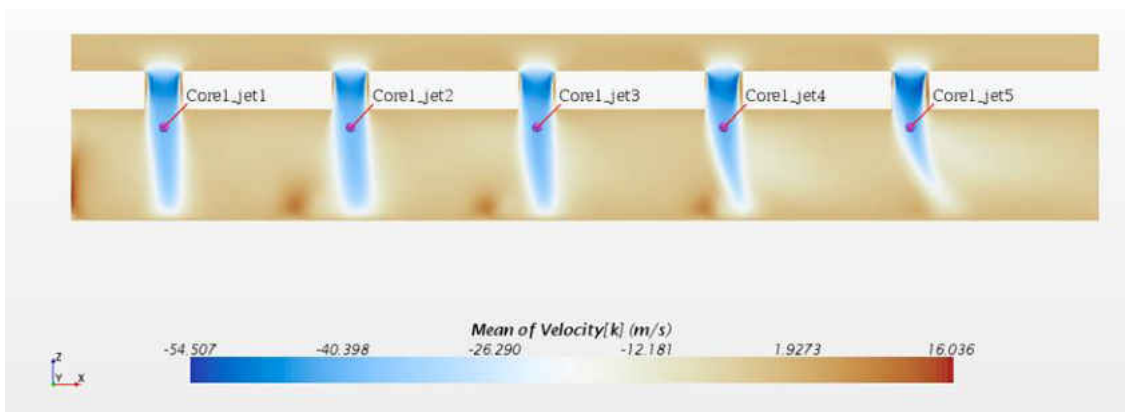


Figure 89 Point probe location in the potential core

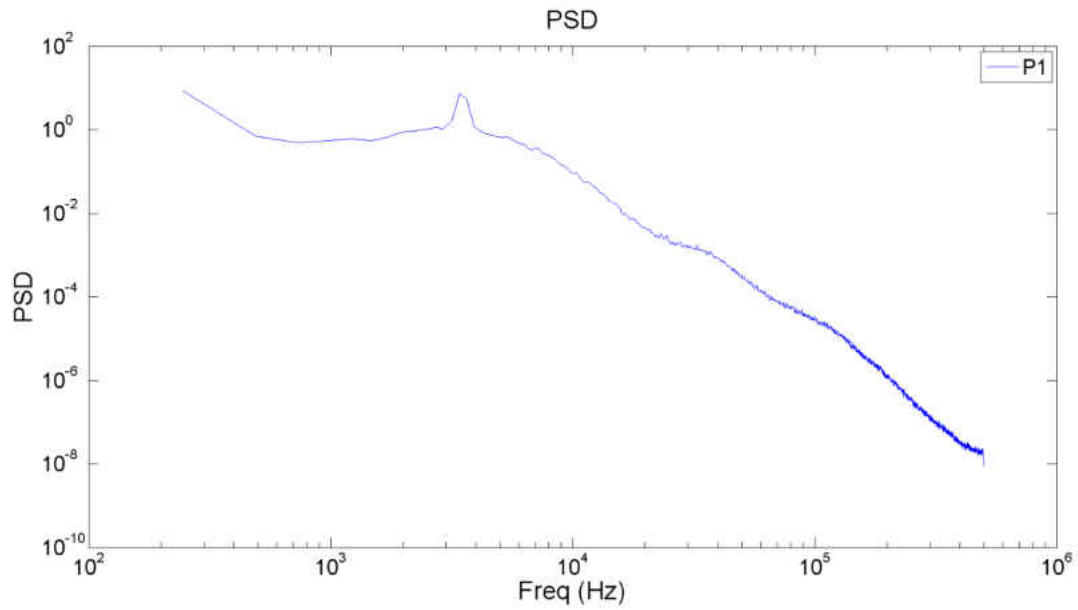


Figure 90 PSD inside the jet potential core

Power spectral density was calculated inside the jet potential core as shown in Figure 89. Figure 90 shows the power spectral density at the jet centerline inside the potential core. It is interesting to note that the same dominant frequency corresponding to Strouhal number of 0.64. Further downstream at the fifth jet, another point in the jet shear layer was where crossflow is strong and the jet is bending. The location of the point probe is shown in Figure 91

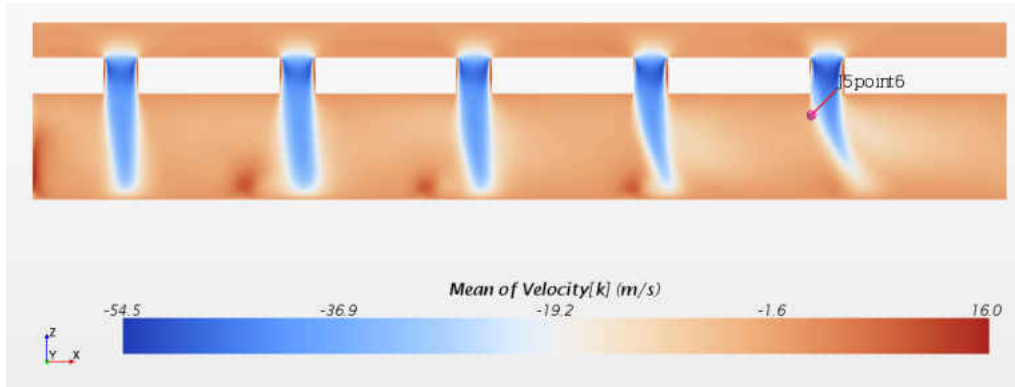


Figure 91 Point probe location in the 5th jet

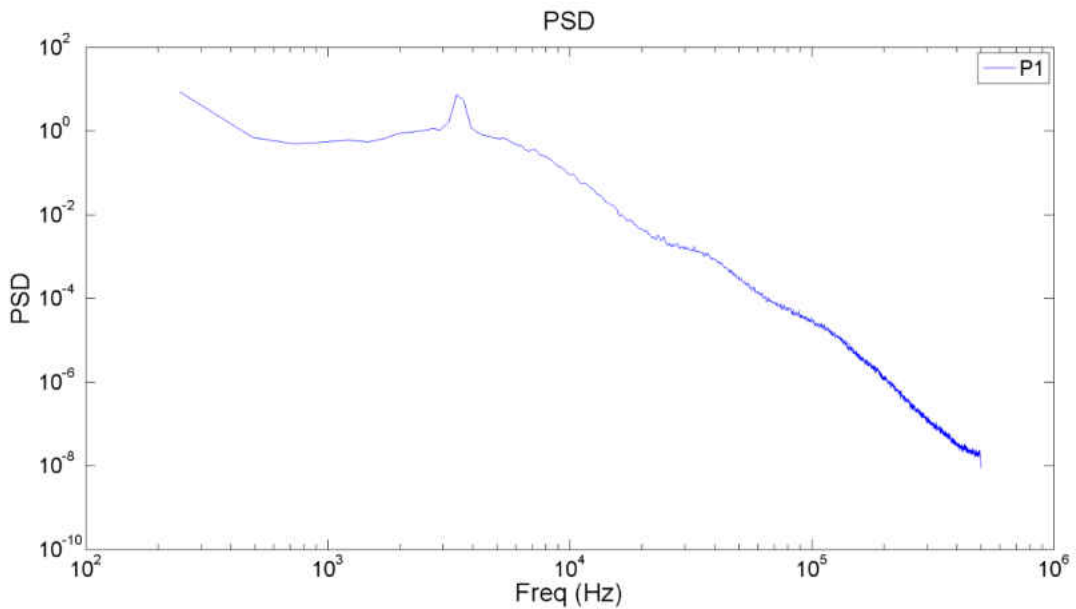


Figure 92 Power Spectral Density for the fifth jet

Figure 92 shows the PSD calculated from the pressure fluctuation data on the probe. Only one dominant frequency is observed at this location. Unlike the other shear layers among different jets the second dominant frequency corresponding to $St=1.36$. The absence of this second dominant frequency at this location is due to the strong crossflow preventing the formation of vortex pairing. Power spectrum was calculated close the wall for different locations in the crossflow direction.

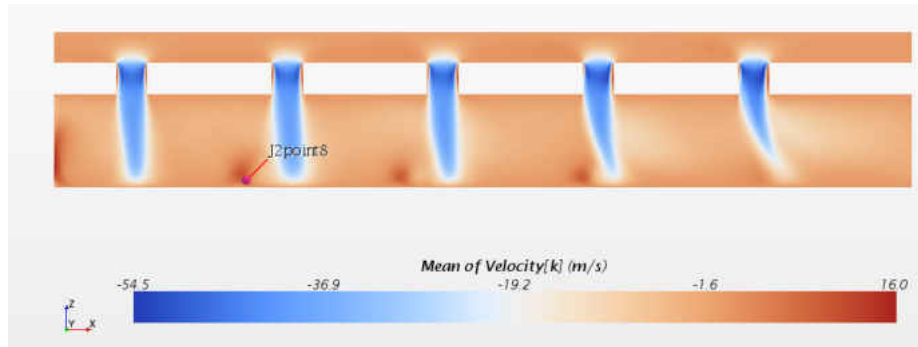


Figure 93 Point probe location near wall jet
PSD

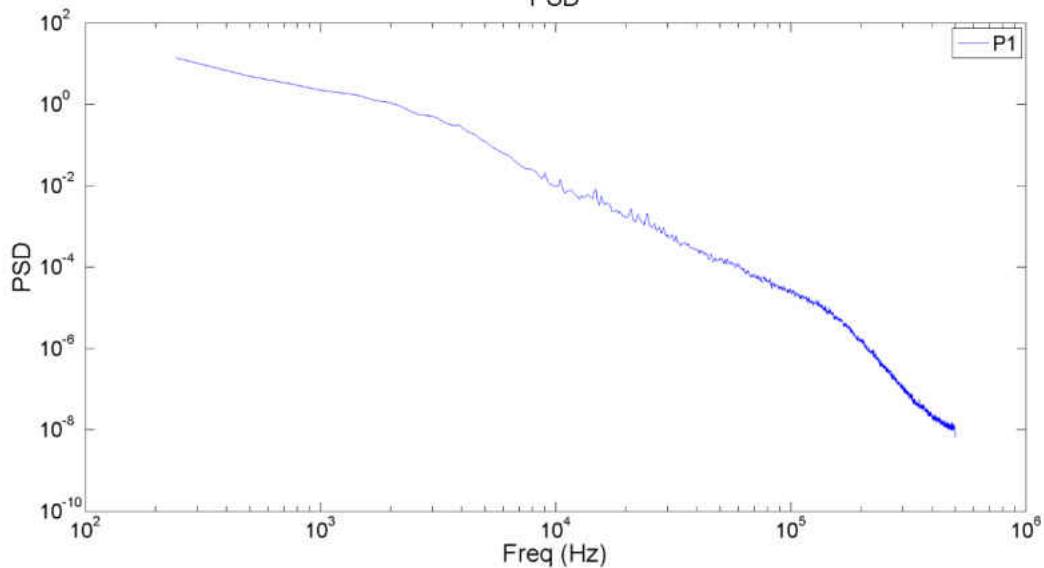


Figure 94 PSD near wall region

The slope of the power spectra can determine if the turbulent scales are resolved or not. The slope of the power spectrum indicated by the straight line in Figure 94 is $-5/3$ which agrees well with the well-known characteristics of turbulence spectrum. Figure 93 shows the point probe location in the wall jet zone and close to stagnation point. Nishino et al [106] reported that the flow near stagnation point is isotropic in nature. The turbulence spectrum in Figure 94 shows that flow is isotropic in nature which confirms the similar findings from the previous study by Nishino et al. [106] and Uddin et al. [94].

The natural frequency of the jet was found to be different than the other single jet impingement study. In the experimental work by Liu and Sullivan [101] the natural frequency of the jet was concluded to be $St=1.23$. The jet Reynolds number in that study was 12,300. In the study by Chiriac and Ortega [107] the natural frequency was found to be corresponding to a $St=1.1$. The jet Reynolds number was 750. Hallquist [108] reported that the jet natural frequency increases with jet Reynolds number. In their study the natural frequency of the jet was found to be corresponding to a Strouhal number of 1.5. The findings of the jet natural frequency are summarized in Table 11

Table 11 Jet Impingement Natural Frequency

Authors	Study type	Jet Reynolds Number	Strouhal Number
Chiriac and Ortega [107]	Numerical Work	750	1.1
Liu & Sullivan [101]	Experimental Work	12,300	1.23
Current Study	Numerical Work	15,000	1.36
Hallqvist [108]	Numerical Work	20,000	1.4

Turbulent Statistics

Flow Anisotropy

Turbulent statistics are useful tool to understand the flow anisotropy. Typically in an array impingement problem, the first few jets behaves like a regular impinging jet. Past this, the flow acts like a jet in a cross flow, thus in an impingement channel, the flow is expected to be anisotropic in nature. Only the first jet was selected inside the channel as a representative of the entire channel to describe the anisotropy of the flow field. Two axial locations on the first jet were chosen to show the flow anisotropy. Figure 95 depicts the locations on the first jet where the Reynolds normal stresses are calculated from PIV, LES, and RSM.

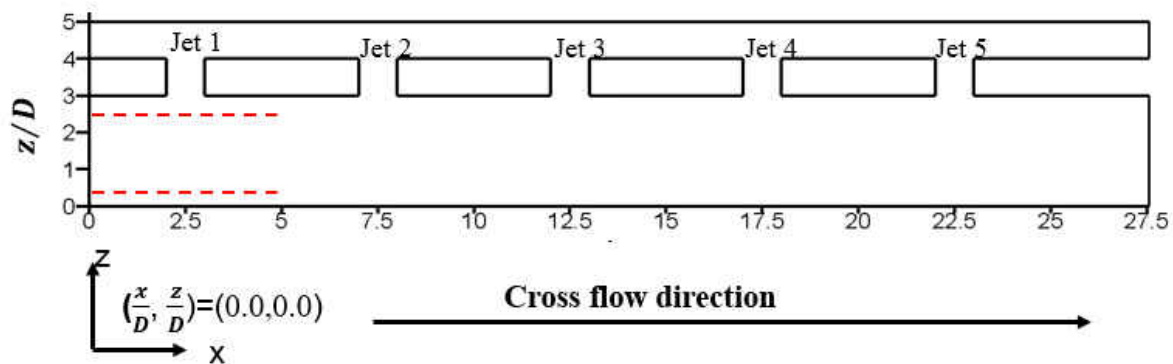


Figure 95 Location of the Reynolds normal stresses

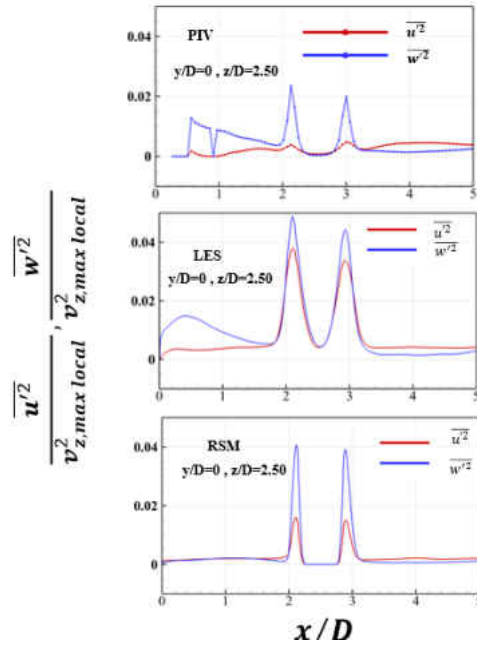


Figure 96 Flow field anisotropy at two different axial location for the first jet ($z/D=2.50$)

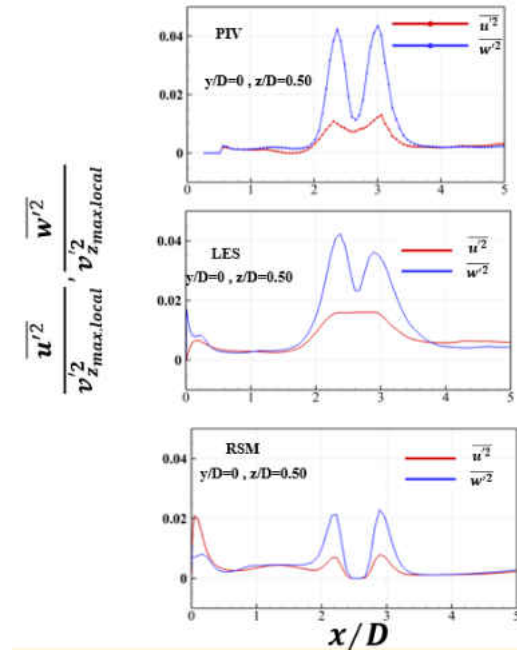


Figure 97 Flow field anisotropy at two different axial location for the first jet ($z/D=0.25$)

Figure 96 shows the Reynolds normal stresses ($\overline{u'^2}$, $\overline{v'^2}$, $\overline{w'^2}$) at $z/D=2.5$ channel height and Figure 97 shows the Reynolds normal stress at $z/D=0.5$ channel height at the centerline plane of the channel. The normal stresses are normalized by the square of maximum axial local velocity of jet1 at $z/D=2.5$. The two-component PIV data shows variations for Reynolds normal stresses ($\overline{u'^2}$, $\overline{w'^2}$) for both locations. The out of plane component ($\overline{v'^2}$) was not possible to measure and was not estimated in the PIV data. To keep the numerical comparison consistent $\overline{v'^2}$ component was excluded in Figure 96 and Figure 97. Close to the jet orifice, $z/D=2.5$ Figure 96, the flow is expected to be anisotropic at the jet shear location at $\sim x/D=2.5$ and $\sim x/D=3.0$. PIV, LES, and RSM shows anisotropy at the jet shear layer location for the Reynolds stress components. Very close to the target wall ($z/D=0.5$) the anisotropic behavior of the flow expected to be more evident than close to the jet orifice. At this location, jet impinges, flow turns, and wall jet develops. These events cause the velocity gradient in the flow to be more inhomogeneous in all directions. Again Figure 97 shows flow is highly anisotropic through the variation of Reynolds normal stresses in the experiment and the CFD.

Turbulent Kinetic Energy profile

Since the flow inside the channel is anisotropic, to get a better comparison among PIV, LES, and RSM the out of plane component velocity (v') was not included in the numerical calculation of the turbulent kinetic energy. Hence for all the methods, the turbulent kinetic energy (k) was calculated using $\frac{1}{2}(\overline{u'^2} + \overline{w'^2})$. A location very close to the jet orifice and close to the target wall ($z/D=0.5$) was selected for the comparison of the turbulent kinetic energy as shown in Figure 98. All the profiles

were non-dimensionalized by the maximum local velocity of the individual jets at $z/D=2.75$ channel height.

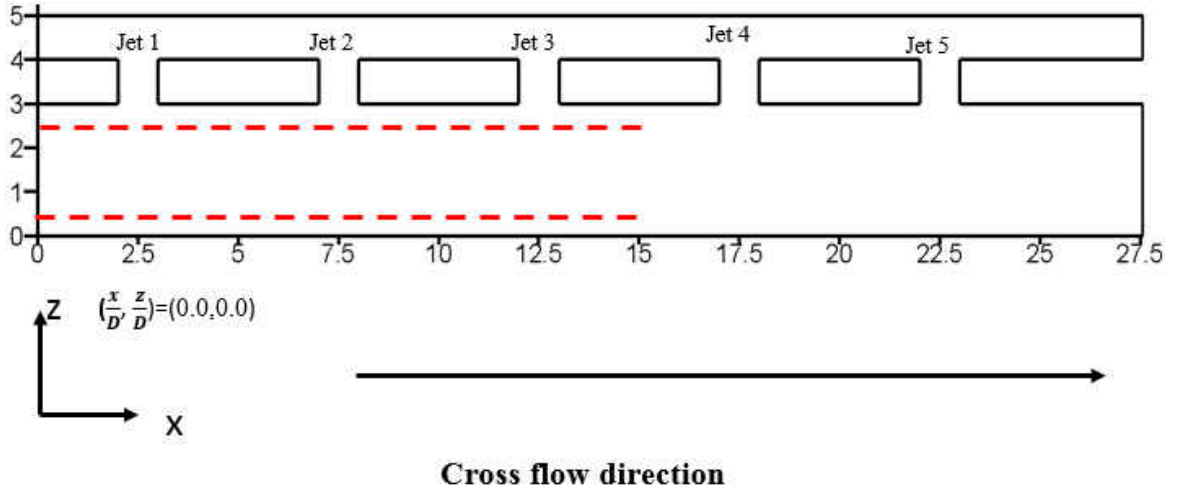


Figure 98 Locations for turbulent kinetic energy profile comparison

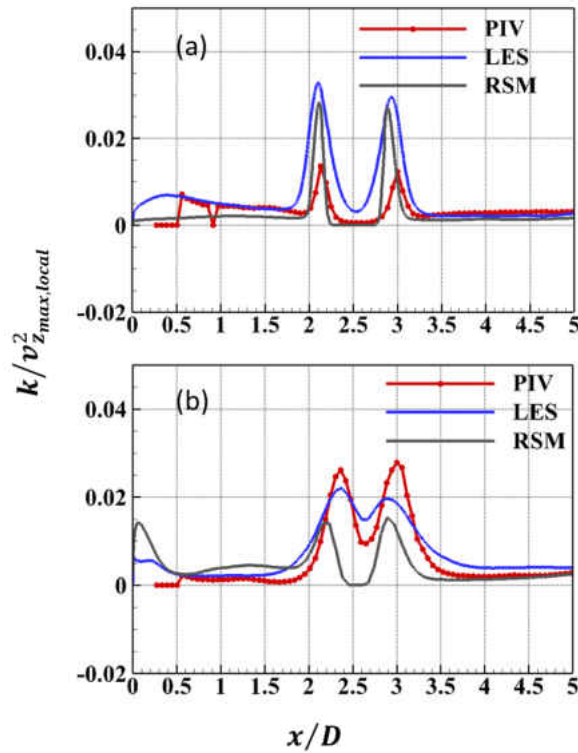


Figure 99 Turbulent kinetic profile at different channel height for individual jets

Figure 99 (a-b) shows the turbulent kinetic energy profile obtained from the experiment and numerical simulations at $z/D=2.75$. Even though the profiles calculated from the simulations are similar to that of the experiment, the difference in magnitude was observed between the experiment and the simulations at $z/D=2.5$.

Figure 99 (b) shows the turbulent kinetic energy profile comparison very close to the target wall. PIV and LES show good agreement along this axial location. The kinetic energy profile along the jet shear layer at this location has broadened than close to the orifice location ($z/d=2.5$), shows the jet is approaching the target wall, and the jet shear layer is thickening due to entrainment from the neighboring jet. Figure 99 (b) a show a peak in turbulent kinetic energy at $x/D \sim 2.2$ and $x/D \sim 3$. This is due to the presence of a wall jet recirculation zone created by a wall jet collision.

Turbulent Shear Stress Profile

The turbulent shear stress is the cause of transport and mixing in turbulent flow. Variation of the turbulent shear stress along the jet centerline would provide information on the jet behavior. In general, the Reynolds stress terms play a crucial role in turbulent production hence the profiles of the shear stress will shed insight about the mixing and shear in the domain of interest. Figure 100 shows the location where turbulent shear stress profile are plotted. All the profiles were non-dimensionalized by the maximum local velocity of the individual jets at $z/D=2.75$ channel height. Turbulent shear stresses from PIV, LES and RSM are compared along the jet centerline for the first three jets. These are shown in Figure 101-103. PIV and LES show excellent agreement for all three jets. RSM shows the poor capability of predicting the Reynolds stress component. The mean velocity characteristics along these jets were compared in the “Centerline Axial Jet Velocity”

section of the paper. The prediction of mean velocity gradient along the jet centerline was not captured well by RSM. As the turbulence shear stress generates from the mean velocity gradient, it is important for turbulence model to predict the mean flow behavior of the flow. The inability of predicting mean quantities by RSM is also reflected in the shear stress profile by RSM. As the jet propagates downstream a rise in shear stress up to $z/D > 0.5$ is noticeable for all the jets. This gradual increase in shear stress suggests that there is a continuous increase in momentum flux along the jet centerline. Initially, along this line the w' is responsible for driving the momentum flux. The increment in shear stress also indicates that the mean jet velocity is decaying along this direction. After $z/D < 0.5$ a decrease in momentum flux is observed which suggests that w' fluctuation is carrying high momentum fluid away from the jet centerline, and u' component is gaining a momentum in the streamwise direction with the development of wall jet.

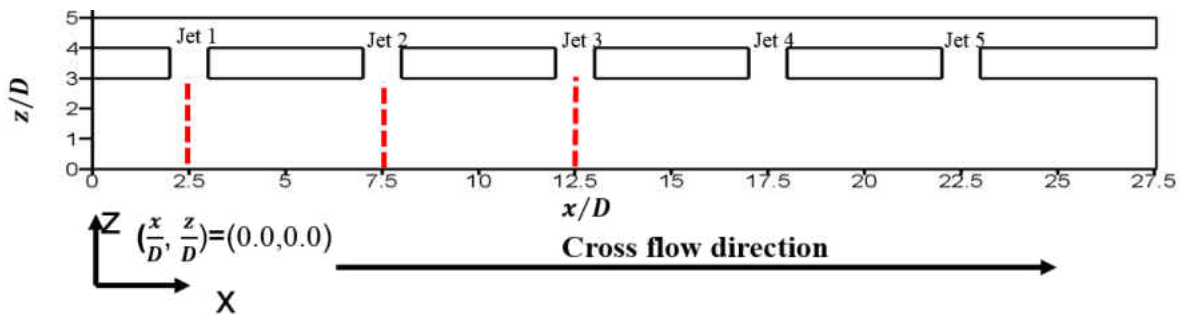


Figure 100 Turbulent shear stress profile along the jet centerline

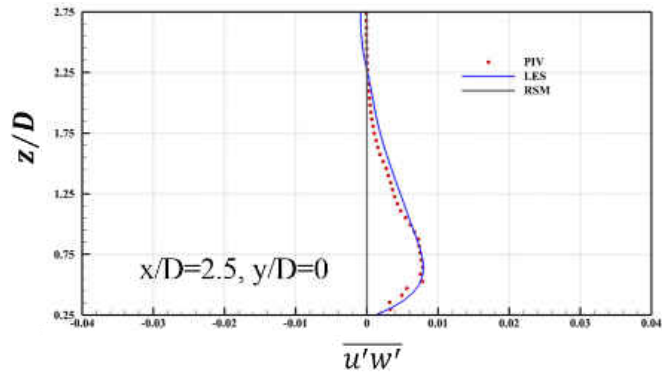


Figure 101 Turbulent shear stress profile along the centerline (First jet)

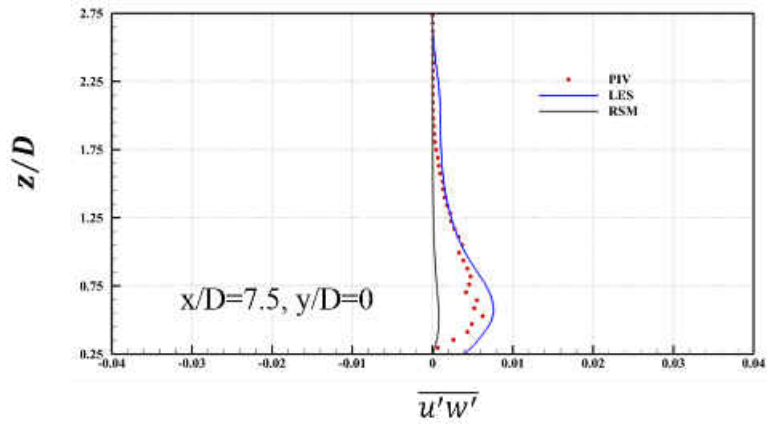


Figure 102 Turbulent shear stress profile along the centerline (Second jet)

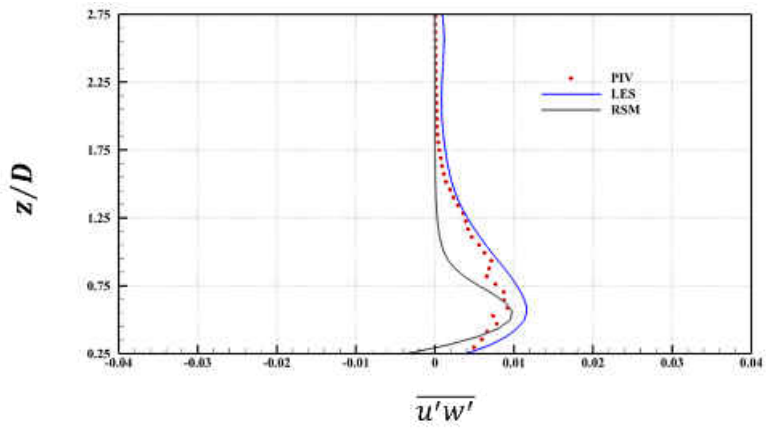


Figure 103 Turbulent shear stress profile along the centerline (Third jet)

Reynolds shear stress components very close to the target wall was extracted for comparison at $z/D=0.5$. The location of is shown in Figure 104.

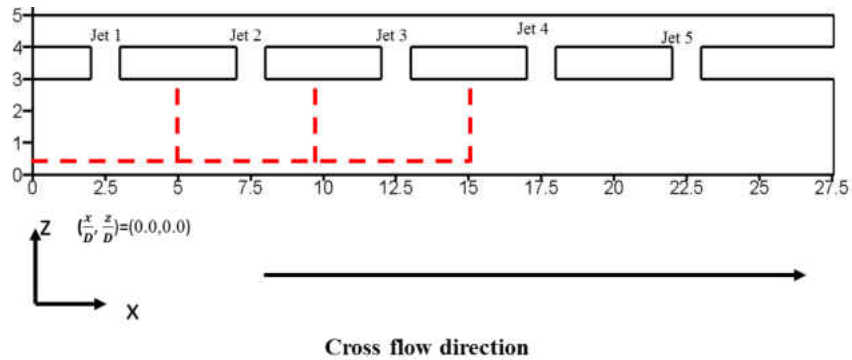


Figure 104 Shear stress profile location close to the target wall

The shear stress components are normalized by the square of the maximum local jet velocity at $z/D=2.5$ for each jet. The magnitude and profile of turbulent shear stress between PIV and LES are very similar for the first three jets. For the first jet Figure 105 a symmetric profile of shear stress is observed on the jet centerline at $x/D=2.5$. The change in “sign” of shear stress profile indicates two opposite flow directions. In Figure 106 , two similar profiles (where the shear stress changes its sign) are observed in the region between $x/D=5-10$. One is at the second jet centerline, $x/D=7.5$, the other profile is asymmetric, observed at $x/D=5.9$. This indicates the

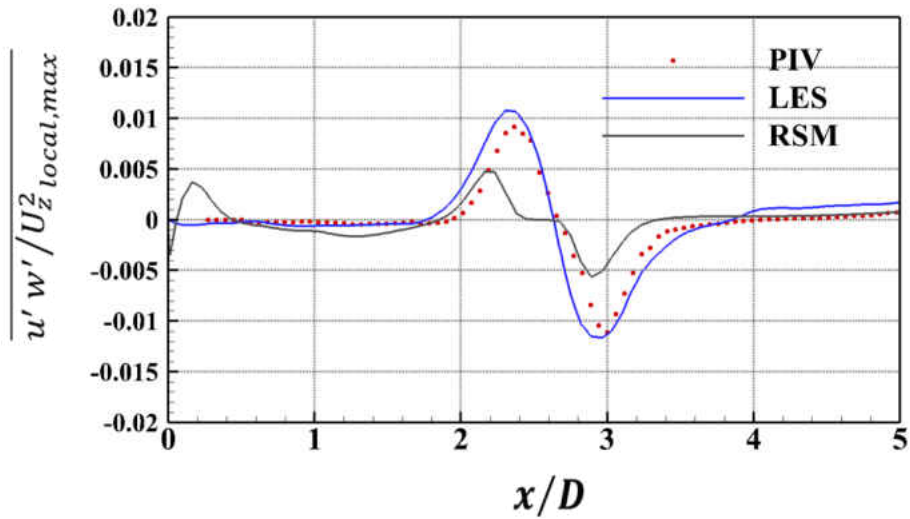


Figure 105 Turbulent shear stress profile close to the target wall, $z/D=0.25$ (first jet)

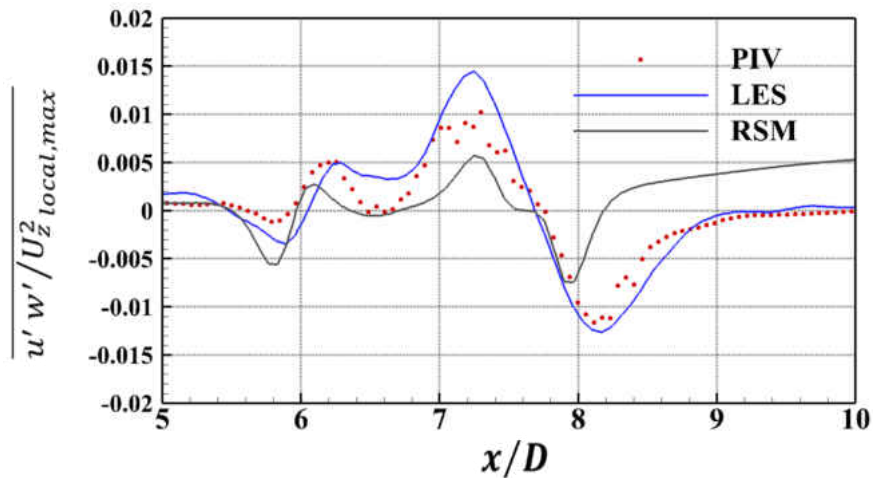


Figure 106 Turbulent shear stress profile close to the target wall, $z/D=0.25$ (second jet)

region of wall jet recirculation zone. The magnitude of the shear stress due to wall jet collision is smaller compared to the magnitude of shear stress created by jet shear layer. As the cross flow gains more momentum, the jet bends more and it is expected that the recirculation zone due to wall jet collision will be pushed towards the centerline of the third jet. This can be seen in Figure 107 where a change in sign of shear stress profile happens at $x/D= 11.5$. Further downstream, between $X/D=15-20$ Figure 108 the cross flow gains enough momentum to push all the flow in one direction

hence we do not see a similar wall jet recirculation zone. Deviation on the Reynolds shear stress regarding the profile is observed between PIV and LES for the fourth jet. One of the possible reasons could be the jet trajectory is different in PIV and LES at this location. The difference in jet trajectory causes the difference in mean velocity gradient, causing a slight offset in the peak of Reynolds shear stress for LES. RSM failed to predict the correct magnitude and trend for all the jets when compared to PIV and LES.

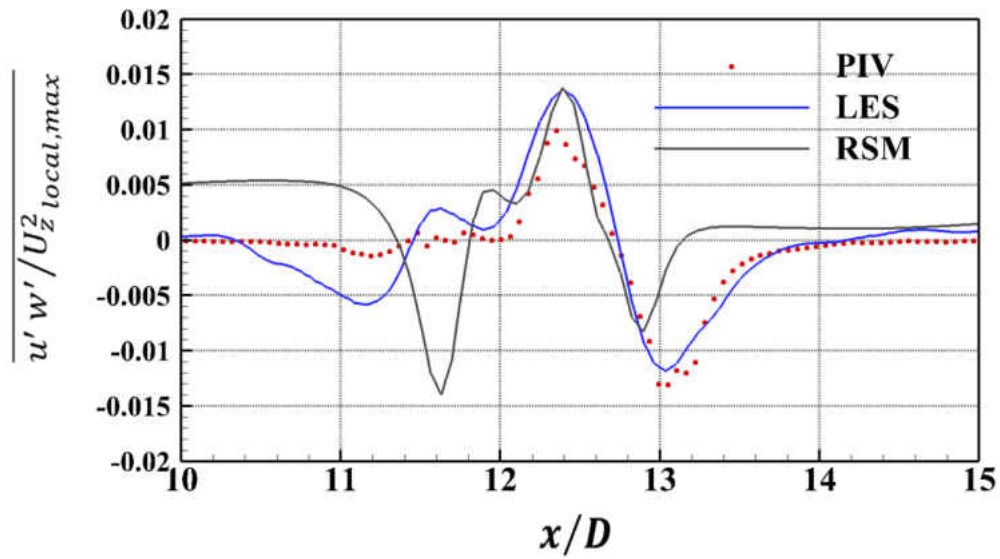


Figure 107 Turbulent shear stress profile close to the target wall, $z/D=0.25$ (third jet)

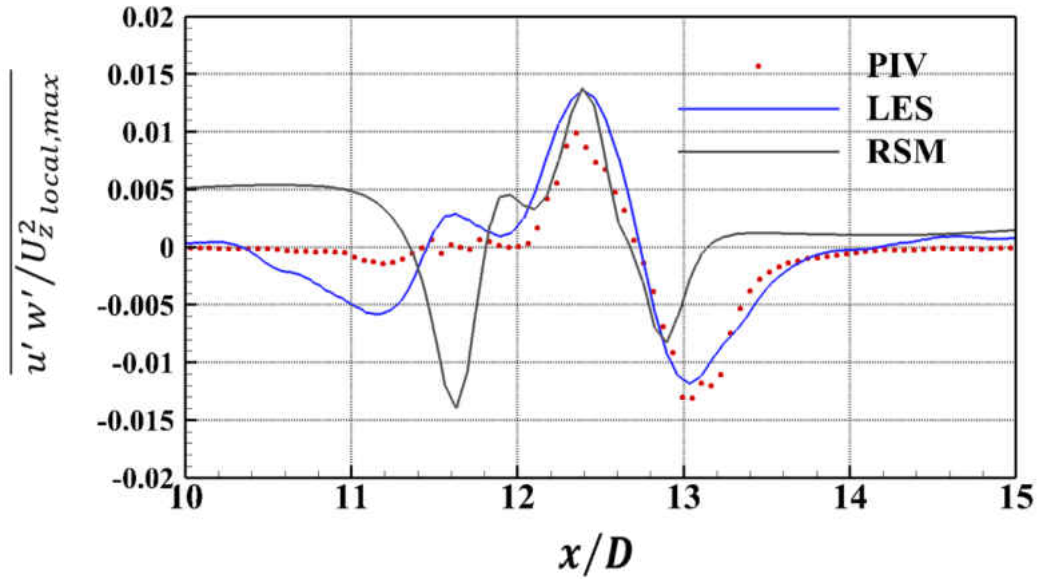


Figure 108 Turbulent shear stress profile close to the target wall, $z/D=0.25$ (fourth jet)

Turbulent Kinetic Energy Budget

The mean turbulent kinetic energy can give information about the main characteristics of turbulence in a flow. Taking the trace of the mean Reynolds stress equation yields the turbulent kinetic energy and can be written as:

$$\underbrace{\frac{\partial k}{\partial t} + U_j \frac{\partial k}{\partial x_j}}_{C_k} = \underbrace{-\overline{u'_i u'_j} \frac{\partial U_i}{\partial x_j}}_{P_k} - \underbrace{\frac{\partial}{\partial x_j} \left[\frac{1}{2} \overline{u'_i u'_i u'_i} + \frac{1}{\rho} \overline{p' u'_i} \delta_{ij} - \vartheta \frac{\partial k}{\partial x_j} \right]}_{D_k} - \underbrace{\vartheta \left(\frac{\partial u'_i}{\partial x_j} \frac{\partial u'_i}{\partial x_j} \right)}_{\varepsilon_k}$$

Where C_k indicates mean flow convection, P_k denotes production of turbulent kinetic energy due to shear and normal stresses, D_k is the diffusive transport and ε_k is the viscous dissipation. One of the purposes of the current study is to validate LES's capability to predict mean flow and turbulent statistics for the narrow wall impingement problem. The experiment was performed on this kind of impingement channel to satisfy the need for experimental data to validate turbulence models

which was not available in the published literature prior to this work. Even though all these individual terms can be calculated from the current 3D LES simulations, the current study is only limited to the terms that can be calculated from the 2D PIV data for the turbulent energy budget calculation and the fidelity of the LES technique for a narrow wall impingement problem can be tested. All the production terms in the Figures are non-dimensionalized by $\frac{U_{z,max,local}^3}{D}$.

The production of turbulent kinetic energy (P_k) and the mean flow convection (C_k) was calculated from the PIV and compared with LES to the centerline plane of the channel. Since the purpose of the impingement is to remove heat from the target surface, a location close to the target wall ($z/D=0.5$) is used for comparison shown in Figure 109

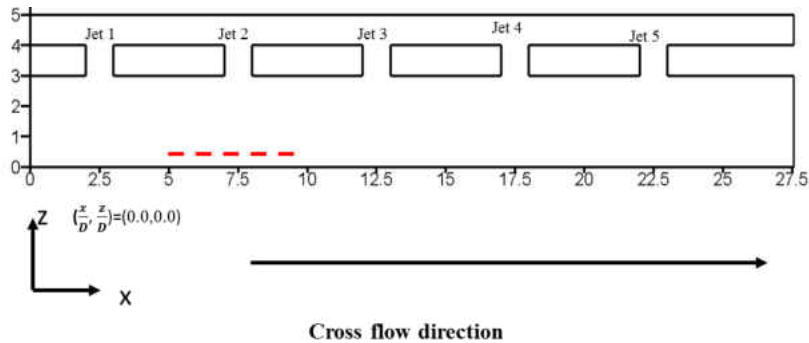


Figure 109 Location for turbulent kinetic energy budget calculation

The turbulent kinetic energy due to production can be expressed

$$P_{k,normal} = -\overline{u'^2} \frac{\partial U}{\partial x} - \overline{w'^2} \frac{\partial W}{\partial z} \quad (65)$$

Figure 110 shows the production due to normal stresses ($P_{\overline{u'^2}}, P_{\overline{w'^2}}$) calculated from the experiment. ($P_{\overline{w'^2}}$) is the dominating term when compared to ($P_{\overline{u'^2}}$) term. The wall parallel

component $\overline{u'^2}$ at this location is very small compared to $\overline{w'^2}$, hence the term $-\overline{u'^2} \frac{\partial U}{\partial x}$ is almost negligible.

It was found from the experiment that $\overline{w'^2} \frac{\partial W}{\partial x}$ is contributing the most for the production of $P_{k,normal}$

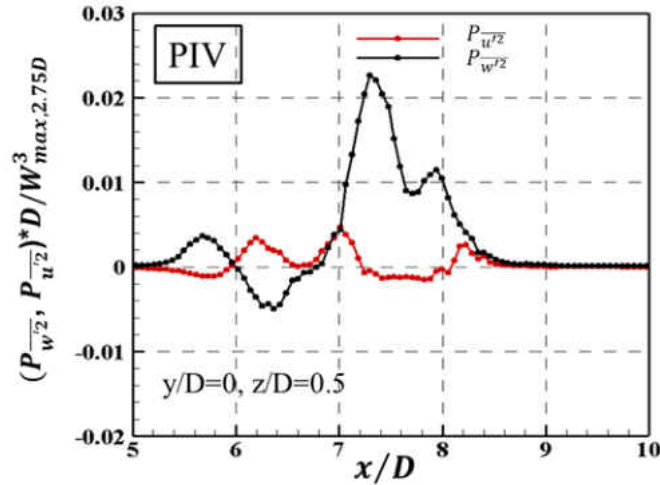


Figure 110 Contribution of the normal stresses to the production rate of turbulent kinetic energy

The contribution of normal stress ($P_{v'^2}$) to the turbulent kinetic energy is found to be negative at $x/D \sim 6.4$ as shown in Figure 110. This happens when the flow accelerates and turbulence energy transfer from small scales to the large scales. Figure 111 shows the velocity vector obtained from PIV. The location where the normal stress, ($P_{v'^2}$) is negative at $x/D \sim 6.4$, a recirculation zone is observed at the same location suggesting the flow is accelerating due to upwash motion of the fluid.

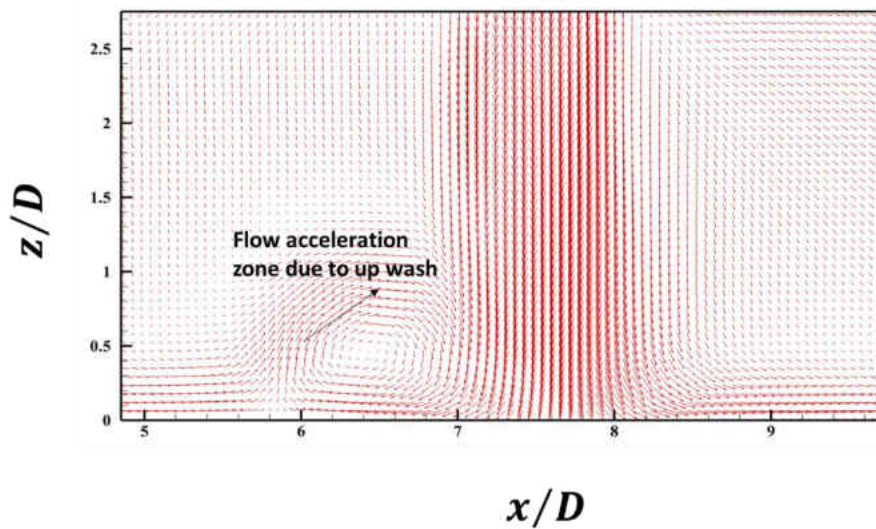


Figure 111 Velocity vector from PIV

Figure 112 shows the turbulent kinetic energy production due to normal stresses ($P_{u'^2} + P_{w'^2}$). LES and PIV shows good agreement for the production of turbulent kinetic energy due to normal stresses. The positive P_k indicates that the energy is being extracted from the mean flow and the term that is responsible for extracting the energy from the mean flow field is the Reynolds stresses. Negative production of turbulent kinetic energy was noticed at $\sim x/D = 6.1-6.8$. This indicates that transfer of energy is happening from the turbulent flow field to mean flow field at this location.

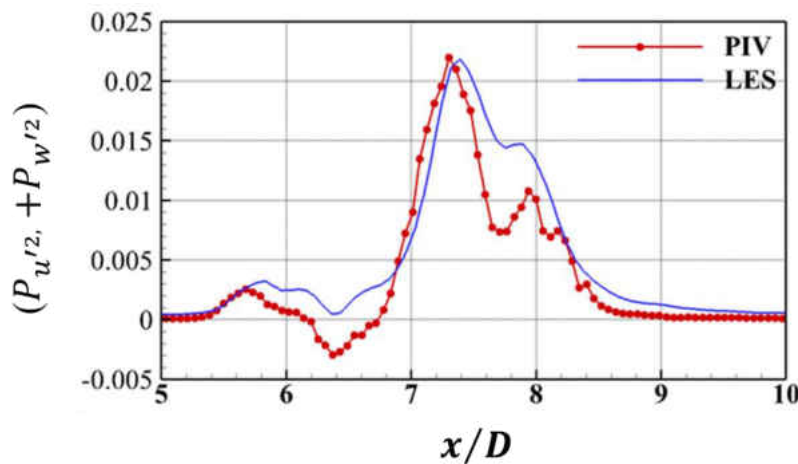


Figure 112 Turbulence production due to normal stresses

Figure 113 shows the comparison between PIV, LES, and RSM for the turbulent kinetic energy production due to wall normal stress from x/d 5-10. This corresponds the second jet location. LES was able to predict the production due to wall normal stress reasonably well in the near wall region. It is interesting to note that LES was able to predict the negative production of turbulent kinetic energy. RSM shows poor capability of predicting the production term due to wall normal stress component both in terms of profile and magnitude. This suggest that the jet shear layer and up wash motion were not captured well in RSM calculation. In addition to that it is interesting to note that RSM predict a negative production of turbulent kinetic energy due to wall normal stress component at $\sim x/D=8$. Calculation from PIV and LES do not show any negative production at this location.

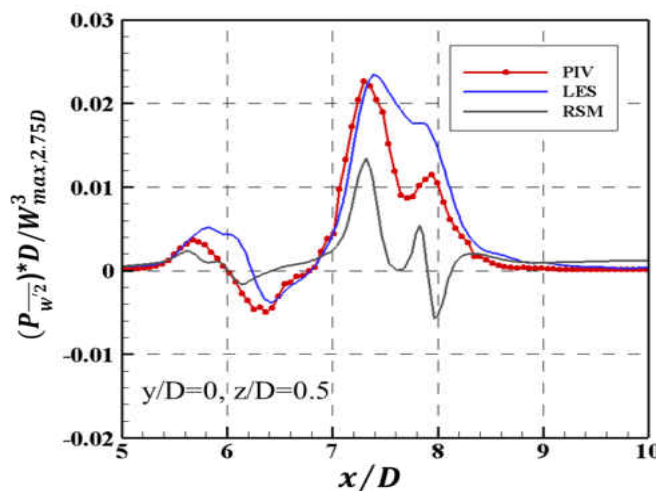


Figure 113 Comparison of turbulence production rate due to normal stress (PIV, LES, and RSM)

To understand the reason behind RSM predicting the negative production of turbulent kinetic at x/D 8, whereas PIV and LES do not such phenomena. Velocity streamlines and negative production of P was plotted in the same figure as shown in Figure 114. The black solid line shows where the profile of the pk was taken. The profile is shown in Figure 114 to the right. At location

$x/D=8$ PIV and LES streamline shows that the streamlines are diverging after emanating from the jet orifice. This is expected since the crossflow is moving in one direction. The RSM calculation shows the opposite trend than PIV and LES where the flow is pushed in due to the entrainment and causes a local acceleration in the region where p_k goes to negative. In other words flow is accelerating rather than slowing down in RSM calculation.

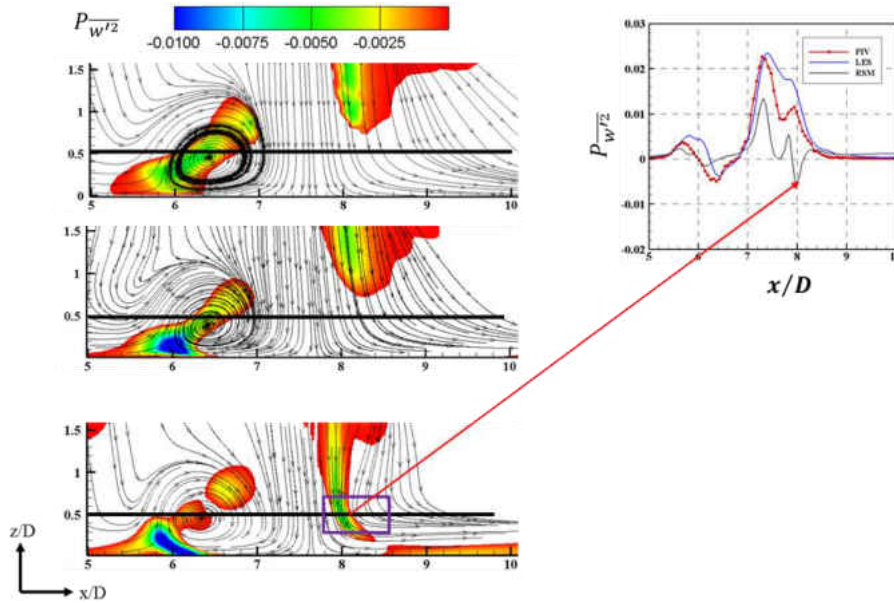


Figure 114 Velocity streamline and negative contour of $P_{w'^2z}$

Production due to shear stress can be calculated as follows:

$$P_{k, shear} = -\overline{u'v'} \left(\frac{\partial U}{\partial z} + \frac{\partial w}{\partial x} \right) \quad (66)$$

$P_{k, shear}$ is mostly driven by mean velocity gradient. As expected the $P_{k, shear}$ is maximum at the location of jet shear layer. PIV and LES shows good agreement for $P_{k, shear}$ as can be seen in Figure 115

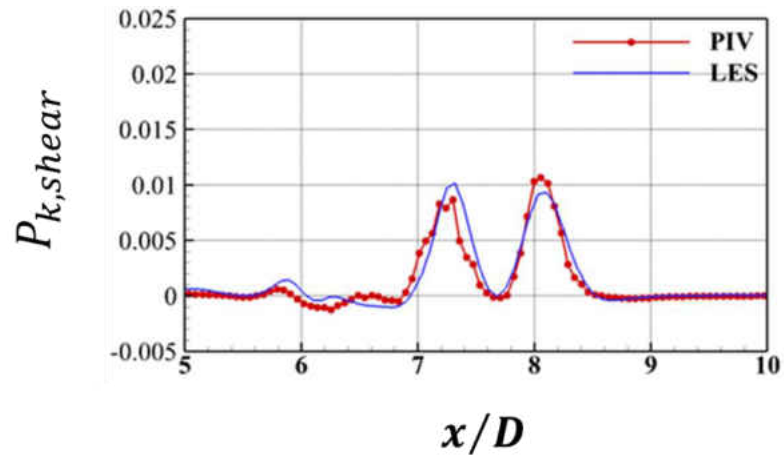


Figure 115 Production of turbulent kinetic energy due to shear

CHAPTER 8: DETAILED HEAT TRANSFER ANALYSIS

Heat Transfer Comparison

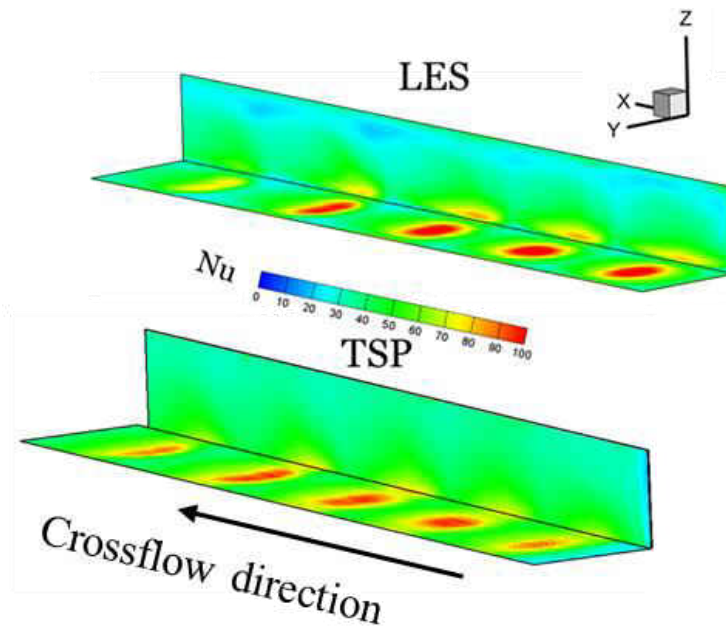


Figure 116 Isometric view of the target wall and sidewall heat transfer comparison for $Re_j = 15,000$ (top-LES; bottom-Experiment (TSP))

Figure 116 shows the local heat transfer distribution calculated from LES (top) and local heat transfer distribution obtained from TSP (bottom). El-Gabry and Kaminski [57] emphasized the importance of obtaining local heat transfer distributions for the impingement cooling problem. First, designs that are based on averaged heat transfer are most likely to fail in practical operations due to extreme temperature gradients and thermal stresses. Hence a local heat transfer distribution provides the designer the details of the thermal behavior. Second, results obtained from the local temperature distribution can be used to validate CFD results so that CFD can be used as a reliable design tool in industry. The iso-metric view in Figure 116 provides a detailed thermal imprint of

the orthogonal jets after impinging onto the target surface as well as the ability of the wall jets to pick up heat from the sidewall due to upwash motion.

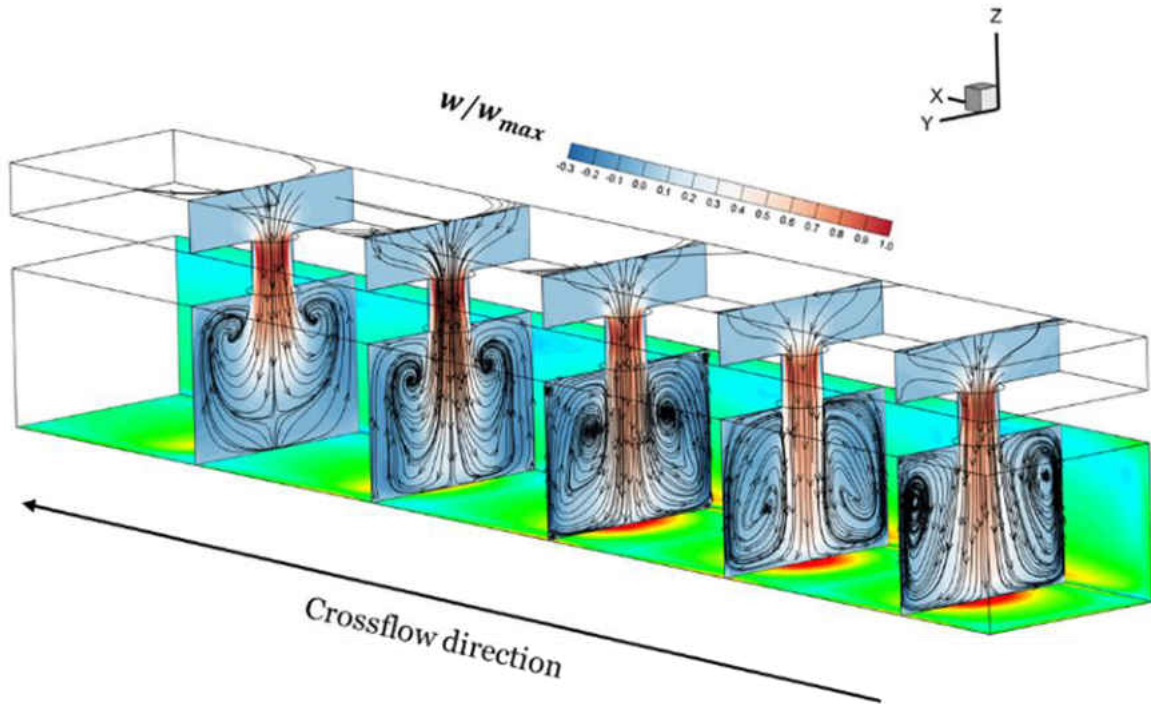


Figure 117 Detailed flow visualization and heat transfer calculated from LES ($Re_j = 15,000$)

The flow development inside the narrow wall channel with respect to the heat transfer calculated from LES is shown in Figure 117. The wall normal velocity is normalized with respect to the maximum wall normal velocity inside the channel in Figure 117. Velocity streamlines are superimposed on the flow contours. The first jet appears to be spreading more than the second jet. The build-up of crossflow from the third jet onwards and how it is preventing the individual jets from penetrating all the way towards target wall can also be seen in Figure 117. The counter rotating vortices created from the upwash are mainly responsible for the sidewall heat transfer. Due to the accumulation of the crossflow, the center of the CVP are being pushed towards the jet plate for the

third, fourth, and fifth jet. This phenomena causes the sidewall heat transfer distribution to differ compared to different than the upstream region of the sidewall.

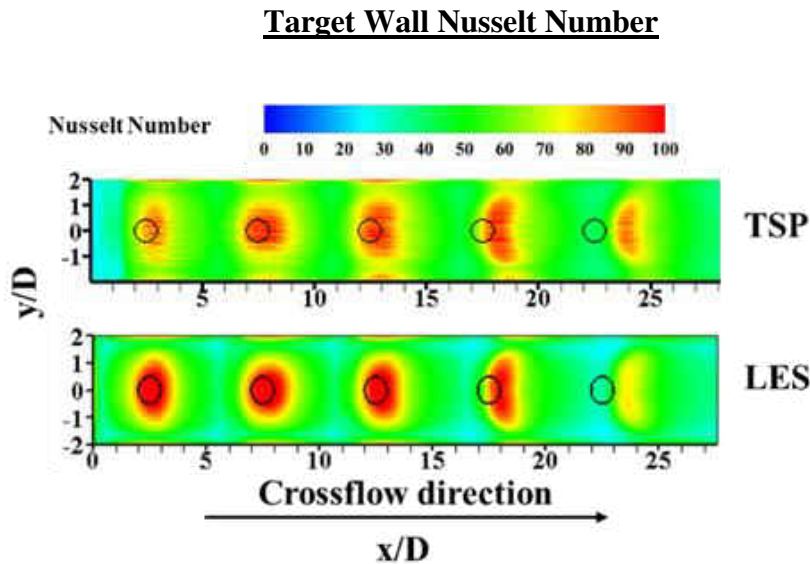


Figure 118 Target wall Nusselt number contour ($Re_j = 15,000$)

Figure 118 shows the target wall Nusselt number obtained from experiment (top) and from LES (Bottom). Both experiment and CFD agrees well for the target wall Nusselt number distribution. The impinging positions on the target wall are clearly visible from the Nusselt number contour which shows higher heat transfer coefficients. The effect of crossflow becomes stronger from the third jet where the thermal imprint of these jets (third, fourth and fifth) shifted downstream of the jet centers. This is due to the fact that crossflow has gained enough momentum to bend the jets. The thermal imprint of the individual jets are found to be different and are not universal in nature. For example, in the experiment, the first jet appears to be elliptical. The presence of an end cap wall before the first jet and the presence of the second jet, creates a different boundary condition

for the first jet. The presence of these two factors cause the thermal imprint of the first jet to elongate more in y direction. As the effect of crossflow is also minimum for the second jet, the second jet is circular in shape. After the second jet, the identity of the pure impinging jets are being altered by the crossflow which makes the third jet shape to be oval and the fourth and fifth jet to be the kidney shape where the crossflow effect is severe. These shapes are also captured well by LES for the individual jets when compared to the experiment.

To further understand the thermal imprint behavior of the first jet (elliptical shaped) and second jet (circular jet shaped), wall normal velocity contours were superimposed on the target wall heat transfer distribution from LES. This is shown in Figure 119. The wall normal velocity contour was normalized by the maximum velocity for the individual jets. As the spreading rate of the first jet is larger than the second jet the jet appears to be elliptical shape. For the second jet, the jet behaves similar to a classical orthogonal impinging jet, this causes the thermal imprint of the jet to be more circular in shape.

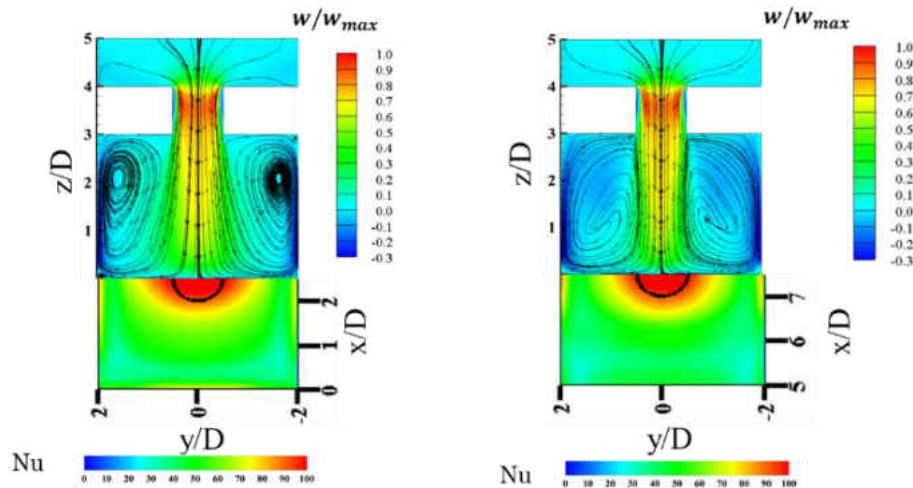


Figure 119 Velocity and heat transfer for the first and second jet (Obtained from LES)

Figure 120 shows the laterally averaged Nusselt number obtained from the experiment and LES. Laterally average Nusselt number calculations were done by averaging the Nusselt number profiles in the spanwise direction. The uncertainty in the Nusselt number was calculated to be 9.6%. The stagnation point heat transfer are in excellent agreement between experiment and LES. Figure 120 also shows the ability of LES to predict stagnation point heat transfer accurately. All the data gathered from the simulations (LES and RANS) and experiment reveals that heat transfer is a manifestation of flow and matching flow physics data is a precursor for any numerical model to predict accurate heat transfer for an impingement heat transfer problem.

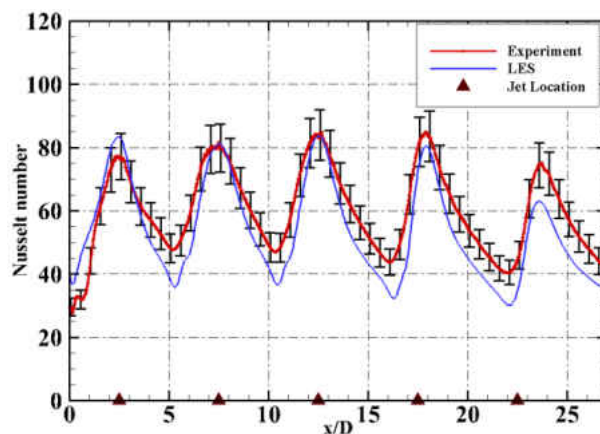


Figure 120 Laterally averaged Nusselt number comparison for $Re_j = 15,000$ (Experiment and LES)

It can be seen from Figure 120 that the heat transfer in-between jet locations (the valley region of the profile) were not predicted accurately by LES. The discrepancy in the valley region of the heat transfer profile is due to the fact that the kinetic energy was resolved $\sim 75\%$ in LES in this regions. The rest of the domains were resolved well enough (above 80%) in the current simulation.

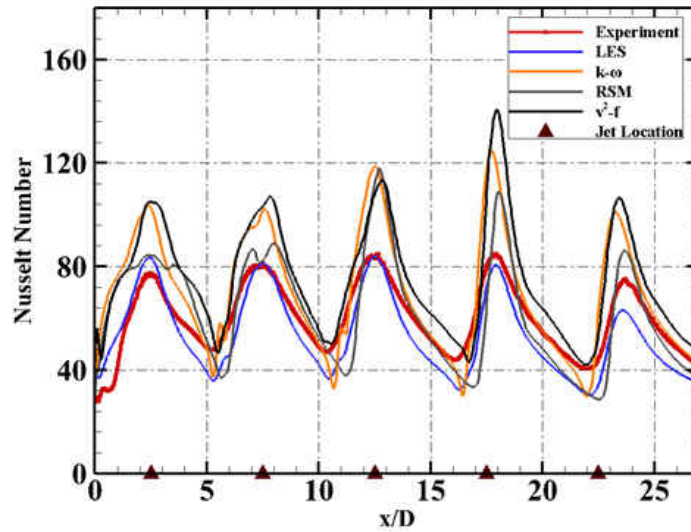


Figure 121 Laterally averaged Nusselt number comparison $Re_j = 15,000$ (Experiment, LES and RANS)

Figure 121 shows the laterally averaged Nusselt number comparison obtained from the experiment, LES, and RANS. RANS prediction shows different heat transfer behavior than that of experiment and LES. Predicting stagnation point heat transfer accurately is one of the distinct drawback for the conventional RANS models. Even the best of the RANS models, the $v2-f$ model, can be inaccurate by up to 2-30%.for impingement heat transfer [87]. This was expected and discussed in the “centerline jet velocity” section. The centerline axial jet velocity from LES revealed identical profile when compared to the PIV. RANS showed a much different jet behavior where the jet impinges onto target surface with higher momentum than in the experiment.

Sidewall Wall Nusselt Number

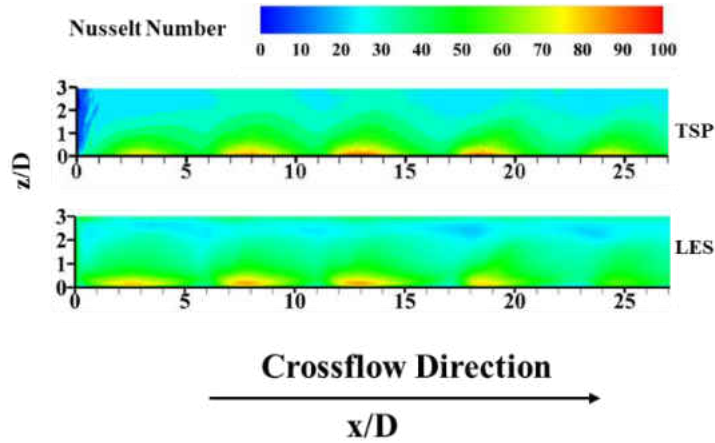


Figure 122 Sidewall Nusselt number contour($Re_j=15,000$)

Figure 122 shows the sidewall Nusselt number contour comparison between experiment and LES. The agreement between experiment and LES is promising. The thermal imprint produced by the wall jets was predicted accurately in LES.

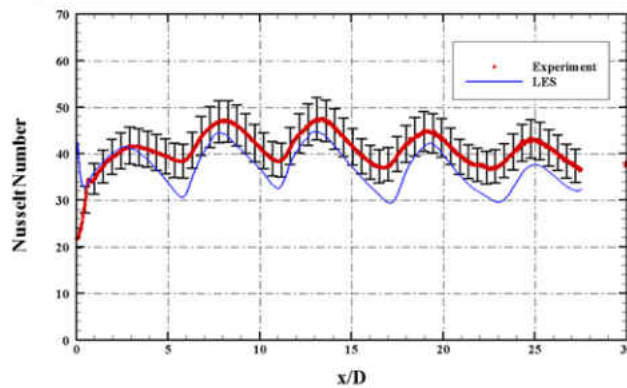


Figure 123 Laterally averaged Nusselt number for the sidewall heat transfer for $Re_j=15,000$ (Comparison between experiment and LES)

Figure 123 shows the laterally averaged Nusselt number comparison between experiment and LES. The magnitude and profile for the sidewall heat transfer showed good agreement between experiment and LES. The surface averaged Nusselt number for sidewall is ~30% lower than that of the target wall.

CHAPTER 9: CONCLUSION AND FUTURE WORK

Curved Surface Impingement

A detailed experimental and numerical investigation on impingement heat transfer on a curved surface has been performed for four different jet Reynolds numbers (55,000-125,000). From the baseline study, it was found that at the downstream section heat transfer deteriorates significantly compared to upstream impingement section. In an attempt to enhance heat transfer at the downstream section different types of turbulators were placed to enhance mixing in the flow. By adding turbulators in the post-impingement region, heat transfer can be enhanced significantly while maintaining the same pressure drop as no turbulator case. For each configuration, the pressure drop across the channel exhibited the same trend for all the Reynolds numbers. Both the W-shaped and 90° turbulators showed positive impact on heat transfer with almost no negative impact on pressure drop due to the low blockage ratio (e/Z) of 4.76%. The secondary flow created by the W-shaped (W1- and W-2) turbulators produced more uniform heat transfer distribution than 90° turbulators. Even though both the 90° and W-1 shaped turbulators showed almost identical heat transfer augmentation, the W-1 shaped turbulators are more desirable from a design aspect as the feature produces a more homogenous temperature gradient than that of the 90° turbulators. As a result, W-1 shaped turbulators would reduce part failure caused by high thermal stresses. It was also found that the rib orientation with respect to crossflow needs to be taken into consideration for designing the W shaped rib.

Array Impingement

An array impingement configuration was studied experimentally and numerically. TSP was used to obtain a local heat transfer distribution. The heat transfer data shows that at low streamwise spacing heat transfer profile remains constant compared to the florschuetz et al. [109] prediction where the heat transfer decays significantly at the downstream.

Flow visualization study using PIV was done on one of the jet rows centerline plane. CFD was performed to compare the experimental results. It was found that the jet diffusion is more in the experimental results suggested the jet shear layer thickness was not predicted accurately in CFD. The jet trajectory calculated by CFD was also found to be different than in PIV.

Narrow Wall Impingement

A detailed experimental and numerical investigation on the flow field of impingement heat transfer on a narrow wall has been performed for a jet Reynolds number of 15,000. PIV was performed on the centerline of the channel to gather information about individual jet behavior. Predicting impingement heat transfer using RANS models has been a very challenging problem over the years due to the complexity of this flow field. Since heat transfer is a manifestation of flow, the objective of the current study was to understand the flow field inside a narrow wall impingement channel, and evaluate the performance of various numerical models against experimental data. Simulating an impingement problem in a narrow wall channel is an inherently complex problem. Initially, the first few jets behave like orthogonal impinging jets. Past the transition region, the problem behaves as a jet in crossflow. Hence, simulating a narrow wall impingement channel involves modeling

two different complex problems. Nowadays with growing computational power and resources, CFD are widely used as a design tool and the potential of LES needs to be investigated in engineering applications such as impingement cooling, where current RANS models failed to predict flow features and heat transfer distribution accurately. LES and RANS were carried out to find out the best numerical model for impingement the heat transfer problem. Despite the formidable demand on computational resources to perform LES on a wall bounded flow problem, LES shows very promising prediction capability on the flow field, when compared to RANS for this problem. Flow features like jet-to-jet interaction, stagnation flows, upwash fountain flows, and recirculation due to collision of wall jets, between adjacent jets, were captured accurately by LES.

Future Work

Understanding flow physics of impingement cooling in relation to heat transfer is complex. Based on the lesson learned from the current study, the author proposes following topics to be studied and can be considered as future work for the continuation of the current study:

Topic1: Revisiting Single Round Jet Impingement

In engineering applications most of the flow is turbulent. It is well-known that the effect of inlet conditions have a significant effect on the flow field of turbulent jet flow field [110]. Typical RANS models are most widely used for industrial applications as the cost of computation is minimal compared to the LES or DNS. It is worth noting that the typical RANS model contains

many calibrated constants, but these constants are calibrated against simple shear flows. However, impingement flow has very complex turbulent motion. Initially, as the jet approaches the target wall, the involvement to the turbulence field caused by the normal strain rates are noteworthy near the stagnation region, but after impingement as the flow radially develops the shear strain becomes dominant in the form of wall jet flow [94]. Flow phenomena like this make the typical RANS model quite difficult to predict the correct flow pattern for the impinging jet.

Several numerical studies have been performed on single round jet of impinging flows using LES technique. The results from these works are compared to the data by copper et al. [111] for the flow field and Baughn et al. [92] for the heat transfer comparison. The two experiments were run in two different conditions. Hence, the boundary conditions that need to be implemented are not clear for a numerically expensive computational technique like LES or DNS.

Moreover, the inlet turbulence flow field data was not described adequately by Cooper et al. [111]. Different authors have used different pipe length to generate the inlet flow conditions that go into the impinging flow field. The author proposes to perform a single round jet experiment that includes both the local heat transfer and detailed flow visualization data with identical boundary condition and Reynolds number. While designing the experiment three major factors need to be take into consideration and report accurately which have been not clearly reported in the published single jet impingement literature to formulate the numerical setup without any error or conjecture :

Confinement Condition

The study done by Baughn et al. [92] and Cooper et al. [111] had no confinement. Uddin et al. performed LES of a single round impinging jet, but numerical setup had a confined boundary

condition. The results were compared with the data from Baughn et al. [92] and Cooper et al. [111]. Hadziabdic and Hanjalic [112] used three different types of boundary conditions to simulate the open surface and found large differences in in the streamline patterns.

Nozzle Exit Condition

The nozzle outlet condition plays a crucial role in predicting the correct flow field and heat transfer. A mismatch in the nozzle exit condition in the numerical model can result in predicting inaccurate flow field and heat transfer data. Figure 124 below shows the importance of obtaining detailed and accurate boundary conditions and the detailed experimental data can be used to generate more realistic inlet condition instead of using a numerically artificial boundary condition.



Figure 124 Scalar contour shows the effect of three different inlet velocity profiles [68]

One of the methods to generate inflow conditions in numerical simulation is to use a mean velocity profile and add random perturbation to it. Frohlich and Rodi [113] reported that this method of inflow generation gives incorrect results. Another benefit of gathering detailed information of flow

field is that instead of running a precursor simulation of a pipe flow, the detailed experimental data near the exit of the nozzle can be used to generate more realistic inflow condition.

Distribution of the Grid

Piomelli and Chasnov [71] have given a mesh criteria for performing wall model and wall resolved LES flow. Grid spacing must be chosen carefully because this determines the cutoff filters for LES that determines the inertial range. Recently Hadziabdic and Hanjalic [112] reported that this requirement is not sufficient for impinging flow. The author suggests to investigate these mesh criteria in a more methodical way and if possible establish a mesh criteria for LES in impinging flows.

Motivated from the information above the author planned to perform a single jet wall resolved LES. But due to time constraints it was not possible to finish the work. But it can be considered as possible future work from this current study. The mesh shown in Figure 125 has the mesh criteria which satisfies the criteria for wall resolved LES simulation.

Table 12 Mesh criteria for wall resolved LES

Δy^+	.89<1
Δr^+	~36
$r\Delta\theta^+$	~20

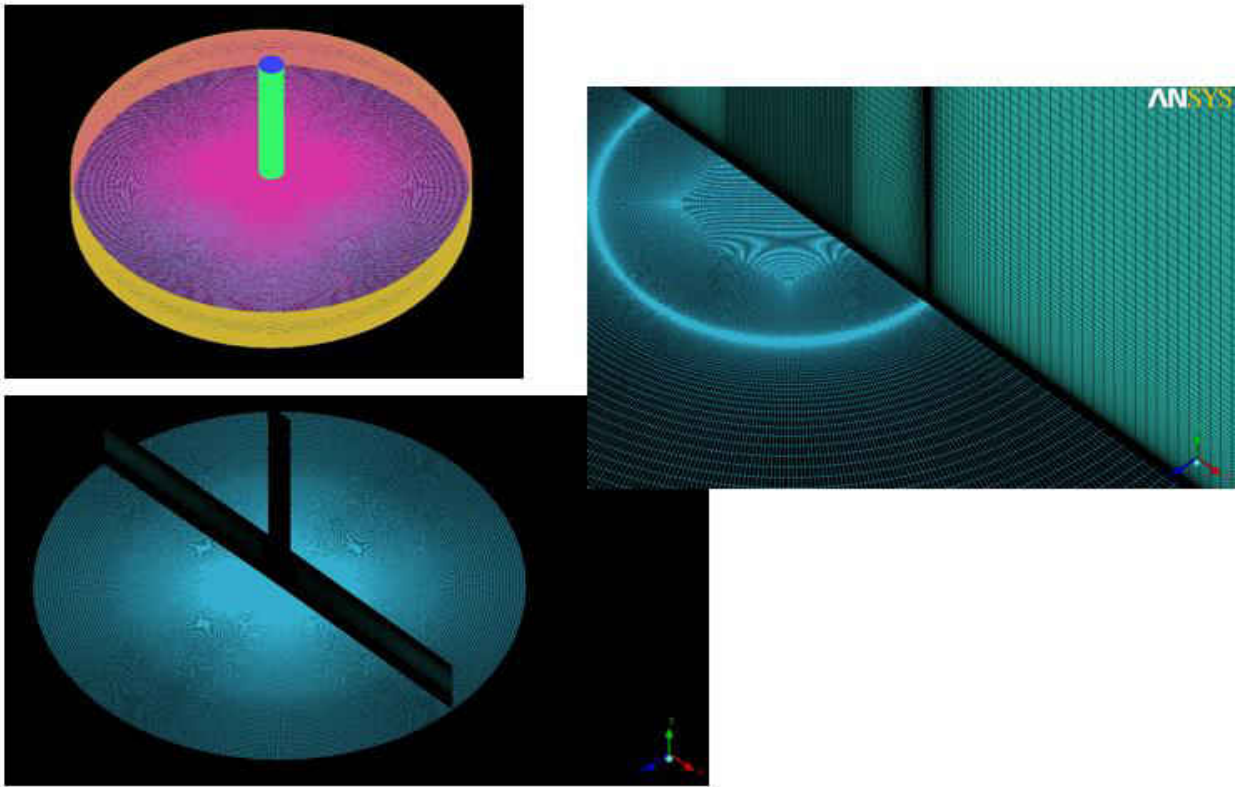


Figure 125 Wall resolved mesh for single jet impingement LES case

Topic 2: Narrow Wall Impingement

A commercial software Starccm+ was used to simulate a narrow wall impingement configuration using LES. According to author's knowledge, this is the first time work for this kind has been done for this type of simulation. The author proposes some possible considerations that could be incorporated into this work in the future. In the current simulation, based on the grid spacing and distribution it was found that in some regions of the computational domain, especially in the plenum region, the turbulent length scales were not resolved enough. Pope [114] suggested that if the ratio of the resolved turbulent kinetic energy to the total kinetic energy is larger than 80%, the LES simulation is well resolved. Figure 126 shows the ratio of the resolved turbulent kinetic energy to the total kinetic energy. The ratio in Figure 126 is shown by the symbol, M (%)

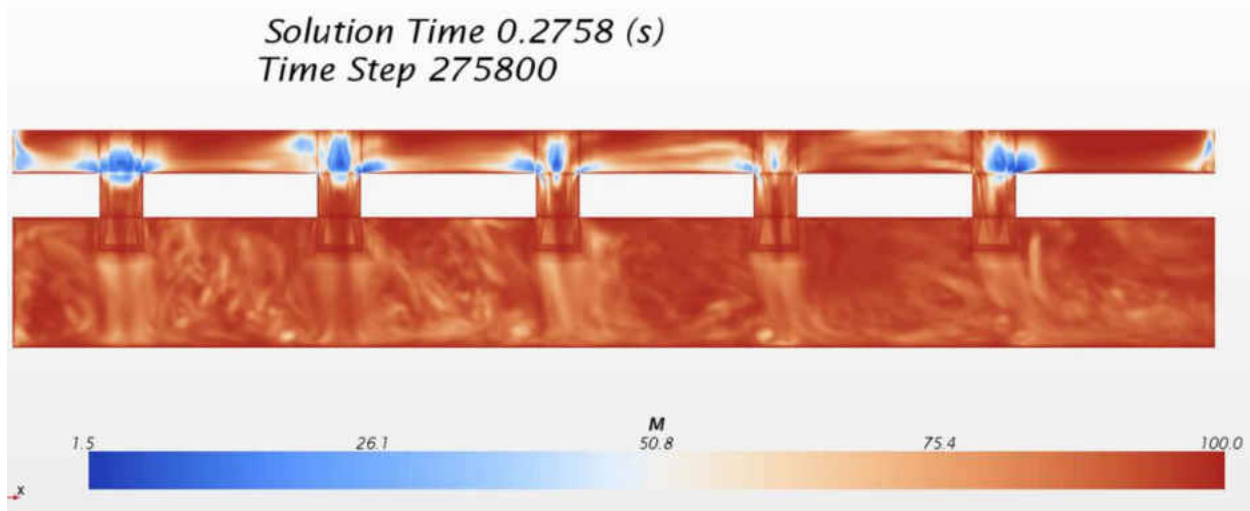


Figure 126 Ratio of the resolved turbulent kinetic energy to the total kinetic energy (M) is at the center plane of the channel

It can be seen from Figure 126 that the grid spacing and resolution is not sufficient enough in the

- Plenum region
- In the jet shear layer region

The author suggests obtaining a grid resolution such that everywhere in the domain the value of M is above 80%. The following improvements in the software and its use are also suggested if possible.

- The ratio of the resolved turbulent kinetic energy to the total kinetic energy was not readily available from the software. The author suggests some improvement or incorporates a built in function so that this value can be monitored from the beginning of the simulation.
- It is apparent from Figure 126 is that near the wall region the turbulent scales are well resolved. The shear layer of all the jets are was not well resolved. The mesh criteria near the shear layer used for free jet LES from different literature can be used for jet impingement simulation.
- In order to reduce the computational time, an adaptive refined mesh method can be incorporated into the software in which based on the value of M the code can locally refine the mesh where the scales are not resolved enough. This would save the computational time significantly.
- A detailed comparison between wall model and wall resolved LES simulation is suggested in order to understand the difference between two models. Even though wall resolved LES

is computationally very expensive, it is worth investigating the performance of the two models for jet array impingement heat transfer application. It was not possible to study this model due to lack of resources and time for computing such a large amount of cell. The mesh shown in Figure 127 satisfies the requirement for wall resolved LES mesh. Hence it was not possible to study this model due to lack of resource and time for computing such large amount of cell.

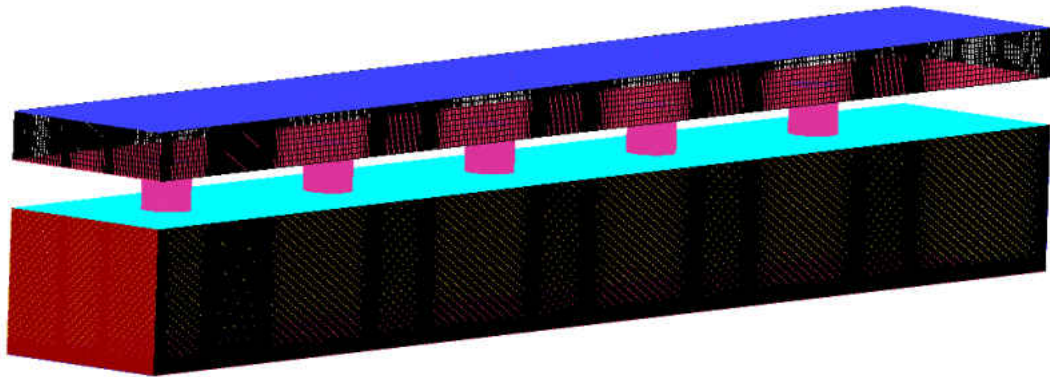


Figure 127 Wall resolved LES mesh for narrow wall impingement

Topic 3: Effect of Crossflow in a Narrow Wall Impingement Cooling

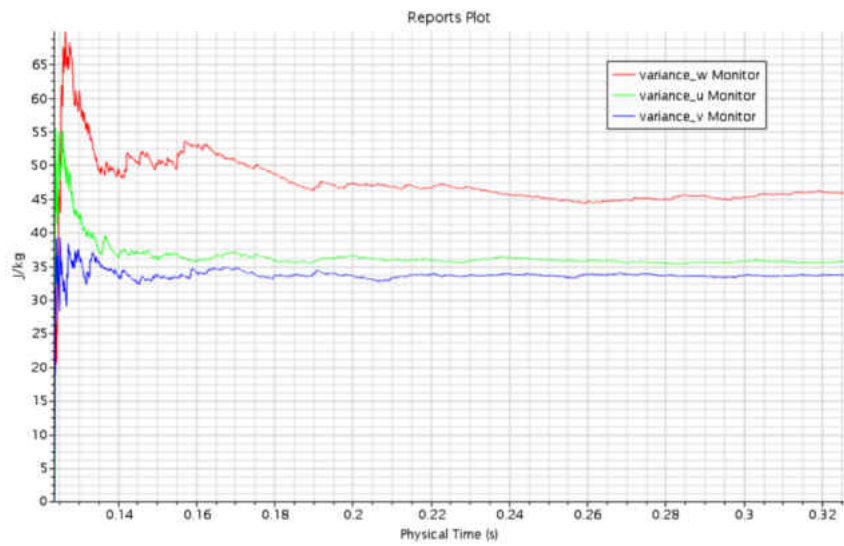
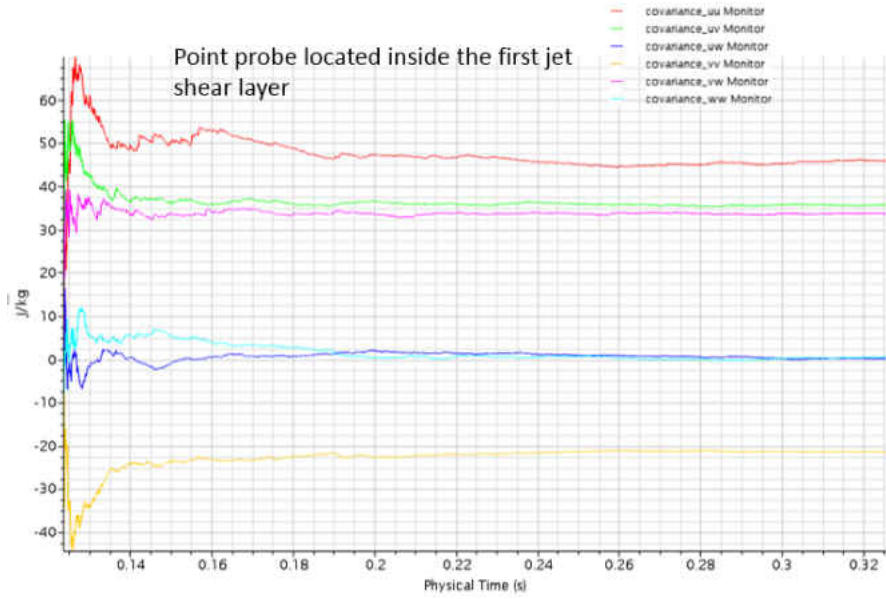
The crossflow is inevitable for any impingement cooling configuration. This crossflow degrades the heat transfer. To understand the effect of crossflow and jet interaction, a narrow wall impingent design with only one jet can be designed to study the effect of crossflow. The crossflow can be

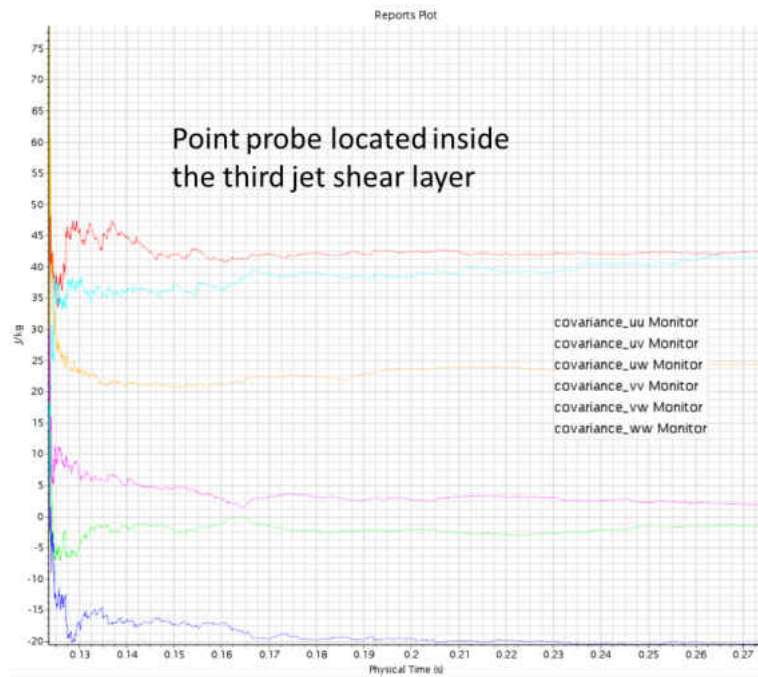
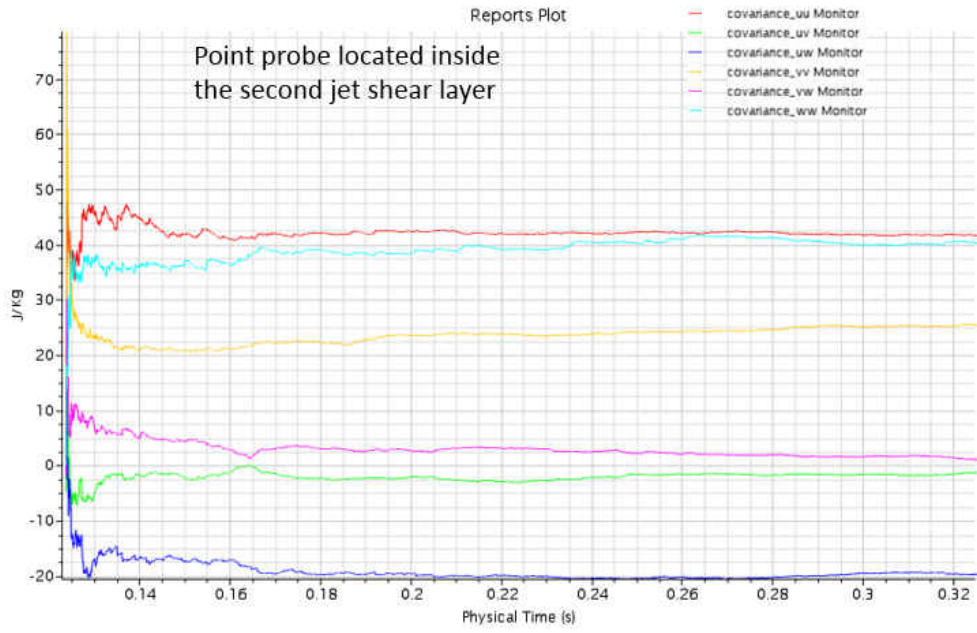
injected from the end cap wall by removing it in the present configuration. The jet Reynolds number can be fixed while the crossflow can be varied to build the test matrix.

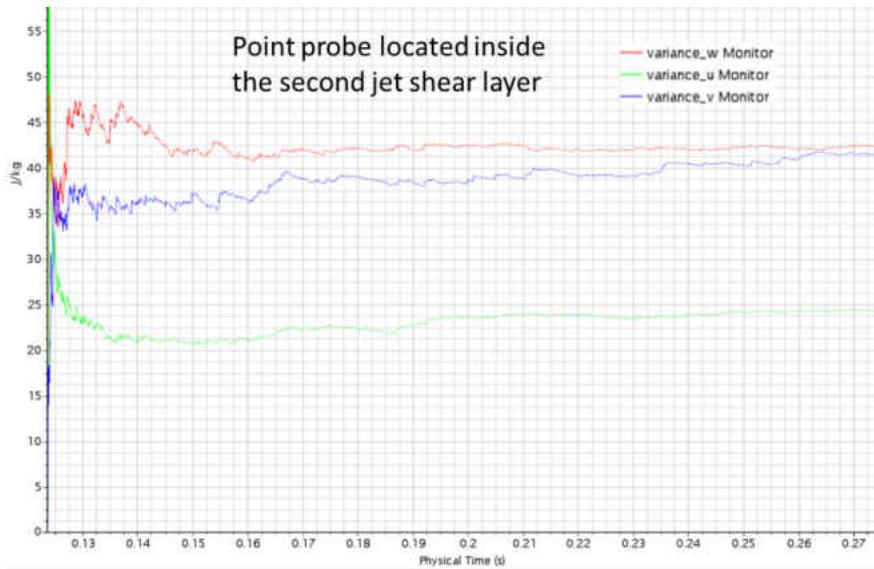
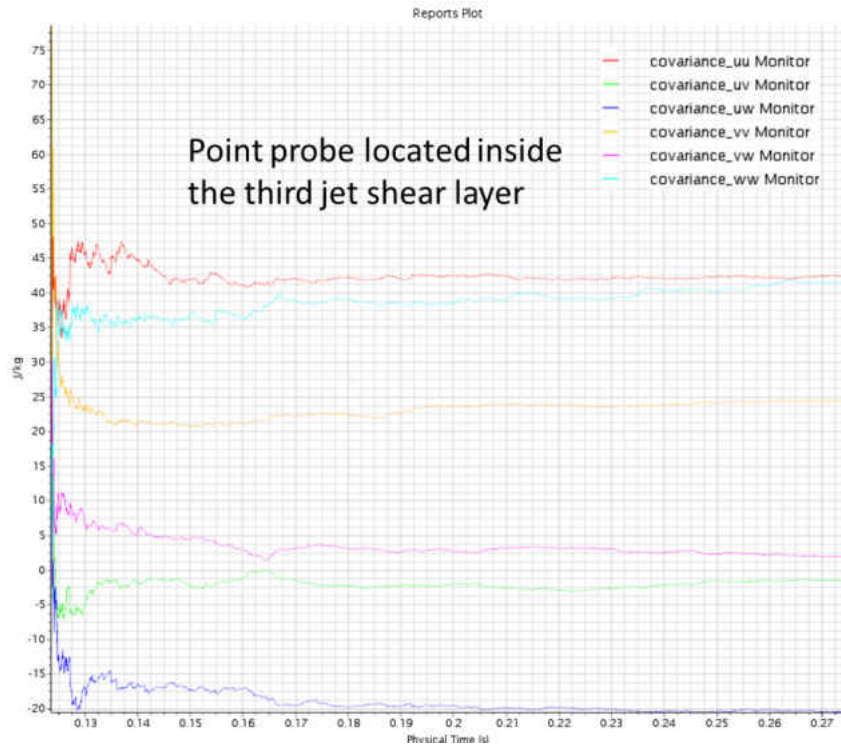
As the domain in the channel is shortened, it is possible to do wall model LES and wall resolved LES and investigate the jet degradation as the crossflow increases.

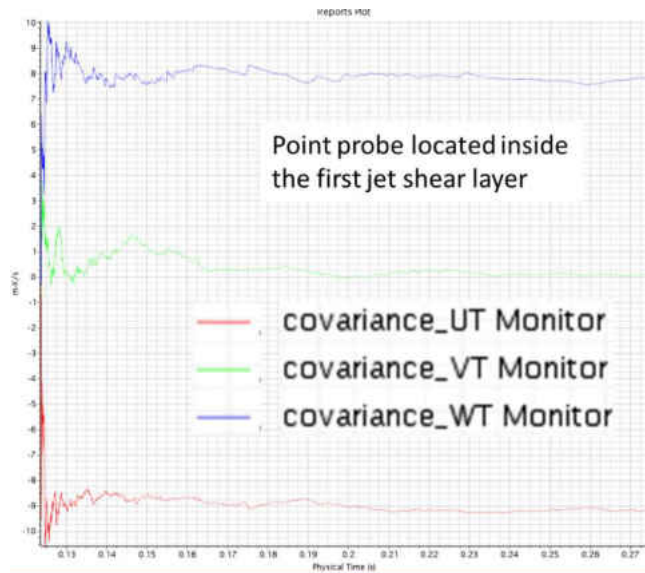
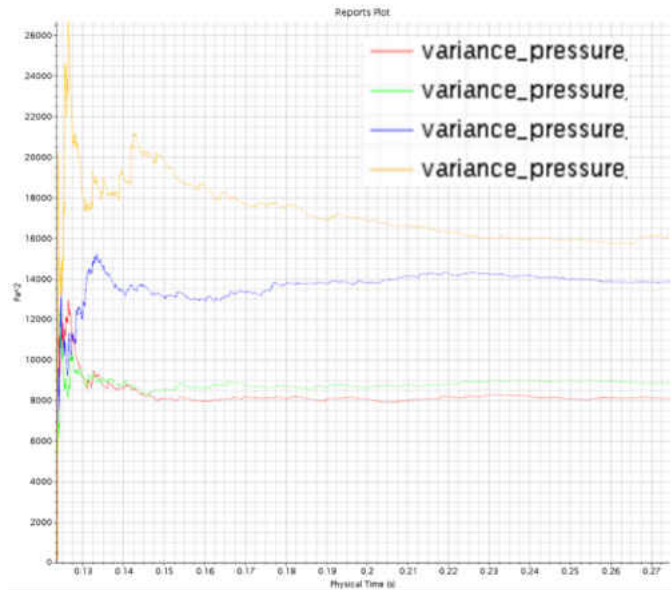
APPENDIX

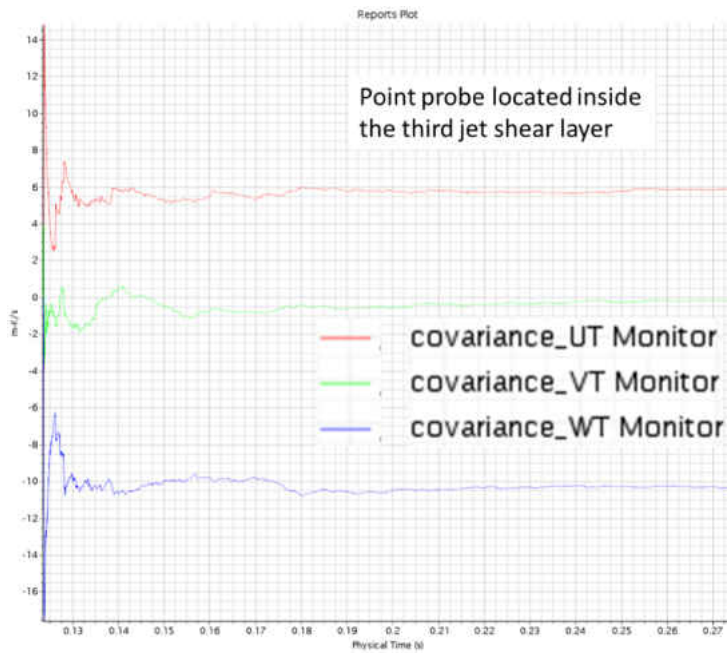
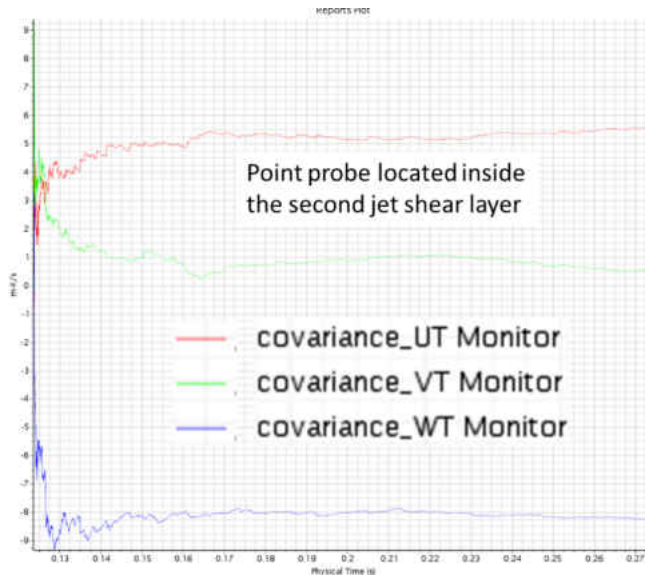
Statistical Convergence



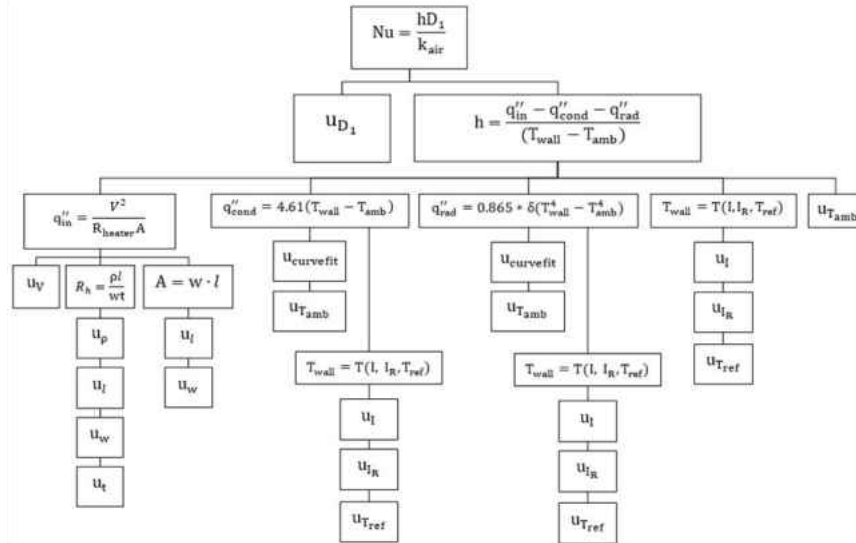




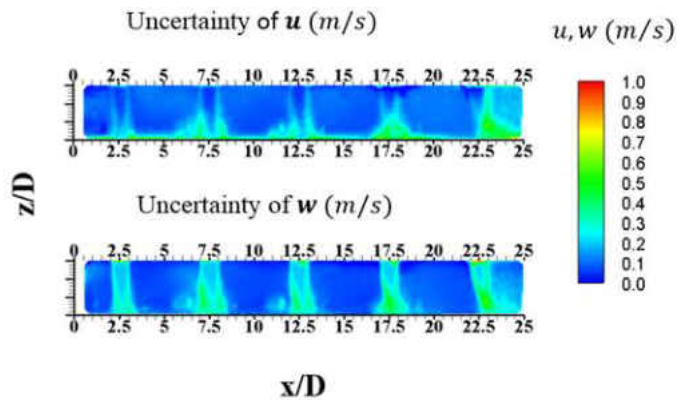




Uncertainty Tree for Heat Transfer



PIV Uncertainty



LIST OF REFERENCES

- [1] Saravanamuttoo, H.H., Rogers, G.F.C., and Cohen, H., Gas Turbine Theory, Harlow: Pearson Education, 2001.
- [2] Polezhaev, J., "The Transpiration Cooling for Blades of High Temperature Gas Turbine," *Energy Convers. Mgmt*, vol. 38, no. 10-13, pp. 1123-1133, 1997.
- [3] Terzis, A., "Detailed Heat Transfer Distributions of Narrow Impingement Channels for Integrally Case Turbine Airfoils," Institute of of Aerospace Thermodynamics of University of Stuttgart, Stuttgart, 2014.
- [4] Bunker, R. S., "Cooling Design Analysis," DOE Gas Turbine Handbook, Department of Energy, 2006.
- [5] Bunker, R. S., "Gas Turbine Heat Transfer," *Journal of Turbomachinery*, vol. 129, no. 2, pp. 193-201, 2007.
- [6] Claretti, R., "Heat and Fluid Flow Characterization of a Single-Hole-Per-Row Impingement Channel at Multiple Impingement Heights," University of Central Florida, Orlando, 2011.
- [7] Livsey, D. J. and Hamblet, M., "Air cooled gas turbine airfoil," United States Patent, 1996.
- [8] Dailey, G. M., Evans, P. A., and McCall, R. A. B., "Cooled Aerofoil for a Gas Turbine," United States Patent, 2001.
- [9] Moore, R. P., "Cooled airfoils for a gas turbine engine.," United States Patent, 1997.

- [10] Lee, C.-P. and Bunker, R. S., "Thermal shield turbine airfoil," United States Patent, 2006.
- [11] Lutum, E., Semmler, K., and von Wolfersdorf, J., "Cooled Blade for a Gas Turbine," United States Patent, 2002.
- [12] Liang, G., "Turbine stator vane with near wall integrated micro cooling channels," United States Patent, 2013.
- [13] Florschuetz, L. W., and Isoda, Y., "Flow Distributions and Discharge Coefficient for Jet Array Impingement with Initial Cross Flow," *Journal of Engineering for Power*, vol. 105, no. 2, pp. 296-304, 1983.
- [14] Florschuetz, L.W., Berry, R. A., and Metzger, D. E., "Periodic Streamwise Variations of Heat Transfer Coefficients for Inline and Staggered Arrays of Circular Jets with Cross Flow of Spent Air," *Journal of Heat Transfer*, vol. 102, pp. 132-137, 1980.
- [15] Florschuetz, L. W., Truman, C. R., and Metzger, E. D., "Streamwise Flow and Heat Transfer Distributions for Jet Array Impingement with Cross flow," *Journal of Heat Transfer*, vol. 103, pp. 337-342, 1983.
- [16] Gillespie, D. R. H., Wang, Z., Ireland, P. T., and Kohler, S. T., "Full Surface Local Heat Transfer Coefficient Measurements in a Model of an Integrally Cast Impingement Cooling Geometry," *Journal of Turbomachinery*, vol. 120, no. 1, pp. 92-99, 1998.
- [17] Chambers, A. C., Gillespie, D. R. H., Ireland, P. T., and Dailey, G. M., "The Effect of Initial Cross Flow on the Cooling Performance of a Narrow Impingement Channel," *Journal of Heat Transfer*, vol. 127, no. 4, pp. 358-365, 2005.

- [18] Chambers, A. C., Gillespie, D. R. H., Ireland, P. T., and Kingston, R., "Enhancement of Impingement Cooling in a High Cross Flow Channel Using Shaped Impingement Cooling Holes," *Journal of Turbomachinery*, vol. 132, no. 2, pp. 001-021, 2010.
- [19] Chyu, M. K. and Alvin, M. A., "Turbine Airfoil Aerothermal Characteristics in Future Coal-Gas-Based Power Generation Systems," *Heat Transfer Research*, vol. 41, no. 7, pp. 737-752, 2010.
- [20] Ricklick, M., Kapat, J. S., "Sidewall effects on heat transfer coefficient in a narrow impingement channel," *Journal of Thermophysics and Heat Transfer*, vol. 24, no. 1, pp. 123-132, 2010.
- [21] Claretti, R., Hossain, J., Harrington, J. T., Bernstein, J. A., Verma, S. B., Kapat, J. S., "Heat Transfer Study on Multiple Walls of an Impingement Channel With Variable Jet Heights," in *ASME 2013 Heat Transfer Summer Conference*, Minneapolis, 2013.
- [22] Miller, N., Siw, S. C., Chyu, M. K., and Alvin, M. A., "Effects of Jet Diameter and Surface Roughness on Internal Cooling with Single Array of Jets," in *Proceedings of ASME Turbo Expo: Turbine Technical Conference and Exposition*, 2013, San Antonio, Texas, USA, GT2013-95400.
- [23] Uysal, U., Li, P. W., Chyu, M. K., and Cunha, F. J., "Heat Transfer on Internal Surfaces of a Duct Subjected to Impingement of a Jet Array with Varying Jet Hole-Size and Spacing.," *Journal of Turbomachinery*, vol. 128, no. 1, pp. 158-165, 2006.

- [24] Fechter, S., Terzis, Ott, P., Weigand, B., and von Wolfersdorf, J., "Experimental and numerical investigation of narrow impingement cooling channels," *Int. Journal of Heat and Mass Transfer*, vol. 67, pp. 1208-1219, 2013.
- [25] Hossain, J., Tran, L. V., Kapat, J. S., Fernandez, E., and Kumar, R., "An Experimental Study of Detailed Flow and Heat Transfer Analysis in a Single," in *ASME Turbo Expo*, Dusseldorf, 2013.
- [26] Terzis, A., Skourides, C., Ott, Peter., Wolfersdorf, Jens von., Weigand, B., "Aerothermal Investigation of a Single Row Divergent Narrow Impingement Channel by Particle Image Velocimetry and Liquid Crystal Thermography," *Journal of Turbomachinery*, vol. 138, no. 5, pp. 051003-051012, 2015.
- [27] Weigand, B., and Spring, S., "Multiple Jet Impingement - A Review," *Heat Transfer Research*, vol. 42, no. 2, pp. 101-142, 2011.
- [28] Kercher, D. M., and Tabakoff, W., "Heat Transfer Study by a Square Array of Round Air Jets Impinging Perpendicular to a flat Surface Including the Effect of Spent Air," *Journal of Engineering for Gas Turbines and Power*, vol. 92, no. 1, pp. 73-82, 1970.
- [29] Hollwarth, B. R., and Berry, R. D., "Heat Transfer From Arrays of Impinging Jets with Large Jet-to-Jet Spacing," *Journal of Heat Transfer*, vol. 100, no. 2, pp. 352-357, 1978.
- [30] Metzger, D. E., Florschuetz, L. W., Takeuchi, D. I., Behee, R. D., and Berry, R. A., "Heat Transfer Characteristics for Inline and Staggered Arrays of Circular Jets with Crossflow of Spent Air," *Journal of Heat Transfer*, vol. 101, no. 3, pp. 526-531, 1979.

- [31] Andrews, G. E., Hussain, R. A. A., and Mkpadi, M. C., "Enhanced Impingement Heat Transfer: The Influence of Impingement X/D for Interrupted Rib Obstacles (Rectangular Pin Fins)," *Journal of Turbomachinery*, vol. 128, no. 2, pp. 321-331, 2006.
- [32] Trabold, T. A., and Obot, N. T., "Impingement Heat Transfer Within Arrays of Circular Jets. Part II: Effects of Crossflow in the Presence of Roughness Elements," *Journal of Turbomachinery*, vol. 109, no. 4, pp. 594-601, 1987.
- [33] Van Treuren, K. W., Wang, Z., , "Local Heat Transfer Coefficient and Adiabatic Wall Temperature Measurement Beneath Arrays of Staggered and Inline Impinging Jets," in *International Gas Turbine and Aeroengine Congress and Exposition*, The Hague, Netherlands, 1994.
- [34] Huang, L., El-Genk, M. S., "Heat Transfer of an Impinging Jet on a Flat Surface," *Int. J. Heat Mass Transfer*, vol. 37, no. 1994, pp. 1915-1923, 1994.
- [35] Son C. M., Gillespie D. R. H., Ireland P. T. and Dailey G. M., "Heat Transfer and Flow Characteristics of an Engine Representative Impingement Cooling System," *Journal of Turbomachinery*, vol. 123, pp. 154-160, 2001.
- [36] Azad G. S., Huang Y. and Han J.-C., "Jet Impingement Heat Transfer on Pinned Surfaces Using a Transient Liquid Crystal Technique," *International Journal of Rotating Machinery*, vol. 8, no. 3, pp. 161-173, 2002.
- [37] Dano, B.P.E., Liburdy, J.A. & Kanokjaruvijit, K., " Flow characteristics and heat transfer performance of a semi confined impinging array of jets: effect of nozzle geometry," *International Journal of Heat and Mass Transfer*, vol. 48, pp. 691-701, 2005.

- [38] Yan W. M., Liu H. C., Soong C. Y. and Yang W. J., "Experimental Study of Impinging Heat Transfer Along Rib-Roughened Walls by Using Transient Liquid Crystal Technique," *International Journal of Heat and Fluid Flow*, vol. 48, pp. 2420-2428, 2005.
- [39] Leon, F. G. Geers, L. F. G., Hanjalic, K., and Tummers, M. J., "Wall imprint of turbulent structures and heat transfers in multiple impinging jet arrays," *Journal of Fluid Mechanics*, vol. 546, pp. 255-284, 2006.
- [40] Park, J., Goodro, M., Ligrani, P., Fox, F., and Moon, Hee-Koo., "Separate Effects of Mach Number and Reynolds Number on Jet Array Impingement Heat Transfer," *Journal of Turbomachinery*, vol. 129, 2007.
- [41] Goodro, M., Park, M., Ligrani, P., Fox, M., Moon, H. K., "Effect of Hole Spacing on Jet Array Impingement Heat Transfer," in *ASME Turbo Expo 2007: Power for Land, Sea, and Air*, Montreal, Canada, 2007.
- [42] Esposito E. I., Ekkad S. V., Kim Y. and Dutta P., "Novel Jet Impingement Cooling Geometry for Combustor Liner Backside Cooling," *Journal of Thermal Science and Engineering Applications*, vol. 1, no. 2, pp. 021001-021008, 2009.
- [43] Katti, V. & Prabhu, S. V., "Influence of streamwise pitch on the local heat transfer characteristics for in-line arrays of circular jets with crossflow of spent air in one direction," *Heat and Mass Transfer*, vol. 45, no. 9, pp. 1167-1184, 2009.
- [44] Spring, S., Xing, Y., and Weigand, B., "An Experimental and Numerical Study of Heat Transfer from Arrays of Impinging Jets with Surface Ribs," *Journal of Heat Transfer*, vol. 134, no. 8, pp. 082201-11, 2012.

- [45] Xing, Y., Spring, S., and Weigand, B., "Experimental and Numerical Investigation of Heat Transfer Characteristics of Inline and Staggered Arrays of Impinging Jets," *Journal of Heat Transfer*, vol. 134, no. 8, pp. 092201-11, 2010.
- [46] Chi, Z., and Ren, J., "Experimental and Numerical Study of the Anticrossflows," *International Journal of Heat and Mass Transfer*, vol. 64, pp. 567-580, 2013.
- [47] Hossain, J., Garrett, C., Curbelo, A., Harrington, J., Wang, W., Kapat, J., Thorpe, S., Maurer, M., "Use of Rib Turbulators to Enhance Post-Impingement Heat Transfer for Curved Surface," in *ASME Turbo Expo 2016: Turbomachinery Technical Conference and Exposition*, Seoul, South Korea, 2016.
- [48] Hrycak, P., "Heat Transfer from a Row of Impinging Jets to Concave Cylindrical Surfaces," *International Journal of Heat and Mass Transfer*, vol. 24, pp. 407-419, 1981.
- [49] Metzger, D. E., and Bunker, R. S., "Local Heat Transfer in Internally Cooled Turbine Airfoil Leading Edge Regions: Part I: Impingement Without Film Coolant Extraction Local Heat Transfer in Internally Cooled Turbine Airfoil Leading Edge Regions: Part I: Impingement W," *Journal of Turbomachinery*, vol. 112, no. 3, pp. 451-458, 1990.
- [50] Taslim, M. E., and Bethka, D., "Experimental and Numerical Impingement Heat Transfer in an Airfoil Leading-Edge Cooling Channel with Cross-flow," *Journal of Turbomachinery*, vol. 131, no. 1, pp. 011-021, 2009.
- [51] Gau, C., Lee, C. C., "Impingement Cooling Flow Structures and Heat Transfer along Rib-Roughened Walls," *International Journal Heat Mass Transfer*, vol. 35, no. 11, pp. 3009-3020, 1992.

- [52] Hansen, G. L., and Webb, W. B., "Air Jet Impingement Heat Transfer from Modified Surfaces," *Int. J. Heat Mass Transfer*, vol. 36, no. 4, pp. 989-997, 1993.
- [53] Haiping, C., Dalin, Z., and Taiping, D., "Impingement Heat Transfer from Rib Roughened Surface within Arrays of Circular Jet: The Effect of the Relative Position of the Jet Hole to the Ribs, Proceedings of the International," in *Proceedings of the International Gas Turbine & Aeroengine Congress & Exhibition, Orlando, Florida, 97-GT-331*, Orlando, 1997.
- [54] Haiping, C., Jingyu, Z., and Taiping, H., "Experimental Investigation on Impingement Heat Transfer from Rib Roughened Surface within Arrays of Circular Jet: Effect of Geometric Parameters," in *Proceedings of the International Gas Turbine & Aeroengine Congress & Exhibition, Stockholm, Sweden, 98-GT-208*, Stockholm, 1998.
- [55] Annerfeldt, M. O., Persson, J. L., Torisson, T., "Experimental Investigation of Impingement Cooling with Turbulators or Surface Enlarging Elements," in *Proceedings of ASME Turbo Expo. New Orleans, Louisiana, 2001-GT-0149*, Louisiana, 2001.
- [56] Son, C., Dailey, G., Ireland, P., and Gillespie, D., "An Investigation of the Application of Roughness Elements to Enhance Heat Transfer in an Impingement Cooling System," in *Proceedings of GT2005, ASME Turbo Expo 2005: Power for Land, Sea and Air, Reno-Tahoe, Nevada, USA, GT2005-68504*, Reno-Tahoe, 2005.
- [57] El-Gabry, L. A., and Kaminski, D. A., "Experimental Investigation of Local Heat Transfer Distribution on Smooth and Roughened Surfaces Under an Array of Angled Impinging Jets," *Journal of turbomachinery*, vol. 127, no. 3, pp. 532-544, 2005.

- [58] Brakmann, R., Chen, L., Weigand, B., and Crawford, M., "Experimental and Numerical Heat Transfer Investigation of an Impinging Jet Array on A Target Plate Roughened by Cubic Micro Pin Fins," in *Proceedings of ASME Turbo Expo 2015: Turbine Technical Conference and Exposition*, GT2015-42149, Montréal, 2015.
- [59] Gau, C., Lee, C. C., "Impingement Cooling Flow Structures and Heat Transfer along Rib-Roughened Walls," *International Journal Heat Mass Transfer*, vol. 35, no. 11, pp. 3009-3020, 1992.
- [60] Harrington, J., Nayebzadeh, A., Winn J., Wang, W., Kapat, J., Maurer, M., and Thorpe, S., "Effect of Target Wall Curvature on Heat Transfer and Pressure Loss from Jet Array Impingement," in *Proceedings of ASME Turbo Expo 2015: Turbine Technical Conference and Exposition GT2016*, Montreal, 2015.
- [61] Chandra, R. P., Niland, M. E., and Han, J. C., "Turbulent Flow Heat Transfer and Friction in a Rectangular Channel With Varying Number of Ribbed Walls," in *International Gas Turbine and Aeroengine Congress & Exposition*, Houston, 1995.
- [62] Momin, A-M. E., Saini, J. S., and Solanki, S. C., "Heat transfer and friction in solar air heater duct with V-shaped rib roughness on absorber plate," *International Journal of Heat and Mass Transfer*, vol. 45, no. 16, pp. 3383-3396, 2002.
- [63] Maurer, M., "Experimental and Numerical Investigations of Convective Cooling Configurations for Gas Turbine Combustors," University of Stuttgart, Stuttgart, 2008.
- [64] R. Jefferson and P. Tucker, "Wall-Resolved LES and ZONAL LES of round impingement heat transfer," *Numerical Heat Transfer Part B*, pp. 190-208, 2011.

- [65] A. Dewan, R. Dutta and S. Balaji, "Recent Trends in Computation of Turbulent Jet Impingement Heat Transfer," *Heat Transfer Engineering*, pp. 447-460, 2012.
- [66] M. Olsson; L. Fuchs, "Large Eddy Simulations of a Forced Semiconfined Circular Impinging Jet," *Physics of Fluids*, vol. 10, pp. 476-486, 1998.
- [67] Liu, Q., "Study of Heat Transfer Characteristics of Impinging Air Jet Using Pressure and Temperature Sensitive Luminescent Paint," Ph.D dissertation, University of Central Florida, Orlando, 2006.
- [68] Sullivan, J. P., Liu, T, Pressure and Temperature Sensitive Paints, Germany: Springer, 2005.
- [69] Wilcox, D.C., and Rubesin, M. W., "Progress in Turbulence Modeling for Complex Flow Fields Including effects of Compressibility," 1980.
- [70] Wilcox, D.C, Turbulence Modeling for CFD, La Canada: DCW Industries, 2006.
- [71] Piomelli, U., and Chasnov,J.,, "Large Eddy Simulations: Theory and Applications," *Turbulence and Transition Modeling*, pp. 269-336, 1996.
- [72] Germano, M., M., Piomelli, U., Moin, P., and Cabot, W. H. A, "Dynamic Subgrid-Scale Eddy Viscosity Model," *Physics of Fluids*, vol. 3, no. 7, pp. 1760-1765, 1991.
- [73] Chen, Ching-Jen., Fundamental of Turbulence Modeling, Washington: Taylor & Francis, 1997.
- [74] Tardu, S., Statistical Approach to Wall Turbulence, Hoboken, NJ: Wiley, 1988.
- [75] George, W. K., Advances In Turbulence.

- [76] Markatos, N. C. , "The Mathematical Modelling of Turbulent Flows," *Applied Mathematical Modelling*, vol. 10, no. 3, pp. 190-220, 1986.
- [77] Al-Sharif, S. F., "Reynolds Stress Modelling".
- [78] Celik, I. B., "Introductory Turbulence Modeling," 1999.
- [79] McDonough, J. M., "Introductory Lectures on Turbulence," 2007.
- [80] Parneix, S., and Durbin, P., "Numerical Simulation of 3D Turbulent Boundary Layers Using the V2F model," *Annual Research Briefs*, pp. 135-148, 1997.
- [81] Nicoud, F., and Ducros, F, "Subgrid-scale stress modelling based on the square of the velocity gradient tensor," *Flow, Turbulence and Combustion*, vol. 62, pp. 183-200, 1999.
- [82] The American Society of Mechanical Engineers, ASME PTC 19.5 Flow Measurement Performance Test Codes, New York,NY: The American Society of Mechanical Engineers, 2004.
- [83] Navarra, K. R., "Development of the Pressure Sensitive Paint Technique For Advanced Turbomachinery Applications," Virginia Polytechnic Institute and State University, Blacksburg, 1997.
- [84] Liu, Q., "Study of Heat Transfer Characteristics of Impinging Air Jet using Pressure and Temperature Sensitive Luminescent Paint," University of Central Florida Dissertation, Orlando, 2006.
- [85] Claretti, R., Hossain, J., Verma, S. B., Kapat, J. Downs, J. P., Goebel, G. E., "Heat Transfer Characteristics of Jet Array Impingement at Low Streamwise Spacing," San Antonio, Texas, USA, 2013.

- [86] Hossain, J., Fernandez, E., Voet, T., Kapat, J. S., "A Detailed Experimental and Numerical Investigation of Flow Physics in a Single Row Narrow Impingement Channel Using PIV,LES and RANS," in *52nd AIAA/SAE/ASME Joint Propulsion Conference*, Salt Lake City, UT, 2016.
- [87] Zuckerman, M., Lior, N., "Impingement Heat Transfer: Correlations and Numerical Modeling," *Journal of Heat Transfer*, vol. 124, p. 544, 2005.
- [88] Hossain, J, Tran, L. V., Kapat, J. S., Fernandez, E., Kumar, R., An Experimental Study of Detailed Flow and Heat Transfer Analysis in a Single Row Narrow Impingement Channel, Dusseldorf: ASME Turbo Expo 2014: Turbine Technical Conference and Exposition, 2014.
- [89] R. H. J. V. S. B. K. J. S. D. J. P. a. G. G. E. Claretti, "Heat Transfer Characteristics of Jet Array Impingement at Low Streamwise Spacing," in *ASME Turbo Expo 2013: Turbine Technical Conference and Exposition*, San Antonio, 2013.
- [90] Jambunathan, E., Moss E L., and Button, L., "A review of heat transfer data for Single circular jet jet impingement".
- [91] Royne, A., Dey, C., "International Journal of Heat and Mass Transfer," *Effect of nozzle geometry on pressure drop and heat transfer in submerged jet arrays*, vol. 49, pp. 800-804, 2006.
- [92] Baughn, J. W., Hechanova, A. E., and Yan, Xiaojun., "An Experimental Study of Entrainment Effects on the Heat Transfer From a Flat Surface to a Heated Circular Impinging Jet," *Journal of Heat Transfer*, vol. 32, pp. 11685-1174, 1991.
- [93] <http://www.ercofac.org/>.

- [94] Uddin, N., "Turbulence Modeling of Complex Flows in CFD," University of Stuttgart, 2008.
- [95] O'Donovan, T. Murray and B. Darina, "Jet impingement heat transfer-Part 1: Mean and root-mean-square heat transfer and velocity distributions," *International Journal of Heat and Mass Transfer*, vol. 50, pp. 3291-3301, 2007.
- [96] Webb, B., "Single-phase liquid jet impingement heat transfer," *Advances in heat transfer*, pp. 105-217, 1995.
- [97] Behnia, M., Parneix, S., and Durbin, P., "Accurate modelling of impinging jet heat transfer," *Annual Research Briefs*, 1997.
- [98] Viskanta, R., "Heat transfer to impinging isothermal gas and flame jets," *Exp. Thermal Fluid Sci*, vol. 6, pp. 111-134, 1993.
- [99] M. Angioletti, R. D. Tommaso and G. R. E. Nino, "Simultaneous visualization of flow field and evaluation of local heat transfer by transitional impinging jets," *International Journal of Heat and Mass Transfer*, vol. 46, pp. 1703-1713, 2003.
- [100] Popiel, C. O., Trass, O., "Visualization of a Free and Impinging Round Jet," *Experimental thermal and fluid science*, pp. 253-264, 1991.
- [101] Liu, T., Sullivan, J.P., "Heat Transfer and Flow Structures in an excited circular impinging jet," *Int. J Heat Mass Transfer*, vol. 39, no. 17, pp. 3695-3706, 1996.
- [102] Tsubokura, M., Kobayashi, T., Taniguchi, N., Jones, W. P. , "A Numerical Study on the Eddy Structures of Impinging Jets Excited at the Inlet," *International Journal of Heat and Fluid Flow*, vol. 24, pp. 500-511, 2003.

- [103] O'Donovan, T. S., Murray, Darina. B., "Jet impingement heat transfer – Part II: A temporal investigation," *International Journal of Heat and Mass Transfer*, vol. 50, pp. 3302-3314, 2007.
- [104] Schadow, K. C., Gutmark, E., "Combustion Instability Related to Vortex Shedding in Dump Combustors and Their Passive Control," *Prog. Energ. Combust. Sci*, vol. 18, pp. 117-132, 1992.
- [105] Han, B., Goldstein, R. J., "Instantaneous Energy Separation in a Free Jet Part I. Flow Measurement and Visualization," *Int. J. Heat Mass Transfer*, vol. 46, pp. 117-132, 2003.
- [106] Nishino. K., Samada, M., Kasuya, K., Torii, K., "Turbulence Statistics in the Stagnation Region of an Axisymmetric Impinging Jet Flow," *Int. J. Heat and Fluid Flow*, vol. 17, pp. 193-201, 1996.
- [107] Chiriac, V. A., and Ortega, A., "A numerical study of the unsteady flow and heat transfer in a transitional confined slot jet impinging on an isothermal surface," *International Journal of Heat and Mass Transfer*, vol. 45, no. 6, pp. 1237-1248, 2002.
- [108] Hallqvist, T., "Large Eddy Simulation of Impinging Jets with Heat Transfer," Royal Institute of Technology, Stockholm, 2006.
- [109] Florschuetz, L.W., Berry, R. A., and Metzger, D. E., "Periodic Streamwise Variations of Heat Transfer Coefficients for Inline and Staggered Arrays of Circular Jets with Cross Flow of Spent Air," *Journal of Heat Transfer*, vol. 102, pp. 132-137, 1980.
- [110] Xu, G., Antonia, R., "Effect of Different Initial Conditions on a Turbulent Round Free Jet," *Experiments in Fluids*, vol. 33, no. 5, pp. 677-683, 2002.

- [111] Cooper, D., Jackson, D. C., Launder, B. E., Liao, G. X., "Impinging jet studies for turbulence model assessment- I. Flow field experiments," *Int. J. Heat and Mass Transfer*, vol. 36, no. 10, pp. 2675-2684, 1993.
- [112] Hadziabdic, M., and Hanjalic, K., "Vortical structures and heat transfer in a round impinging jet," *Journal of Fluid Mechanics*, pp. 221-260, 2008.
- [113] Frohlich, J., and Rodi, W., *Introduction to Large Eddy Simulation of Turbulent Flows*, New York: Cambridge University Press.
- [114] Pope, S. B., *Turbulent Flows*, New York, 2000.
- [115] Florschuetz, L. W., Truman, C. R., and Metzger, E. D., "Streamwise Flow and Heat Transfer Distributions for Jet Array Impingement with Cross flow," *Journal of Heat Transfer*, vol. 103, pp. 337-342, 1981.
- [116] Florschuetz, L. W., and Isoda, Y., "Flow Distributions and Discharge Coefficient for Jet Array Impingement with Initial Cross Flow," *Journal of Engineering for Power*, vol. 105, no. 2, pp. 296-304, 1983.